SnO_2 Thin Films - Chemical Vapor Deposition and Characterization

Dissertation

Yinmei Lu

JUSTUS-LIEBIG-
UNIVERSITÄT
GIESSEN

SnO_2 Thin Films - Chemical Vapor Deposition and Characterization

vorgelegte Dissertation

von

Dipl.-Phys. Yinmei Lu

im Fachbereich 07 (Physik) der Justus-Liebig-Universität Giessen

zur Erlangung des akademischen Grades Dr. rer. nat.

Gutachter: Prof. Dr. Peter Jens Klar

Prof. Dr. Martin Eickhoff

I. Physikalisches Institut

Justus-Liebig-Universität Giessen

Gießen, November 2015

Contents

1 Introduction

Over the last two decades transparent conducting oxides (TCOs) such as SnO_2, ZnO, In_2O_3, Ga_2O_3, CdO and their ternary and more complex alloys have been of increasing interest. The most compelling motivation to study TCOs is the increasing number of applications including the large flat screen high-definition televisions (HDTVs including liquid crystal display (LCD), plasma and organic light-emitting diode (OLED) based displays), large and high-resolution flat screens for portable computers, the energy-efficient low-emittance windows, solar control and electrochromic windows, thin film photovoltaics (PV), oxide based transistors and transparent electronics as well as hand-held, flexible and smart devices [1]. It is predicted that the transparent display market will sharply grow to reach a $87.2 billion volume by the year 2025 as can been seen in Fig. 1.1 [2].

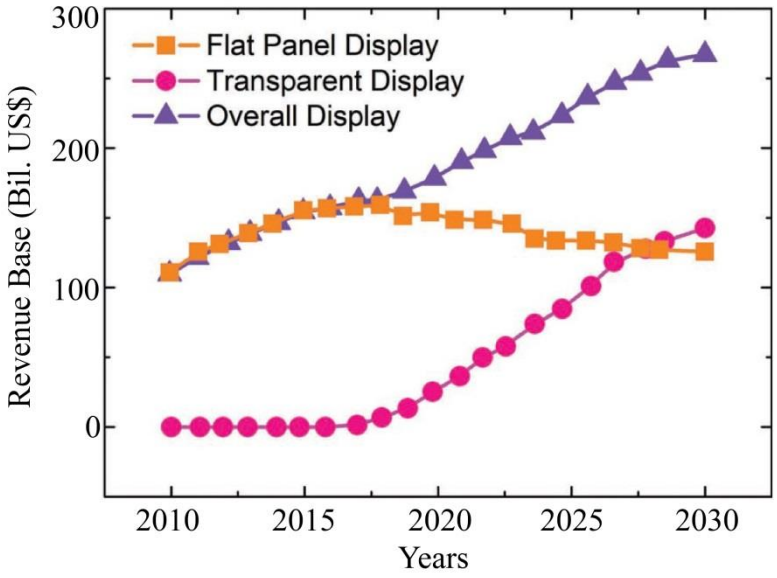

Fig. 1.1. Transparent display technology evolution and global display market (from Ref. [2]).

SnO_2 belongs to the important family of oxide materials that combine low electrical resistance with high optical transparency in the visible range of the electromagnetic spectrum. Another property of SnO_2 is that, although it is transparent in the visible, it is highly reflective for infrared light. Thus, tin oxide or fluorine-doped tin oxide (SnO_2:F) is widely used as a coating in energy efficient windows. Karlsson *et al.* reported that windows with tin oxide coatings are efficient in preventing radiative heat loss, due to their low thermal emittance of approximately 0.15, compared to about 0.84 for uncoated glass [3].

In addition to above mentioned applications as a TCO material, SnO_2 may also be applied to serve as the front electrode of solar cells, electrochromic mirrors and windows, as a layer to defrost windows of aircrafts and automobiles, as a coating of oven windows, as a static dissipation layer, as a layer of touch-panel controls, as electromagnetic shielding etc. [4].

Apart from being applied as a TCO material, SnO_2 is also used as oxidation catalyst, and as the active material in solid state gas sensors. For these two applications the surface of SnO_2 is of direct relevance. More details about these applications of SnO_2 can be found in Ref. [5] and [6].

Of all TCO materials, SnO_2 related materials are cheapest (SnO_2:F), and possess the highest transparency (Cd_2SnO_4), the lowest plasma frequency (SnO_2:F), the highest work function and best contact to *p*-Si (SnO_2:F), the best thermal stability (SnO_2:F), the best mechanical durability (SnO_2:F), the best chemical durability (SnO_2:F), and are least toxic (SnO_2:F) [4].

Ever since the first report of transparent conducting CdO films prepared by thermal oxidation of sputtered cadmium by Bädeker in 1907 [7], the interest in transparent conductors has increased tremendously. Numerous techniques for depositing several very useful transparent conducting oxides, notably antimony-doped tin oxide or fluorine-doped tin oxide and tin-doped indium oxide have been developed, some are used at large-scale production levels [8]. During the 1960s to 1980s, much effort was dedicated to single crystal growth by vapor-phase techniques [9-13]. The first group to successfully grow SnO_2 crystals were Marley *et al.* at the Corning Glass Works Laboratory in 1961 [14]. The fabricated bulk crystals were mostly needles or rods with a relatively small size only up to $7\times7\times20$ mm^3 [15]. Its material properties including electrical properties, fundamental energy gap and optical absorption were closely studied at that time [9, 10, 16-18]. Despite the progress in single crystal growth the crystal size achievable for SnO_2 is still limited. Until now, a single crystal SnO_2 substrate is still not available.

However, interest in SnO_2 has not been affected by the lack of large size single crystals. Up to now, a number of methods have been developed to produce thin SnO_2 films, including atomic layer deposition (ALD) [19-21], spray pyrolysis [22, 23], pulsed laser deposition (PLD) [24], molecular beam epitaxy (MBE) [25], sputtering [26, 27], metal organic chemical vapor deposition (MOCVD) [28, 29], chemical vapor deposition (CVD) [30], etc. On the large-scale production level, notably F-doped SnO_2 and Sb-doped SnO_2 can be produced on various substrates depending on the intended application. Glass and plastic substrates are commonly used in low temperature processes. CVD is a favorable technique and suitable for commercial exploitation since it can yield a high growth rate, and it is inexpensive and versatile and capable of producing films of high quality.

Furthermore, if the process is well controlled, films with a homogenous thickness and stoichiometry can be deposited on complex substrates.

Since many of the emerging applications of SnO_2 in functional wide-bandgap semiconductor devices require highly crystalline epitaxial films, an understanding of the effects of growth parameters and substrate selection on the quality of the epitaxial SnO_2 is important. Recently, huge efforts have been made to grow epitaxial SnO_2 thin films on different substrates, such as on *c*-, a-, *m*-, and *r*-plane sapphire, TiO_2 (110) and (001), Y-stabilized ZrO_2 (100) and (120), $SrTiO_3$ (111), 6H-SiC (0001), MgO (100), and InP (100) etc. [20, 21, 24, 31-41]. However, it turns out to be rather difficult to obtain high-quality heteroepitaxial films with smooth surfaces, because of the large lattice mismatch between SnO_2 and the substrate materials available.

The main purposes of this study were to fabricate SnO_2 films on different substrates by CVD, to investigate the influence of the experimental parameters on the growth rate, composition, and the quality of the films, to find the growth mechanism of the film, and to obtain high-quality SnO_2 films. If such high-quality SnO_2 films were available, we could examine the structure, morphology, optical, electrical properties of this material, and understand the many interesting anisotropic properties of SnO_2.

Despite a fairly large lattice mismatch between SnO_2 and sapphire, sapphire has several advantages as a substrate material: it is stable at high temperatures, optically transparent, and it is cheap compared to other crystalline substrates. This dissertation focuses on SnO_2 thin films on *c*- and *r*-plane sapphires and quartz glass substrates. We have succeeded in obtaining transparent high-quality single crystalline SnO_2 films with thickness up to a few micrometers by CVD on *c*- and *r*-plane sapphire substrates.

There have been several reports in the literature discussing the growth mechanism of SnO_2 (101) on *r*-sapphire [31, 42], but none so far for SnO_2-epitaxy on *c*-plane sapphire. In this work we report on the epitaxial growth of SnO_2 films on *c*-sapphire using chemical vapor deposition (CVD), and investigate the growth mechanism of SnO_2 (100) film on Al_2O_3 (0001) by a detailed X-ray diffraction (XRD) analysis complemented with scanning electron microscopy.

This thesis is organized as follows.

Chapter 2 starts with an introduction of the established crystalline structure of SnO_2, followed by a brief summary of the known physical properties such as electrical, optical properties of SnO_2 material. The working principle of the CVD technique and the specific setup used in this work as well as the experimental parameters of the deposition will shortly be described in ***Chapter 3***.

Chapter 4 outlines the characterization techniques employed in this work. Those are X-ray diffraction (XRD), atomic force microscopy (AFM), and scanning electron microscopy (SEM), X-ray photoemission spectroscopy (XPS), Raman spectroscopy for structure,

surface and cross-section morphologies, and stoichiometry characterization, and photoluminescence (PL), optical transmission and Hall effect measurements for determining optical and electrical properties.

In ***Chapter 5***, we briefly discuss the SnO_2 films grown on quartz glass and describe the influence of the substrate temperature on the film growth rate. The structure, morphology and optical properties of the polycrystalline SnO_2 films are introduced.

In ***Chapter 6***, we describe the systematic investigation of the properties of the films grown on *c*-sapphire at a substrate temperature lower than 900 °C. The extensive experiments and detailed characterization of series of SnO_2 films of different thickness reveal the growth mechanism of the SnO_2 film on *c*-sapphire.

Chapter 7 presents a discussion of the mirror symmetry growth of SnO_2 grown at a substrate temperature lower than 900 °C on *r*-sapphire, and the tilt of the film on the substrate is determined.

The successful growth of thick, high-quality epitaxial SnO_2 films on *c*- and *r*-plane substrates and thick polycrystalline film on quartz glass at high substrate temperature of 900 °C is described in ***Chapter 8***. The structural characteristics of the high-quality layers have been investigated in detail. Angle dependent Raman measurements were performed and confirm the results of the XRD characterization. Low temperature PL shows a recombination line of SnO_2 at 3.30eV. This emission line could be interpreted as an excitonic transition. The optical characterization of the high-quality SnO_2 films is presented in the last subsection. Finally, a brief summary and an outlook for future work are given in ***Chapter 9***.

References

[1] H. Hosono, D.C. Paine, *Handbook of Transparent Conductors*, Springer, New York Heidelberg Dordrecht London, 2010.
[2] E. Fortunato, P. Barquinha, R. Martins, *Oxide Semiconductor Thin-Film Transistors: A Review of Recent Advances*, Advanced Materials, 24 (2012) 2945-2986.
[3] J. Karlsson, A. Roos, *Annual energy window performance vs. glazing thermal emittance — the relevance of very low emittance values*, Thin Solid Films, 392 (2001) 345-348.
[4] R.G. Gordon, *Criteria for Choosing Transparent Conductors*, MRS Bulletin, 25 (2000) 52-57.
[5] M. Batzill, U. Diebold, *The surface and materials science of tin oxide*, Progress in Surface Science, 79 (2005) 47-154.
[6] S. Das, V. Jayaraman, *SnO_2: A comprehensive review on structures and gas sensors*, Progress in Materials Science, 66 (2014) 112-255.

[7] K. Bädeker, *Über die elekrische Leitfähigkeit und die thermoelektrische Kraft einiger Schwermetallverbindungen*, Ann. Phys. (Leipzig), 22 (1907) 749-766.
[8] K.L. Chopra, S. Major, D.K. Pandya, *Transparent conductors—A status review*, Thin Solid Films, 102 (1983) 1-46.
[9] R. Summitt, J.A. Marley, N.F. Borrelli, *The ultraviolet absorption edge of stannic oxide (SnO_2)*, Journal of Physics and Chemistry of Solids, 25 (1964) 1465-1469.
[10] J. Marley, R. Dockerty, *Electrical Properties of Stannic Oxide Single Crystals*, Phys. Rev., 140 (1965) A304-A310.
[11] S. Robert, *Infrared Absorption in Single-Crystal Stannic Oxide: Optical Lattice-Vibration Modes*, J. Appl. Phys., 39 (1968) 3762-3767.
[12] V. Caslavska, R. Roy, *Epitaxial Growth of SnO_2 on Rutile Single Crystals*, J. Appl. Phys., 40 (1969) 3414-3414.
[13] C.G. Fonstad, A. Linz, R.H. Rediker, *Vapor Phase Growth of Stannic Oxide Single Crystals*, J. Electrochem. Soc., 116 (1969) 1269-1271.
[14] J.A. Marley, T.C. MacAvoy, *Growth of Stannic Oxide Crystals from the Vapor Phase*, J. Appl. Phys., 32 (1961) 2504-2505.
[15] B. Thiel, R. Helbig, *Growth of SnO_2 single crystals by a vapour phase reaction method*, J. Cryst. Growth, 32 (1976) 259-264.
[16] T. Arai, *The Study of the Optical Properties of Conducting Tin Oxide Films and their Interpretation in Terms of a Tentative Band Scheme*, J. Phys. Soc. Jpn., 15 (1960) 916-927.
[17] E.E. Kohnke, *Electrical and optical properties of natural stannic oxide crystals*, Journal of Physics and Chemistry of Solids, 23 (1962) 1557-1562.
[18] W. Spence, *The uv Absorption Edge of Tin Oxide Thin Films*, J. Appl. Phys., 38 (1967) 3767-3770.
[19] J. Sundqvist, J. Lu, M. Ottosson, A. Hårsta, *Growth of SnO_2 thin films by atomic layer deposition and chemical vapour deposition: A comparative study*, Thin Solid Films, 514 (2006) 63-68.
[20] D.H. Kim, J.-H. Kwon, M. Kim, S.-H. Hong, *Structural characteristics of epitaxial SnO_2 films deposited on a- and m-cut sapphire by ALD*, J. Cryst. Growth, 322 (2011) 33-37.
[21] A. Tarre, A. Rosental, A. Aidla, J. Aarik, J. Sundqvist, A. Hårsta, *New routes to SnO_2 heteroepitaxy*, Vacuum, 67 (2002) 571-575.
[22] P. Grosse, F.J. Schmitte, G. Frank, H. Köstlin, *Preparation and growth of SnO_2 thin films and their optical and electrical properties*, Thin Solid Films, 90 (1982) 309-315.
[23] V. Consonni, G. Rey, H. Roussel, D. Bellet, *Thickness effects on the texture development of fluorine-doped SnO_2 thin films: The role of surface and strain energy*, J. Appl. Phys., 111 (2012) 033523.
[24] J.E. Dominguez, L. Fu, X.Q. Pan, *Epitaxial nanocrystalline tin dioxide thin films grown on (0001) sapphire by femtosecond pulsed laser deposition*, Appl. Phys. Lett., 79 (2001) 614-616.
[25] M.Y. Tsai, M.E. White, J.S. Speck, *Investigation of (110) SnO_2 growth mechanisms on TiO_2 substrates by plasma-assisted molecular beam epitaxy*, J. Appl. Phys., 106 (2009) 024911.
[26] M. Becker, A. Polity, P.J. Klar, B.K. Meyer, *Synthesis of tin oxides SnO_{2-x} in the entire composition range (x = 0 to 1) by ion-beam sputter-deposition*, physica status solidi (RRL) – Rapid Research Letters, 9 (2015) 326-330.

[27] Y.-C. Ji, H.-X. Zhang, X.-H. Zhang, Z.-Q. Li, *Structures, optical properties, and electrical transport processes of SnO_2 films with oxygen deficiencies*, physica status solidi (b), 250 (2013) 2145-2152.
[28] X. Feng, J. Ma, F. Yang, F. Ji, C. Luan, *Preparation and characterization of single crystalline SnO_2 films deposited on α-Al_2O_3 (0001) by MOCVD*, Materials Letters, 62 (2008) 1809-1811.
[29] X. Feng, J. Ma, F. Yang, F. Ji, F. Zong, C. Luan, H. Ma, *Structural and photoluminescence properties of single crystalline SnO_2:In films deposited on α-Al_2O_3 (0 0 0 1) by MOCVD*, J. Cryst. Growth, 310 (2008) 3718-3721.
[30] R.N. Ghoshtagore, *Mechanism of CVD Thin Film SnO_2 Formation*, J. Electrochem. Soc., 125 (1978) 110-117.
[31] M.E. White, M.Y. Tsai, F. Wu, J.S. Speck, *Plasma-assisted molecular beam epitaxy and characterization of SnO_2 (101) on r-plane sapphire*, J. Vac. Sci. Technol. A, 26 (2008) 1300-1307.
[32] M.Y. Tsai, M.E. White, J.S. Speck, *Plasma-assisted molecular beam epitaxy of SnO_2 on TiO_2*, J. Cryst. Growth, 310 (2008) 4256-4261.
[33] K. Lingyi, M. Jin, L. Caina, Z. Zhen, *Structural and optical properties of single crystalline columbite tin oxide film*, Appl. Phys. Lett., 98 (2011) 261904.
[34] L. Kong, J. Ma, Z. Zhu, C. Luan, F. Ji, *Structural, electrical and optical properties of SnO_2 films deposited on Y-stabilized ZrO_2 (100) substrates by MOCVD*, J. Cryst. Growth, 312 (2010) 2931-2935.
[35] C. Ke, Z. Yang, W. Zhu, J.S. Pan, S. Karamat, *Heteroepitaxial growth of SnO_2 thin films on $SrTiO_3$ (111) single crystal substrate by laser molecular beam epitaxy*, J. Appl. Phys., 107 (2010) 013515.
[36] D. Liu, Q. Wang, H.L.M. Chang, H. Chen, *Variant structure in metal-organic-chemical-vapor-deposition-derived SnO_2 thin films on sapphire (0001)*, J. Mater. Res., 10 (1995) 1516-1522.
[37] L.C. Tien, D.P. Norton, J.D. Budai, *Epitaxial growth of transparent tin oxide films on (0001) sapphire by pulsed laser deposition*, Mater. Res. Bull., 44 (2009) 6-10.
[38] K. Rachut, C. Körber, J. Brötz, A. Klein, *Growth and surface properties of epitaxial SnO_2*, physica status solidi (a), 211 (2014) 1997-2004.
[39] Z. Zhu, J. Ma, C. Luan, W. Mi, Y. Lv, *Epitaxial growth of SnO_2 films on 6H-SiC (0001) by MOCVD*, Mater. Res. Bull., 47 (2012) 253-256.
[40] C. Luan, J. Ma, X. Yu, Z. Zhu, W. Mi, Y. Lv, *Synthesis and properties of epitaxial SnO_2 films deposited on MgO (100) by MOCVD*, Vacuum, 86 (2012) 1333-1335.
[41] T.W. Kim, D.U. Lee, Y.S. Yoon, *Microstructural, electrical, and optical properties of SnO_2 nanocrystalline thin films grown on InP (100) substrates for applications as gas sensor devices*, J. Appl. Phys., 88 (2000) 3759-3761.
[42] S.K. Vasheghani Farahani, T.D. Veal, A.M. Sanchez, O. Bierwagen, M.E. White, S. Gorfman, P.A. Thomas, J.S. Speck, C.F. McConville, *Influence of charged-dislocation density variations on carrier mobility in heteroepitaxial semiconductors: The case of SnO_2 on sapphire*, Physical Review B, 86 (2012) 245315.

2 SnO_2: a brief review of material and properties

Tin (IV) oxide (with the formula SnO_2) is also known as stannic oxide in the older notation. The mineral form of SnO_2 is called cassiterite, and this is the main ore of tin. SnO_2 is an n-type, wide-band-gap semiconductor.

2.1 Crystal structure

SnO_2 possesses several polymorphs such as the rutile-type ($P4_2/mnm$), $CaCl_2$-type ($Pnnm$, 12 GPa), α-PbO_2-type ($Pbcn$, 17 GPa), pyrite-type ($Pa\bar{3}$, 17 GPa), ZrO_2-type orthorhombic phase I ($Pbca$, 18 GPa), fluorite-type ($Fm\bar{3}m$, 24 GPa), cotunnite-type orthorhombic phase II ($Pnam$, 33 GPa) [1]. SnO_2 is cassiterite with a tetragonal rutile structure under ambient conditions [2]. In this dissertation we focus on rutile SnO_2.

Tin has the electronic configuration [Kr]$4d^{10}5s^25p^2$. Rutile SnO_2 has a tetragonal D_{4h}^{14} symmetry. The unit cell of SnO_2, as shown schematically in Fig. 2.1, is tetragonal (a = 0.4378 nm, c = 0.3187 nm [3]) and contains six atoms, two tin and four oxygen. Sn atoms are situated at (0, 0, 0) and (1/2a, 1/2a, 1/2c) and oxygen atoms at ±(ua, -ua, 0) and (1/2a, 1/2a, 1/2c) ± (ua, ua, 0), with u=0.307. Oxygen atoms are joined to form octahedral network, and the metal atoms regularly occupy the interstitial sites of the oxygen octahedral [4]. Thus, each Sn atom has six nearest oxygen neighbors, which form a distorted octahedron. Sn atoms fill the center positions of the oxygen octahedra. The distance between Sn and O atoms within one octahedron is 2.057 Å. [5]

There are two angles between the equilateral O atoms, α (between anion 1 and 2 as well as 3 and 4) and β (between anion 2 and 3 as well as 4 and 1) as shown in Fig. 2.1. The sum of these two angles is 180°, where α = 78.1° and β = 101.9° (calculated according to Ref.[6]). The lower symmetry of the tetragonal crystal structure of SnO_2 leads to an anisotropy in the electronic and optical properties. For example, the smaller distance between Sn atoms along the c-axis, may result in a higher atomic orbital overlap and thus a more conductive pathway for electron transport [7].

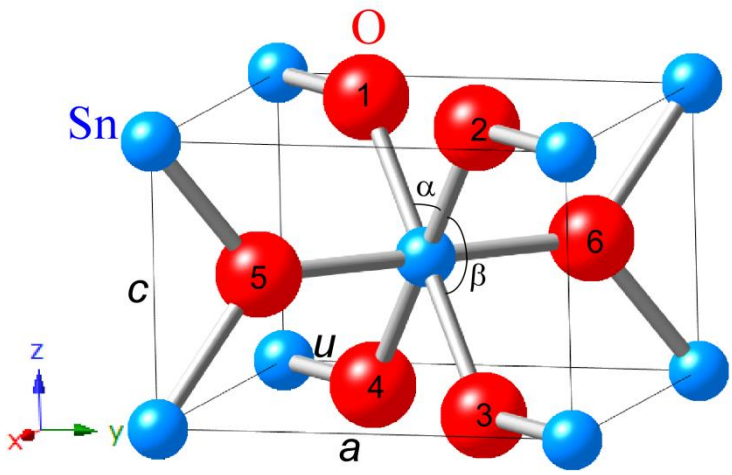

Fig. 2.1. Crystal structure of the tetragonal SnO_2 with the cassiterite structure (drawn with the program CrystalMaker).

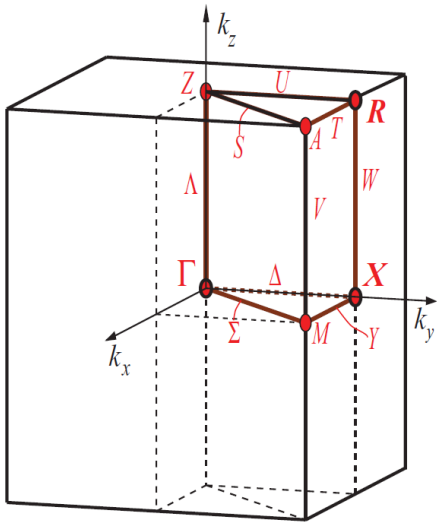

Fig. 2.2. The Brillouin zone of SnO_2 in the rutile structure. The special points R, X, and the zone center Γ are highlighted (from Refs. [8, 9]).

The Brillouin zone of SnO_2 has also simple tetragonal symmetry and is shown in Fig. 2.2 with all symmetry points and axis labelled in the usual way [10].

2.2 Physical properties

2.2.1 Band structure

Despite SnO_2 being a binary oxide of fairly high symmetry and its band structure having been studied theoretically [8, 9, 11-13] and experimentally [14-17] for almost 50 years, its band structure is still not entirely understood. The reasons are that the unit cell contains a fairly large number of atoms, i.e. two tin atoms and four oxygen atoms, and that the effect of the Coulomb interaction on the excited states of the system probed by optical experiments is not negligible. The large number of atoms in the unit cell leads to many bands of different symmetry character at the valence band edge, which are energetically in close vicinity. It took until recently that the Coulomb interaction, which is inherently present in experiment, could be accounted for in ab initio calculations of the band structure of SnO_2. This is important as the excitonic effects are of the same order as the energy differences between the valence bands. However, effects of spin-orbit coupling are still not fully accounted for. Conduction band minimum (CBM) and the valence band maximum (VBM) are located at the Γ point of the Brillouin zone. Robertson *et al.* [12] were one of the first to give a reasonable description of the SnO_2 band structure. The conduction bands arise from *s* and *p* states of Sn with the CB edge at Γ being mainly *s*-like. The upper valence bands are mainly due to tin *d* and oxygen *p* states. The CBM at zone center Γ is formed out of Sn 5*s* states. Robertson *et al.* (see Ref. [7], chapter 2) reported that the upper valence band from 0 eV down to -8.1 eV consists mainly of O 2*p* states, mixed with some Sn *s* and *p* states. At -16 eV, there are mainly O 2*s* states (see Fig. 2.3a).

The upper valence band in SnO_2 is typical for many oxides. It is relatively flat, and thus has a large effective mass. The conduction band of SnO_2 exhibits significant free-electron like character in the Δ direction (Γ-*X* direction), or Λ direction (Γ-*M* direction), where the direct gap was calculated as 3.7 eV by Mishra *et al*. [13] and as 3.6 eV by Barbarat and Calatayud *et al.* [18, 19], respectively. Other theoretical and experimental works reported the values of the SnO_2 band-gap in the range from 3.5 to 4.7 eV [9, 20-23]. The analysis of the partial density of states is shown in Fig. 2.3(b) (from Ref. [13]). It can be seen that at the valence band edge O 2*p* states as well as Sn 4*d* states contribute significantly to the density of states.

The effective mass of the conduction electron is expected to be rather small from the band structure. Mi *et al.* reported that the theoretical values of the effective mass for SnO_2 were $m^*_{\perp} = 0.26\ m_0$ and $m^*_{\parallel} = 0.20\ m_0$, where $\perp$ and $\parallel$ are perpendicular and parallel to the *c* axis, or along the Γ-*X* and Γ-*Z* (see in Fig. 2.2) in the Brillouin zone (m_0 is the free

electron mass) [24]. Based on the cyclotron resonance, Button *et al.* obtained the results of $m^*_{\perp}$ = 0.299 m_0 and $m^*_{\parallel}$ = 0.234 m_0, which were in good agreement with the calculated values [25]. A value of the effective mass of a valence-band of 1.0 m_0 was suggested by Sanon *et al.* [23].

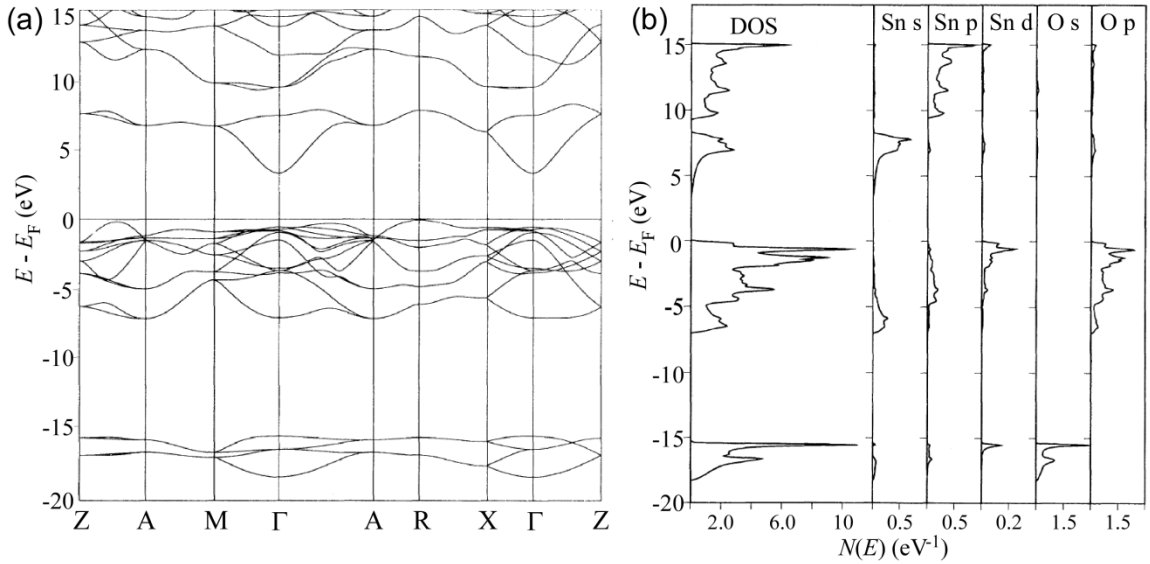

Fig. 2.3. (a) Band structures, and (b) density of states of SnO_2 (from Ref. [13]).

2.2.2 Transport properties

SnO_2 shows n-type conductivity. Oxygen vacancies are commonly considered as the source of the n-type conductivity. However, first-principles investigations of undoped SnO_2 by Kilic and Zunger [26] predicted that although oxygen vacancies are contributing to carrier generation, the majority electron generation takes place due to tin interstitials (Sn_i). The Sn_i defect states appear above the CBM and thus readily create conduction electrons, whereas oxygen vacancies are shallow donors, whose energies are located below CBM.

Transport measurements were carried out on single crystal samples because of their high crystal quality. Fonstad and Rediker reported that single crystals of SnO_2 with low carrier concentrations of ~10^{16}/cm^3 possess a mobility near 260 cm^2/Vs at room temperature [27]. It should be noted, that the electron mobility in thin films is usually much lower than that measured in single crystals. For instance, in epitaxial films (100 nm thick) with electron concentrations of the order of 10^{19} cm^{-3}, an electron mobility of 37 cm^2/Vs was reported [28]. The significant decrease in mobility is at least partially due to scattering by crystal defects, such as antiphase boundaries, domain boundaries, planar

defects, stacking faults and partial dislocations, the density of which varies with film thickness. For polycrystalline films deposited onto glass or polymer substrates, apart from the above mentioned scattering processes, electron scattering by charged grain boundaries needs to be considered as a contribution similar to the charged surface in films [7]. Hall effect measurements showed that both electron concentration and mobility decrease with a reduction of film thickness, which is ascribed to the scattering of electrons by crystal defects and interfaces and the effect of a native space charge region at the near-surface region of the films [29].

The conductivity of SnO_2 films is also dependent on the growth conditions, as the stoichiometry depends on the growth conditions such as oxygen partial pressure or substrate temperature [22].

2.2.3 Optical properties

The interest in SnO_2 coatings is due to the coexistence of high electrical conductivity and a high transparency in the visible range of the electromagnetic spectrum. Typical SnO_2 transmission spectra are shown in Fig. 2.4. At short wavelengths (high energies) electron-interband transitions from the valence band to the conduction band suppress the transmission. While for long wavelengths (low energies) light is reflected because of the plasma edge. The high transparency in the visible wavelength range of 400 - 800 nm was explained by a low concentration of mid-gap states, typically responsible for absorption of photons with energies below the band-gap energy [7].

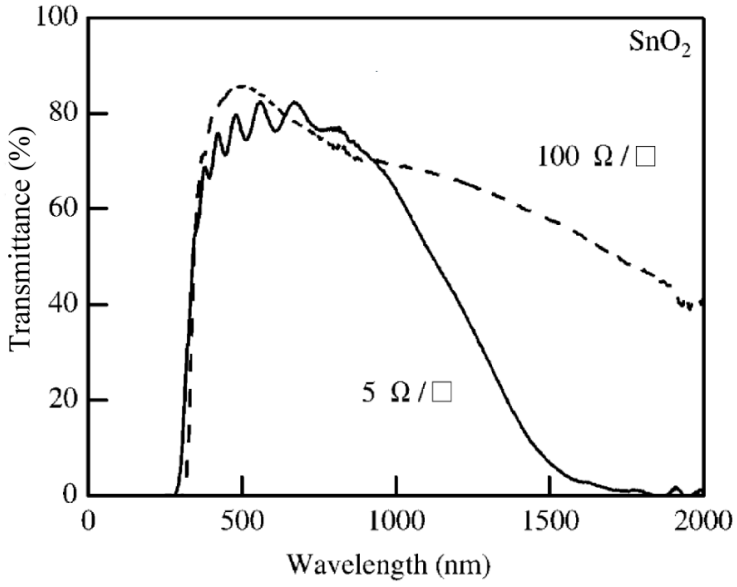

Fig. 2.4. Optical transmittance of SnO_2 films for different conductivity of the films. (From Ref. [30]).

Undoped SnO_2 films exhibit a larger band-gap, typically more than 3.6 eV. The nature of the lowest optical band gap of SnO_2 was heavily disputed for a long time. Theoretical prediction included an indirect gap [9, 31], a dipole-allowed direct gap as well as a dipole-forbidden direct gap [8, 11, 32]. Clarification was sought by performing optical experiments at low temperatures [14-16]. However, at low temperatures excitonic effects were dominating the spectra making the analysis more difficult. Consistent with most experiments is the band ordering suggested by Schleife. He proposed a direct gap at the Γ point. The conduction band edge is basically *s*-like and of Γ_1^+ symmetry in D_{4h} (using the notation of Koster) [33]. The valence bands comprised of O 2*p* and Sn 4*d* states exhibit the following ordering and symmetries $\Gamma_3^+, \Gamma_5^-, \Gamma_5^+, \Gamma_1^+, \Gamma_1^-$. The Γ_3^+ state is *d*-like, while the Γ_5^- state is *p*-like (Fig. 2.5). In particular, the states forming the lowest gap are of the same parity, thus the transition from $\Gamma_3^+ \rightarrow \Gamma_1^+$ is a dipole-forbidden direct transition, The transition from $\Gamma_5^- \rightarrow \Gamma_1^+$, which is about 0.7 eV higher in energy, is a dipole-allowed direct transition. However, it is forbidden for light polarized parallel to the *c*-axis of the rutile lattice.

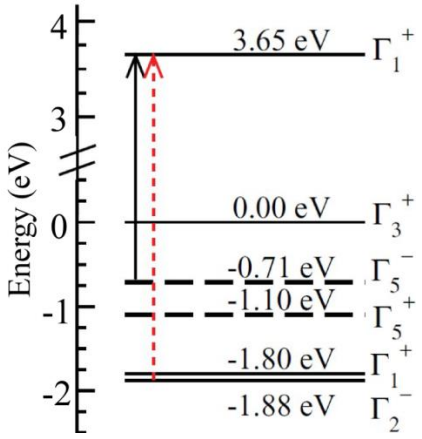

Fig. 2.5. Plot of the quasiparticle eigenvalues together with allowed optical transitions at the Γ point of the Brillouin zone. Dashed lines indicate a two-fold degeneracy of the respective level. Solid black (dotted red) arrows show dipole-allowed optical transitions for light polarized perpendicular (parallel) to the c axis of the rutile lattice. (from Ref. [8])

In the literature one finds different approaches of fitting the experimental optical data of transmittance / absorption results in order to extract the optical band gap of SnO_2. These depend on the temperature where the experiments were conducted as well as on the assumption made about the nature of the band gap. At temperatures above 200 °C excitonic effects appear to be negligible. In this temperature region fits have been performed mainly with so called Tauc-plots [34, 35], which are based on a *k·p*-perturbational description of the optical transition yielding

$$\alpha(h\nu) \propto A(h\nu - E_g)^{\frac{1}{2}}, \tag{2.1}$$

and

$$\alpha(h\nu) \propto A(h\nu - E_g)^{\frac{3}{2}} \tag{2.2}$$

for a dipole-allowed and a dipole-forbidden direct transition, respectively. Many authors use the former. In this thesis we use the latter in accordance with theory.

It should be noted that fits of the data assuming Urbach tails may also yield a good description of the experimental data in this temperature range [15]

$$\alpha \propto \alpha_0 \cdot \exp\left(\frac{b_0(h\nu - E_g)}{kT}\right). \tag{2.3}$$

Optical transmission of the conductive SnO_2 films is limited in the near infra-red (IR) region by free carrier absorption. The corresponding plasma wavelength (or plasma frequency) depends on the carrier concentration and carrier effective mass. The plasma frequency is given by

$$\omega_p = \left(\frac{ne^2}{\varepsilon_0 \varepsilon_\infty m^*}\right)^{1/2} \tag{2.4}$$

where n is the carrier concentration, e is the electron charge, ε_0 is the permittivity of free space, ε_∞ is the high frequency permittivity, and m^* is the electron effective mass. The high reflectivity in the near IR region below the plasma wavelength makes highly doped SnO_2 suitable as a low-emissivity window coating.

The wide band-gap of SnO_2 is of potential interest for UV optoelectronics. Its calculated exciton binding energy is 130 meV. This is much higher than the reported binding energy value of 60 meV for ZnO and of 25 meV for GaN [7, 36]. However, in experiments Reimann *et al.* found that the exciton binding energies of three excitons of SnO_2 were 32.76, 36.8, and 39.7 eV, respectively [37].

References

[1] L. Gracia, A. Beltran, J. Andres, *Characterization of the High-Pressure Structures and Phase Transformations in SnO_2. A Density Functional Theory Study,* The Journal of Physical Chemistry B, 111 (2007), 6479-6485.

[2] J. Haines, J.M. Léger, *X-ray diffraction study of the phase transitions and structural evolution of tin dioxide at high pressure: Relationships between structure types and implications for other rutile-type dioxides*, Physical Review B, 55 (1997), 11144-11154.

[3] G.J. McCarthy, J.M. Welton, *X-Ray Diffraction Data for SnO_2. An Illustration of the New Powder Data Evaluation Methods*, Powder Diffraction, 4 (1989), 156-159.
[4] J.G. Zheng, X. Pan, M. Schweizer, F. Zhou, U. Weimar, W. Göpel, M. Rühle, *Growth twins in nanocrystalline SnO_2 thin films by high-resolution transmission electron microscopy*, J. Appl. Phys., 79 (1996), 7688-7694.
[5] X.Q. Pan, L. Fu, *Oxidation and phase transitions of epitaxial tin oxide thin films on $(\bar{1}012)$ sapphire*, J. Appl. Phys., 89 (2001), 6048-6055.
[6] W.H. Baur, A.A. Khan, *Rutile-type compounds. IV. SiO_2, GeO_2 and a comparison with other rutile-type structures*, Acta Crystallographica Section B, 27 (1971), 2133-2139.
[7] H. Hosono, D.C. Paine, *Handbook of Transparent Conductors*, Springer, New York Heidelberg Dordrecht London, (2010).
[8] A. Schleife, J.B. Varley, F. Fuchs, C. Rödl, F. Bechstedt, P. Rinke, A. Janotti, C.G. Van de Walle, *Tin dioxide from first principles: Quasiparticle electronic states and optical properties*, Physical Review B, 83 (2011), 035116.
[9] F.J. Arlinghaus, *Energy bands in stannic oxide (SnO_2)*, Journal of Physics and Chemistry of Solids, 35 (1974), 931-935.
[10] J.G. Gay, W.A. Albers, F.J. Arlinghaus, *Irreducible representations of the little groups of D^{14}_{4h}*, Journal of Physics and Chemistry of Solids, 29 (1968), 1449-1459.
[11] J.L. Jacquemin, G. Bordure, *Band structure and optical properties of intrinsic tetragonal dioxides of groups-IV elements*, Journal of Physics and Chemistry of Solids, 36 (1975), 1081-1087.
[12] J. Robertson, *Electronic structure of SnO_2, GeO_2, PbO_2, TeO_2 and MgF_2*, Journal of Physics C: Solid State Physics, 12 (1979), 4767.
[13] K.C. Mishra, K.H. Johnson, P.C. Schmidt, *Electronic structure of antimony-doped tin oxide*, Physical Review B, 51 (1995), 13972-13976.
[14] M. Nagasawa, S. Shionoya, *Zeeman Effect and Symmetry of the Intrinsic SnO_2 Exciton*, Phys. Rev. Lett., 21 (1968), 1070-1073.
[15] M. Nagasawa, S. Shionoya, *Urbach's rule exhibited in SnO_2*, Solid State Commun., 7 (1969), 1731-1733.
[16] D. Fröhlich, R. Kenklies, R. Helbig, *Band-Gap Assignment in SnO_2 by Two-Photon Spectroscopy*, Phys. Rev. Lett., 41 (1978), 1750-1751.
[17] V.T. Agekyan, *Spectroscopic properties of semiconductor crystals with direct forbidden energy gap*, physica status solidi (a), 43 (1977), 11-42.
[18] P. Barbarat, S.F. Matar, *First-principles investigations of the electronic, optical and chemical bonding properties of SnO_2*, Computational Materials Science, 10 (1998), 368-372.
[19] M.A. Mäki-Jaskari, T.T. Rantala, *Band structure and optical parameters of the SnO_2 (110) surface*, Physical Review B, 64 (2001), 075407.
[20] R. Summitt, J.A. Marley, N.F. Borrelli, *The ultraviolet absorption edge of stannic oxide (SnO_2)*, Journal of Physics and Chemistry of Solids, 25 (1964), 1465-1469.
[21] M. Nagasawa, S. Shionoya, *Temperature Dependence of the Fundamental Optical Absorption Edge in Stannic Oxide*, J. Phys. Soc. Jpn., 30 (1971), 1118-1123.
[22] Y.M. Lu, J. Jiang, C. Xia, B. Kramm, A. Polity, Y.B. He, P.J. Klar, B.K. Meyer, *The influence of oxygen flow rate on properties of SnO_2 thin films grown epitaxially on c-sapphire by chemical vapor deposition*, Thin Solid Films, 594 (2015), 270-276.
[23] G. Sanon, R. Rup, A. Mansingh, *Band-gap narrowing and band structure in degenerate tin oxide (SnO_2) films*, Physical Review B, 44 (1991), 5672-5680.
[24] Y. Mi, H. Odaka, S. Iwata, *Electronic Structures and Optical Properties of ZnO, SnO_2 and In_2O_3*, Jpn. J. Appl. Phys., 38 (1999), 3453.

[25] K.J. Button, C.G. Fonstad, W. Dreybrodt, *Determination of the Electron Masses in Stannic Oxide by Submillimeter Cyclotron Resonance*, Physical Review B, 4 (1971), 4539-4542.

[26] Ç. Kılıç, A. Zunger, *Origins of Coexistence of Conductivity and Transparency in SnO_2*, Phys. Rev. Lett., 88 (2002), 095501.

[27] C.G. Fonstad, R.H. Rediker, *Electrical Properties of High-Quality Stannic Oxide Crystals*, J. Appl. Phys., 42 (1971), 2911-2918.

[28] J.E. Dominguez, X.Q. Pan, L. Fu, P.A. Van Rompay, Z. Zhang, J.A. Nees, P.P. Pronko, *Epitaxial SnO_2 thin films grown on $(\bar{1}012)$ sapphire by femtosecond pulsed laser deposition*, J. Appl. Phys., 91 (2002), 1060-1065.

[29] J.E. Dominguez, L. Fu, X.Q. Pan, *Effect of crystal defects on the electrical properties in epitaxial tin dioxide thin films*, Appl. Phys. Lett., 81 (2002), 5168-5170.

[30] D.S. Ginley, C. Bright, *Transparent Conducting Oxides*, MRS Bulletin, 25 (2000), 15-18.

[31] A. Svane, E. Antoncik, *Electronic structure of rutile SnO_2, GeO_2 and TeO_2*, Journal of Physics and Chemistry of Solids, 48 (1987), 171-180.

[32] J.M. Themlin, R. Sporken, J. Darville, R. Caudano, J.M. Gilles, R.L. Johnson, *Resonant-photoemission study of SnO_2: Cationic origin of the defect band-gap states*, Physical Review B, 42 (1990), 11914-11925.

[33] G.F. Koster, *Properties of the thirty-two point groups*, The MIT Press, (1963).

[34] J. Tauc, R. Grigorovici, A. Vancu, *Optical Properties and Electronic Structure of Amorphous Germanium*, physica status solidi (b), 15 (1966), 627-637.

[35] J. Tauc, *Optical properties and electronic structure of amorphous Ge and Si*, Mater. Res. Bull., 3 (1968), 37-46.

[36] B. Yu, C. Zhu, F. Gan, *Exciton spectra of SnO_2 nanocrystals with surficial dipole layer*, Optical Materials, 7 (1997), 15-20.

[37] K. Reimann, M. Steube, *Experimental determination of the electronic band structure of SnO_2*, Solid State Commun., 105 (1998), 649-652.

3 Chemical vapor deposition: principle and film deposition

As mentioned in the introduction, various methods have been employed to grow SnO_2 films, such as ALD, PLD, MBE, sputter deposition, MOCVD, spray pyrolysis etc. Many of these techniques suffer from one or more drawbacks such as a low deposition rate, a prolonged post processing (e.g. annealing) time, or expensive targets, precursors, and apparatus. CVD is a favorable technique and suitable for commercial exploitation since it is based on an inexpensive and versatile process capable of producing films of high quality at a high growth rate. Several groups have used a CVD process to produce SnO_2 thin films employing SnI_4 or $SnCl_4$ (Sn^{4+}) as the Sn precursor [1, 2]. In this work we have attempted to use SnI_2 (Sn^{2+}) as Sn precursor to achieve SnO_2 and also SnO films by CVD. However, we have not succeeded in growing SnO. The reason we will explain in section 3.2. We have also tried to employ pure-metal tin as tin precursor. Although the melting point is only 232 °C for metallic tin, we found, even when the temperature of the precursor reservoir reached 900 °C, that the evaporation rate of metal tin was only about 0.004 g/h and the growth rate of the film was very low, and again no SnO was obtained. In this chapter, we first briefly introduce the basic principle of CVD and the specific setup used in this work, then describe the typical experimental parameters for the deposition of SnO_2 films.

3.1 CVD principle and apparatus

In the broadest sense chemical vapor deposition involves the formation of a thin solid film on a substrate material by a chemical reaction of vapor-phase precursors. The chemical reactions of precursors occur in the gas phase and the product is deposited on to the substrate. The reactions can be promoted by heat (thermal CVD), higher frequency radiation such as UV (photo-assisted CVD) or plasma (plasma-enhanced CVD). In this thesis all the results are based on thermally activated chemical vapor deposition and the thermal energy is applied from the furnaces surrounding the reactor tube (hot-wall CVD). In thermal CVD, the film growth rate is determined by several parameters: the temperature of the substrate (reaction zone), the operating pressure of the reactor, and the composition and chemistry of the gas-phase, etc. The most important one of these parameters is the substrate temperature. The dependence of the SnO_2 film growth rate on substrate

temperature is shown in section 5.1 in Fig. 5.1. The dependence on the O_2 flow rate is discussed in section 6.2.1 in Fig. 6.6. A more detailed background and introduction to CVD techniques can be found in Ref. [3].

Fig. 3.1. Mini CVD reactor (left) and CVD1 reactor (right).

Two vertical, hot-wall CVD reactors (mini CVD and CVD1), which were built at the I. Physikalisches Institut (IPI) of Justus-Liebig-University Gießen, are used for the SnO_2 film deposition (in Fig. 3.1). A schematic representation of the CVD1 reactor is shown in Fig. 3.2. It consists of a five-temperature-zones furnace which is completely equipped with quartz tubes. The five temperature zones can be controlled individually and are suitable for temperatures up to 1100 °C. Powder tin iodide (SnI_2, 99 + %, from Alfa Aesar Company) was filled into the reservoir. The SnI_2 evaporation rate was controllable in the range from 0.005 to 0.7 g/h through regulating the temperature of the reservoir in the range from 270 to 450 °C. The SnI_2 vapor was transported towards the reaction zone by an argon carrier gas (99.999%), which flowed in an inner quartz tube. The substrates were cleaned with acetone, methanol, and pure water consecutively in an ultrasonic bath, each for 15 min, and then blown dry with nitrogen gas and placed onto a sample holder made of quartz glass which is approximately 5 cm apart from the orifice of that separate tube. The sample holder was rotated at about 15 rpm during the deposition to improve the film homogeneity. Molecular oxygen gas (99.999%) was used as the oxygen precursor, and the O_2 gas flow was varied from 0 to 50 sccm for the film deposition in this apparatus (from 0 to 65 sccm in the mini CVD). Prior to film deposition, the chamber was evacuated to 0.1 mbar. The pressure during the deposition was kept at 30 - 40 mbar. In order to achieve a constant temperature of the deposition zone, the whole chamber was heated for about one hour prior

to deposition. The films were deposited at a substrate temperature between 300 and 950 °C for 0.5 to 7.2 h with thicknesses of 0 to 8 µm. Almost all deposited films are transparent, if the films thickness is less than 1 µm. However, if the films are really epitaxial single crystals on sapphire substrates, even films with thickness larger than 4 µm will be still transparent (see chapter 8 for details).

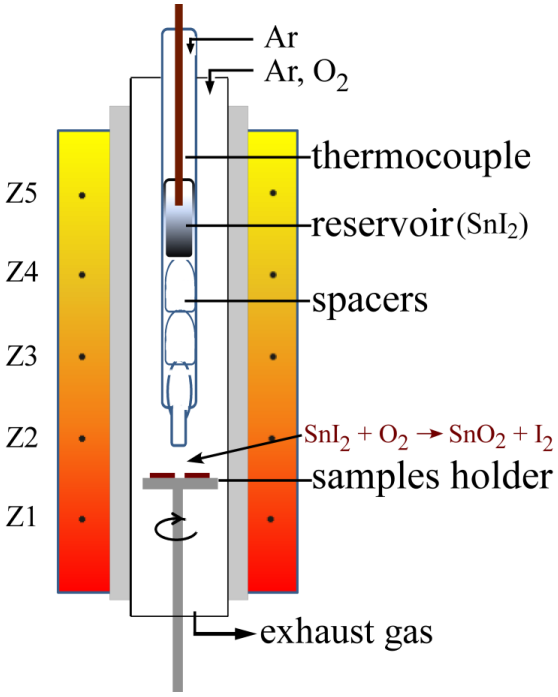

Fig. 3.2. Schematic representation of the five-temperature-zone reactor of CVD1.

The mini CVD is a much simpler apparatus than the CVD1. The chamber design of the mini CVD is similar to that of the CVD1. However, the furnace of the mini CVD consists of one part only and cannot be separately controlled. The reservoir temperature is controlled by the furnace, and the substrate is heated with a halogen lamp, therefore the maximal stable temperature of the substrates that can be reached is only about 750 °C. The substrate holder cannot be rotated.

More information about these CVD apparatuses used can be found in Refs. [4, 5].

3.2 Film deposition

During the course of this study, SnO_2 films were prepared by CVD on different types of substrates, i.e. quartz glass, *c*-plane and *r*-plane sapphire substrates with the setups described above.

Table 3.1. Summary of typical experimental parameters for deposition of SnO_2 films in the chamber of the mini CVD system.

substrate	substrate temperature (°C)	SnI_2 evaporation rate (g/h)	O_2 gas flow rate (sccm)	pressure (during deposition) (mbar)	deposition rate (nm/h)
c-sapphire	510	0.016	5	7.0	37
	510	0.016	10	7.0	67
	270-700	0.016	20	7.0	130 (510 °C)
	510-650	0.016	40	7.0	244 (510 °C)
	510	0.016	60	7.0	290
r-sapphire	300-700	0.02-0.03	0; 1.5; 5; 10; 15; 20; 25; 30; 40; 50; 60; 65	7.0	-

Table 3.2. Summary of typical experiment parameters for deposition of SnO_2 films in the chamber of the CVD1 system.

substrate	substrate temperature (°C)	SnI_2 evaporation rate (g/h)	O_2 gas flow rate (sccm)	pressure (during deposition) (mbar)	deposition rate (nm/h)
quartz glass	450-850	0.005-0.25	1 - 40	30;40	-
r-sapphire	450-850	0.005-0.25	1 - 40	30;40	-
c-sapphire	450-850	0.005-0.25	1 - 40	30;40	-
quartz glass	900	0.7	40	30	~4000
r-sapphire	900	0.7	40	30	~2000
c-sapphire	900	0.7	40	30	~1800

As will be discussed in the following chapters, the deposition parameters have a strong influence on the properties of the films. Typical deposition parameters used in the present

study are summarized in the Table 3.1 and 3.2 for the chamber of the mini CVD system and CVD1 system, respectively.

Because tin may have different oxidation states, both Sn(II)O and Sn(IV)O_2 are possible products of the oxidation of SnI_2 according to reactions (3.1) and (3.2), respectively:

$$SnI_2 + \frac{1}{2} O_2 = SnO + I_2 \quad (3.1)$$

$$SnI_2 + O_2 = SnO_2 + I_2. \quad (3.2)$$

Therefore, the Gibbs free energy changes ΔG of SnO and SnO_2 formation are calculated by the software HSC Chemistry based on Eq. (3.3):

$$\Delta G = \Delta H - T \times \Delta S. \quad (3.3)$$

Here ΔH and ΔS are the enthalpy and entropy changes of the reactions, respectively. T is the absolute temperature of the reaction. As shown in Fig. 3.3, the formation of SnO_2 shows a lower Gibbs energy change compared with the formation of SnO in the temperature range of 500 - 1300 K. This means that the formation of SnO_2 is thermodynamically favored over SnO. Consistent with this consideration, only SnO_2 is identified as the reaction product without any SnO precipitates in our deposited films based on the XRD, XPS, and Raman spectroscopy results.

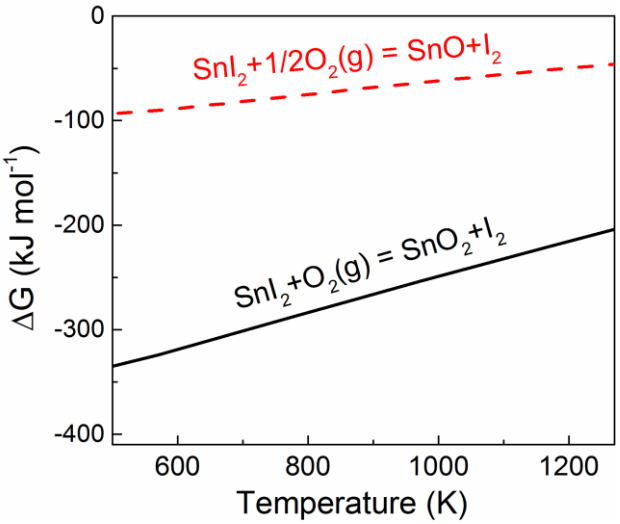

Fig. 3.3. The Gibbs free energy changes of SnO and SnO_2 formation as a function of reaction temperature.

In both reactions (3.1) and (3.2) molecular iodine (I_2) should also be produced. As no iodine could be detected by both XRD and XPS in any of the deposited films, we conclude

that iodine is not incorporated into the SnO_2 films, and the I_2 vapor is evacuated during the deposition.

References

[1] J. Sundqvist, M. Ottosson, A. Hårsta, *CVD of Epitaxial SnO_2 Films by the SnI_4/O_2 Precursor Combination*, Chemical Vapor Deposition, 10 (2004) 77-82.
[2] R.N. Ghoshtagore, *Mechanism of CVD Thin Film SnO_2 Formation*, J. Electrochem. Soc., 125 (1978) 110-117.
[3] A.C. Jones, M.L. Hitchman, *Chemical Vapour Deposition: Precursors, Processes and Applications*, Royal Society of Chemistry, UK, (2009).
[4] C. Neumann, *Homoepitaxie von ZnO*, PhD thesis, I. Physikalisches Institut, Justus-Liebig-Universität Giessen, (2006).
[5] S. Eisermann, *Chemische Gasphasenepitaxie von Zinkoxid und Kupferoxid*, PhD thesis, I. Physikalisches Institut, Justus-Liebig-Universität Giessen, (2011).

4 Characterization methods: principles and instruments

Several methods have been used to characterize the films deposited in this work. For structural characterization, X-ray diffraction (XRD), high-resolution X-ray diffraction (HRXRD), X-ray reflectometry (XRR), and Raman spectroscopy were employed. The surface and morphology analyses were accomplished by atomic force microscopy (AFM) and scanning electron microscopy (SEM). The chemical stoichiometry of the films was determined by X-ray photoelectron spectroscopy (XPS). The optical and electrical properties of the films were obtained by optical transmission, photoluminescence (PL) spectroscopy, and Hall-effect measurements. In this chapter, the main principles of these techniques, and the specific instruments and typical measurement conditions (parameters) used in this work are briefly described.

4.1 Structural characterization methods

4.1.1 X-ray diffraction

X-ray diffraction is a powerful non-destructive method for material characterization, by which the crystal structure, orientation, grain size as well as lattice parameters (in-plane and out-of-plane), strain/relaxation, thickness and defect concentration of epitaxial thin films etc. can be determined [1, 2]. These measurements are possible because the incident X-ray beam wavelength (0.7 - 2.5 Å) is comparable with the distance between two adjacent atoms of the lattice, which is a few angstroms. The penetration depth of XRD is of the order of μm. Therefore, the crystalline structure of thin films is detected as well as that of the underlying substrate. Because of this capability, the structure relationship between film and substrate can be estimated using XRD results.

When X-rays impinge on a crystal, the individual atoms act as secondary radiation emitters and cause interference analogous to the diffraction of light from a grating. Constructive interferences give the diffraction peaks according to Bragg's law,

$$2d_{hkl}\sin\theta = n\lambda, \tag{4.1}$$

where d_{hkl} denotes the interplanar distance of the lattice planes (*hkl*), θ is the incident angle and λ is the diffracted X-ray wavelength.

Many types of X-ray measurements have been carried out on the thin films: θ-2θ (symmetrical) and ω-2θ scans (asymmetrical), rocking curves, pole figures, ϕ-scan, grazing incidence in-plane diffraction (GIID), and reciprocal space mapping (RSM). A large number of publications on X-ray diffraction techniques can be found in Refs. [3-5]. Here we give some information only closely related to this dissertation.

A standard Bragg-Brentano powder diffractometer, Siemens D5000, at the I. Physikalische Institut (IPI) of University Giessen is used for standard characterization of the films [6]. Depending on the coupling of the sample and/or detector rotations during diffraction measurements, two scan modes, i.e., θ-2θ scan and rocking curve scan are typically employed for structural characterizations using this machine.

In a θ-2θ scan, the reflections from the planes parallel to the substrate surface are detected. This allows one to determine the lattice constant in the orientation along the growth direction of an epitaxial layer or polycrystalline film with respect to the substrate, as well as the crystallite size (D). The crystallite size is associated with the coherent crystal length and is deduced from θ-2θ patterns using the Scherrer formula,

$$D = \frac{\kappa\lambda}{\beta \cdot \cos\theta}, \tag{4.2}$$

where θ is the Bragg angle, k is a correcting coefficient depending on the experimental setup and the crystallite shape. It is considered equal to 0.9 in the present case, λ is the wavelength of the X-ray source, and β (in radians) is the full width at half maximum (FWHM) of the peak.

In the rocking curve mode, known also as ω-scan, the sample is "rocked" by a small angle around the Bragg angle θ with the detector remaining at a fixed position (2θ). The half width of the rocking curve is a direct measure of the range of orientation present in the crystal, thus, it is commonly used for evaluating the out-of-plane ordering of the epitaxial layers.

Four-circle X-ray diffraction

For an assessment of the quality of an epitaxial layer a four-circle X-ray diffractometer is necessarily required. In a four-circle X-ray diffractometer, the sample can be rotated in three planes, i.e., ω, ϕ, and χ-circles, as indicated in Fig. 4.1, plus the 2θ-circle for detector rotation, the diffractometer is thus called four-circle diffractometer.

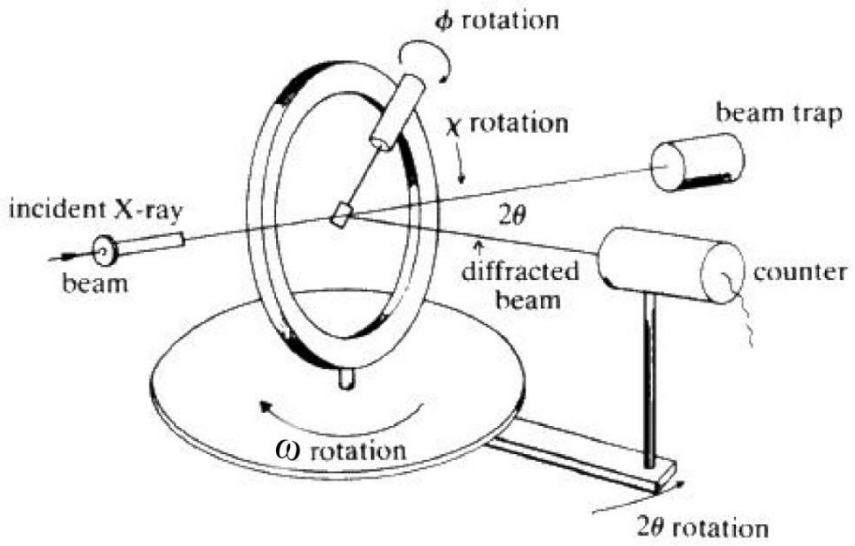

Fig. 4.1. Schematic illustration of the configuration of a four-circle X-ray diffractometer.

A Bruker D8 Discover four-circle diffractometer with Cu $K_{\alpha 1}$ (λ =1.54060 Å) radiation, in the Faculty of Materials Science and Engineering, Hubei University, China, was employed for characterization of epitaxially grown thin films on sapphire substrates. Information concerning the in-plane orientation relationships between the films and substrates can be obtained from HRXRD ϕ-scans. Analyzing the 2θ values of different planes of a SnO_2 film the lattice parameters of this film can be determined using the orthorhombic crystal geometry equation,

$$\frac{1}{d_{hkl}^2} = \frac{h^2}{a^2} + \frac{k^2}{b^2} + \frac{l^2}{c^2}. \tag{4.3}$$

SnO_2 has tetragonal symmetry, but due to the possible strain stress in the deposited films, the lattice parameter *a* may nevertheless not be equal to *b*. Therefore we use the orthorhombic crystal geometry equation to substitute the tetragonal geometry equation.

Some X-ray diffraction measurements of high-quality SnO_2 films on *c*-sapphire were mainly carried out at the Institute of Experimental Physics of Magdeburg University. A Seifert/FPM URD6/TZ6 four-circle X-ray diffractometer, equipped with a Cu K_α X-ray source, Barthels primary monochromator, Eulerian cradle sample stage, and a Ge (220) secondary analyzer was applied for the ϕ-χ scan (pole figure) measurements. Grazing incidence diffraction was accomplished with a Seifert/FPM URD6 four-circle diffractometer, equipped with a Cu K_α radiation source, a primary vertical Soller collimator, a vertical translation sample holder, and a secondary vertical Soller collimator and LiF analyzer.

For grazing incidence X-ray diffraction (GIXRD), the detector scan mode is always adopted. Under grazing incidence conditions, with an incident angle of lower than 1°, the incident X-ray beam is nearly parallel to the film surface, thus the reflections generated from the planes perpendicular to the surface are detected. By grazing incidence ω- or ϕ-scans, the in-plane orientation of the films with respect to the substrates can be directly determined. Depth sensitivity was obtained via the different acceptance angles of the sample for the incoming divergent light.

The scan mode mapping a two-dimensional region of reciprocal space is known as reciprocal space map (RSM). Such a scan can be carried out by combining the 2θ-ω scan mode with the ω-scan mode in the following way: first, for a given length of the scattering angle an ω-scan is performed, the 2θ-ω scan mode is employed to change the length of the scattering vector by a small amount, then again an ω-scan is performed and so forth. RSMs were recorded with a GE/Seifert URD6 diffractometer equipped with a Ge (220) channel cut compressor, and a Braun position sensitive detector. The result of such a scan conducted at the position of the (200), (420), and (411) reflections of the SnO_2 thin films are shown in section 6.3.

4.1.2 X-ray reflectometry

X-ray reflectometry is now a well-established method for the study of surfaces and thin layers, since it provides a wealth of information on thickness and interfacial properties on the nanometer scale, like layer thickness, the layer's electronic densities, surface and interface roughness and morphology.

In this study the XRR measurements were performed with the same diffractometer at University Giessen as used for X-ray powder diffraction, equipped with a modified sample stage, designed specially for XRR by Bruker AXS. The XRR measurements, at grazing incidence θ-2θ scan mode, of our SnO_2 films were typically carried out from $2\theta = 0.35°$ to 2.5° with a scan step of 0.002°. Afterwards, the program "Refsim"[7] was used to simulate the experimental curve, to obtain thickness, surface density, and roughness of the interfaces between the layer and substrate. Although the described setup allows the measurement of film thicknesses up to about 300 nm for a very smooth surface, we can, in practice, measure only films with thicknesses of less than 150 nm, due to the rough surfaces of the films.

More detailed theoretical background on X-ray reflectivity and an introduction to practical X-ray reflectometry techniques can be found in Refs. [6, 8-10].

4.1.3 Raman spectroscopy

Raman spectroscopy yields information about the symmetry, structure, defects, and phase of a crystal. Variations in phonon mode intensities, line widths, line shapes, and frequencies can be used to study the crystal quality and structure as well as to prove the existence of defects and impurities. Angle-dependent Raman spectra reveal the symmetry properties of the vibrational modes and thus the symmetry of the crystalline material under study. Tin dioxide has a tetragonal rutile structure (space group D_{4h}^{14}, $P4_2/mnm$) with two SnO_2 molecules per primitive unit cell. The symmetry character of the 15 optical phonon branches at the Γ point of the Brillouin zone may be derived by group theory:

$$\Gamma_{\text{rutile}} = A_{1g} + A_{2g} + A_{2u} + B_{1g} + B_{2g} + 2B_{1u} + E_g + 3E_u, \qquad (4.4)$$

where the modes of A_{1g}, B_{1g}, B_{2g}, and E_g symmetry are Raman active [11, 12]. Fig. 4.2 shows the motions of oxygen anions with respect to stationary tin cations, either perpendicular to the *c* axis (modes A_{1g} and B_{2g}) or parallel to the *c* axis (mode E_g) [13].

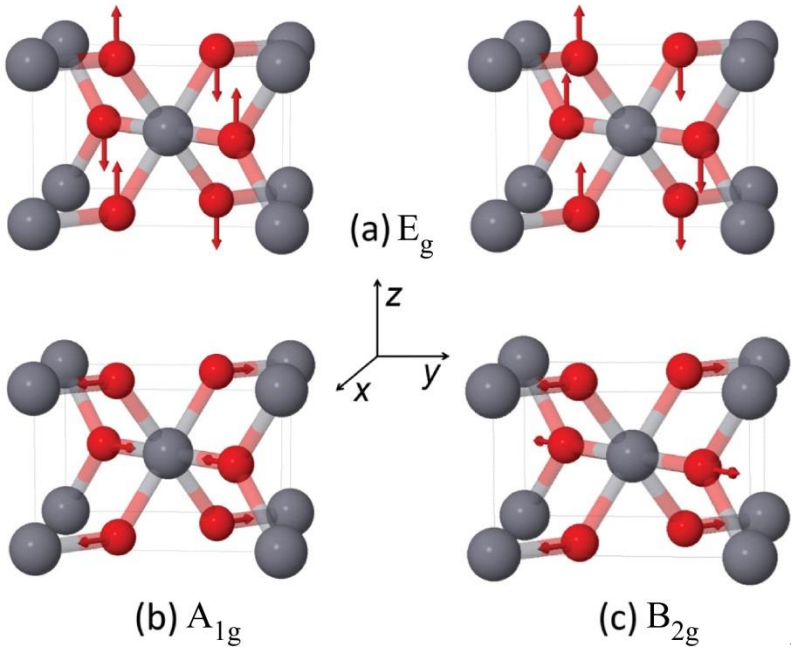

Fig. 4.2. Oxygen atom displacements for Raman active modes. (from Ref. [13])

The Raman tensors $\hat{R}$ of the phonons in rutile symmetry of SnO_2 have the following matrix form [14-16]:

$$\hat{R}(A_{1g}) = \begin{pmatrix} a & 0 & 0 \\ 0 & a & 0 \\ 0 & 0 & b \end{pmatrix}, \quad \hat{R}(B_{1g}) = \begin{pmatrix} c & 0 & 0 \\ 0 & -c & 0 \\ 0 & 0 & 0 \end{pmatrix}, \quad \hat{R}(B_{2g}) = \begin{pmatrix} 0 & d & 0 \\ d & 0 & 0 \\ 0 & 0 & 0 \end{pmatrix},$$

$$\hat{R}(\mathrm{E_{g,1}}) = \begin{pmatrix} 0 & 0 & 0 \\ 0 & 0 & e \\ 0 & e & 0 \end{pmatrix}, \hat{R}(\mathrm{E_{g,2}}) = \begin{pmatrix} 0 & 0 & e \\ 0 & 0 & 0 \\ e & 0 & 0 \end{pmatrix}. \quad (4.5)$$

The scattered Raman intensity of a non-degenerated mode *k* is proportional to

$$I(k) \propto \left|\vec{e}_s^T \hat{R}(k) \vec{e}_i\right|^2, \quad (4.6)$$

where $\vec{e}_i$ and $\vec{e}_s$ denote unit vectors representing the polarization of the incident and scattered radiation, respectively. The total scattered intensity of the twofold-degenerated mode of E_g symmetry character is given by:

$$I \propto \left|\vec{e}_s^T \hat{R}\ (\mathrm{E_{g,1}}) \vec{e}_i\right|^2 + \left|\vec{e}_s^T \hat{R}\ (\mathrm{E_{g,2}}) \vec{e}_i\right|^2. \quad (4.7)$$

The parameters *a*, *b*, *c*, *d*, and *e* are Raman tensor elements which may be nonzero [14].

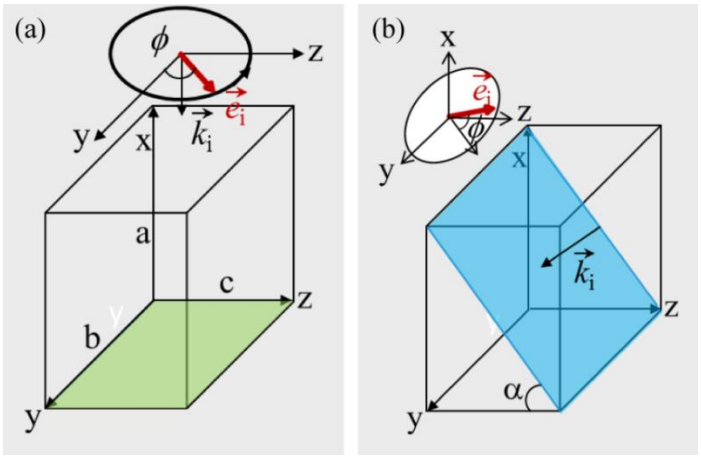

Fig. 4.3. Schematic illustration of the orientation of the wave vector $\vec{k}_i$ and the polarization vector $\vec{e}_i$ for a rotation of SnO_2 film about the normal of the (100)-plane on *c*-sapphire (a), and about the normal of the (101)-plane on *r*-sapphire (b).

The intensity dependence of the Raman-active lattice vibrations on the rotation of the films is studied in this work. Fig. 4.3 schematically illustrates the orientation of the wave vector $\vec{k}_i$ and the polarization vector $\vec{e}_i$ of the excitation laser for a rotation of the film about the axis defined by the excitation laser ($\vec{k}_i$). In the case of SnO_2 film on *c*-sapphire, the wave vector is aligned parallel to the *x* axis (Fig. 4.3a). The wave vector is the normal to the (101)-plane, when the incident laser irradiates the SnO_2 film on *r*-sapphire, i.e., the polarization vector lies in the (101)-plane (Fig. 4.3b). To calculate the intensity dependence of the Raman-active phonons on the rotation angle, the polarization vectors are represented in polar coordinates, e.g., a vector rotating in the (100)-plane about the *x* axis has the form:

$$\vec{e}_i = \begin{pmatrix} 0 \\ \cos\phi \\ \sin\phi \end{pmatrix}, \quad (4.8)$$

where ϕ is the rotation angle between incident polarization vector $\vec{e}_i$ and the *y* axis. The polarization of the scattered light may now be analyzed parallel or perpendicularly to the incident one, thus one obtains in polar coordinates:

$$\vec{e}_s^{\parallel} = \begin{pmatrix} 0 \\ \cos\phi \\ \sin\phi \end{pmatrix}, \tag{4.9}$$

and

$$\vec{e}_s^{\perp} = \begin{pmatrix} 0 \\ -\sin\phi \\ \cos\phi \end{pmatrix}, \tag{4.10}$$

where $\parallel$ and $\perp$ denote parallel and perpendicularly oriented incident and scattered polarization vectors, respectively. Inserting these polarization vectors and the Raman tensors of tetragonal SnO_2 in equations (4.6) or (4.7) yields the intensity dependence on sample rotation about the *x* axis for SnO_2 film on *c*-sapphire. For example, one obtains for modes of A_{1g} symmetry character:

$$\begin{aligned} I^{\parallel}(A_{1g}) &\propto \left| \begin{pmatrix} 0 \\ \cos\phi \\ \sin\phi \end{pmatrix} \begin{pmatrix} a & 0 & 0 \\ 0 & a & 0 \\ 0 & 0 & b \end{pmatrix} \begin{pmatrix} 0 \\ \cos\phi \\ \sin\phi \end{pmatrix} \right|^2 \\ &\propto \left| \tfrac{1}{2}(a+b) + \tfrac{1}{2}(a-b)\cos(2\phi) \right|^2. \end{aligned} \tag{4.11}$$

The intensity dependence of any Raman-active SnO_2 phonons on the sample rotation about the normal of the (100)- and (101)-plane can be determined. The related outcomes of the calculations are listed in Table 4.1) and (4.2).

Table 4.1. Theoretical dependence of the scattered intensity of Raman-active SnO_2 phonons on the sample rotation around the normal of the (100)-plane for parallel ($\vec{e}_i \parallel \vec{e}_s$) and perpendicular ($\vec{e}_i \perp \vec{e}_s$) oriented incident and scattered polarization vectors $\vec{e}_i$ and $\vec{e}_s$, respectively. The rotation angle is given by ϕ.

	Scattered Raman intensity upon the sample rotation of SnO_2 film about the normal of (100)-plane	
Mode	$\vec{e}_i \parallel \vec{e}_s$	$\vec{e}_i \perp \vec{e}_s$
A_{1g}	$\frac{1}{4}\lvert a+b+(a-b)\cos(2\phi)\rvert^2$	$\frac{1}{4}\lvert a-b\rvert^2\sin^2(2\phi)$
B_{1g}	$\lvert c\rvert^2\cos^4\phi$	$\frac{1}{4}\lvert c\rvert^2\sin^2(2\phi)$
B_{2g}	0	0
E_g	$\lvert e\rvert^2\sin^2(2\phi)$	$\lvert e\rvert^2\cos^2(2\phi)$

Table 4.2 Theoretical dependence of the scattered intensity of Raman-active SnO_2 phonons on the sample rotation around the normal of the (101)-plane for parallel ($\vec{e}_i \parallel \vec{e}_s$) and perpendicular ($\vec{e}_i \perp \vec{e}_s$) oriented incident and scattered polarization vectors $\vec{e}_i$ and $\vec{e}_s$, respectively. The rotation angle is given by ϕ.

	Scattered Raman intensity upon the sample rotation of SnO_2 film about the normal of the (101)-plane	
Mode	$\vec{e}_i \parallel \vec{e}_s$	$\vec{e}_i \perp \vec{e}_s$
A_{1g}	$\lvert a\cos^2\phi + (0.69a + 0.31b)\sin^2\phi\rvert^2$	$0.024\lvert b-a\rvert^2\sin^2(2\phi)$
B_{1g}	$\lvert c\rvert^2\lvert(0.69\sin^2\phi - \cos^2\phi)\rvert^2$	$0.71\lvert c\rvert^2\sin^2(2\phi)$
B_{2g}	$0.69\lvert d\rvert^2\sin^2(2\phi)$	$0.69\lvert d\rvert^2\cos^2(2\phi)$
E_g	$\lvert e\rvert^2(0.31\sin^2(2\phi) + 0.86\sin^4\phi)$	$\lvert e\rvert^2(0.31\cos^2(2\phi) + 0.21\sin^2(2\phi))$

Raman spectra were recorded in backscattering geometry at room temperature (300 K) using a Renishaw inVia Raman microscope at IPI of University Giessen. A linearly polarized laser with a wavelength of 532 nm was used for excitation and focused onto the surface of the sample with a 50× objective. The same objective was used to collect the scattered light, which was then dispersed by a spectrometer with a focal length of 250 mm and detected by a charge-coupled device (CCD) camera. The system's spectral resolution is limited to 5.1 cm^{-1}. To measure the angle-dependent Raman spectra, a microscope stage rotating about the axis defined by the direction of the incoming excitation laser was used. A polarization filter combined with a half-wave plate in the optical path of the scattered light from the sample was used to select parallel or perpendicularly polarized light with respect to the polarization vector of the excitation laser.

For a more detailed description of Raman techniques and practical applications in material research refer to Refs. [16, 17].

4.2 Surface and morphology characterization methods

4.2.1 X-ray photoelectron spectroscopy

X-ray photoelectron spectroscopy (XPS), also known as electron spectroscopy for chemical analysis (ESCA), is an extremely surface sensitive quantitative spectroscopic technique that measures the elemental composition at the parts per thousand ranges and allows one to determine the chemical state and electronic state of the elements which are present within a material. Surface analysis by XPS is accomplished by irradiating a sample in vacuum with monoenergetic soft X-rays or ultraviolet radiation and analyzing the energy of the detected electrons. Mg K_α (1253.6 eV) or Al K_α (1486.6 eV) X-rays radiation are usually used for XPS. These photons interact with atoms in the surface region of the sample, causing electrons to be emitted by the photoelectric effect. The emitted electrons have measured kinetic energies, E_K given by:

$$E_k = h\nu - E_B - \phi_{s,} \tag{4.12}$$

where $h\nu$ is the photon energy, E_B is the binding energy of the atomic orbital from which the electron originates, and ϕ_s is the spectrometer work function. The spectrum is obtained as a plot of the number of detected electrons per energy interval versus their kinetic energy.

XPS experiments in the present study were carried out using a SPECS PHOIBOS 150 system at photon energy of 1486.61 eV (Al $K\alpha$ radiation), at a base pressure of about 2×10^{-10} mbar. Detailed XPS investigations on the deposited SnO_2 films in this work are discussed in the subsection 6.2.4. More information about photoemission and practical applications of ESCA can be found for example in Refs. [18] and [19].

4.2.2 Scanning electron microscopy

The scanning electron microscope is one of the most versatile instruments available for the examination and analysis of microstructure morphology and chemical composition of solids. Image formation in the SEM is dependent on the acquisition of signals produced by the electron beam and specimen interaction. A variety of signals, mainly secondary plus backscattered electrons and X-rays, are produced, when the electron beam hits the surface of the specimen. Using special detectors, these signals can be collected giving specific information about the irradiated volume. We used an SEM equipped with a thermal field emission source and a secondary electron detector. The acceleration voltage between cathode and anode is commonly of the order of magnitude of 0.5 to 30 kV, and the

apparatus requires an extreme vacuum in the column of the microscope, which allows electron travel without scattering by the residual gas molecules or atoms.

Secondary electrons are emitted from the atoms located at the top surface of the specimen (~ 5 nm), and having low binding energies, typically around 3 to 5 eV. They produce a readily interpretable image, the contrast of which is mainly determined by the sample surface morphology.

In the present work, we mostly used a FESEM (JSM 7001F, JEOL) with a typical acceleration voltage of 5 to 15 kV and at a background pressure of less than 9×10^{-5} Pa to observe the surface as well as cross-sectional morphology of the films.

More information on the working principles of SEM and its versatile applications in materials science can be found in Refs [20] and [21].

4.2.3 Atomic force microscopy

A typical atomic force microscopy (AFM) system consists of a micro-machined cantilever probe with a sharp tip mounted on a piezoelectric (PZT) actuator and a position sensitive photo detector for receiving a laser beam reflected off the end point of the beam to provide cantilever deflection feedback loop.

An AFM can be used to determine the roughness, grain size, and other features on the nanoscale. It can resolve individual holes, defects (such as pinholes), and atomic clusters on the sample surface. In the course of this study, AFM was performed on an AIST-NT SmartSPM, operating in non-contact mode.

For a detailed review of AFM technology see for example Refs. [22] and [23].

4.3 Optical characterization

4.3.1 Optical transmittance

The transmission spectroscopy is a popular method for determining the thickness of thin films with thicknesses larger than 250 nm, and the optical band-gap of the films. In this case, the thickness of the films can be estimated using the interference pattern in the highly transparent spectral region. The detailed method of deriving the thickness is described in Ref. [24]. If the films are thinner than 150 nm, the thickness was estimated using XRR. Sometimes a destructive approach of cleaving the sample and examining its cross section by SEM was used to directly determine the thickness of the films.

In general the intensity I_0 of light impinging onto the sample can be divided into a reflected part I_R, an absorbed part I_A and a transmitted part I_T. Assuming that the reflected light is negligible, the absorption coefficient α of the films is evaluated with the expression

$$T = \frac{I_T}{I_0} = \exp(-\alpha \cdot t). \tag{4.13}$$

Here T is the transmission coefficient and t is the film thickness.

In the case of SnO_2, the energy dependent absorption coefficient $\alpha(hv)$ in the vicinity of the band gap can be expressed as discussion in section 2.2 as equation (2.2). By extrapolating along the linear portion of the $\alpha^{2/3}$ versus hv curve to the hv axis, the optical bandgaps of the films, represented by the intercept at the hv axis, were deduced.

The optical transmittance of the films was measured by a Lambda 900 UV-Vis-NIR spectrometer by Perkin Elmer at room temperature in the wavelength range of 200 - 3000 nm. This apparatus is equipped with two light sources, a deuterium lamp for UV and a halogen lamp for Vis and NIR, which cover the wavelength range of the spectrometer from 180 to 3300 nm.

The reader interested in more details of optical transmittance is referred to Ref. [25].

4.3.2 Photoluminescence spectroscopy

When a semiconductor is excited with light having energy higher than the material's band gap, free electrons and holes can be created. When these electrons and holes recombine, light can be emitted (radiative recombination). This spontaneous emission of light from the material under optical excitation is called photoluminescence (PL). PL spectroscopy is a powerful technique commonly used to elucidate the band structure and the defect characteristics of wide-band gap oxides. In particular, its nondestructive nature and

minimal processing make it attractive for an initial screening of the material quality excitations such as free or bound excitons. Time-resolved photoluminescence (TRPL) yields additional information regarding the underlying relaxation and recombination mechanisms as well as device performance. In particular, the efficiency of the radiative recombination is strongly related to decay time of the respective transition. For more details about the theory of optical recombination in semiconductors see Refs. [26] and [27].

In this work, TRPL and continuous wave PL (CWPL) measurements were carried out on the SnO_2 films which were grown at high temperatures at Philipps-University Marburg. The TRPL measurements were performed using a pulsed titanium-sapphire (Ti:Sa) laser emitting 100 fs pulses at 828 nm and a repetition rate of 78 MHIts frequency tripled fundamental at 276 nm (4.5 eV) is used for excitation. The sample is mounted inside a high-stability flow cryostat with cylindrical heat exchanger to minimize thermal drifts. The measurements discussed in this section are performed at 67 K as the exciton structure disappears above 77 K according to Nagasawa *et al*. [28]. The emission is collected in backscattering geometry in a confocal setup using a reflective microscopy objective to minimize chromatic and hence temporal aberrations. The signal is then imaged onto the entrance slit of a 30 cm Czerny-Turner spectrograph equipped with a synchronously scanning streak-camera featuring a time-resolution of about 1 ps. Additionally, the setup features a back-illuminated deep-cooled CCD camera mounted on a second exit port of the spectrometer for sensitive detection of time-integrated spectra.

More details of the TRPL and CWPL setup can be found in Ref. [29].

4.4 Hall-effect measurements

In this study, the Van der Pauw technique was used to determine the electrical resistivity of the SnO_2 films. Plated silver or pre-sputtered molybdenum were used for contacts. Typically the carrier concentration, resistivity, and Hall mobility at room temperature were measured to evaluate the electrical properties of the films.

The Hall measurements were performed at IPI, University Giessen. Detailed measuring procedures and more basic knowledge about the Hall measurements can be found in Ref. [30].

References

[1] M.E. White, M.Y. Tsai, F. Wu, J.S. Speck, *Plasma-assisted molecular beam epitaxy and characterization of SnO_2 (101) on r-plane sapphire*, J. Vac. Sci. Technol. A, 26 (2008), 1300-1307.

[2] H. Heinke, V. Kirchner, H. Selke, R. Chierchia, R. Ebel, S. Einfeldt, D. Hommel, *X-ray scattering from GaN epitaxial layers - an example of highly anisotropic coherence*, Journal of Physics D: Applied Physics, 34 (2001), A25.

[3] B.E. Warren, *X-ray Diffraction*, Addison-Wesley, (1969).

[4] G. Bauer, W. Richter, *Optical Characterization of Epitaxial Semiconductor Layers*, Springer, Berlin Heidelberg, (1996).

[5] B.D. Cullity, *Elements of X-Ray Diffraction*, Addison-Wesley Publishing company, Inc., the United States of America, (1956).

[6] Y. He, *$CuInS_2$ Thin films for Photovoltaic: RF Reactive Sputter Deposition and Characterization*, PhD thesis, I. Physikalisches Institut, Justus-Liebig-Univeristät Giessen, (2003).

[7] Brüker AXS GmbH, DIFFRAC^{plus}, *REFSIM Version 2.0*.

[8] D.K.G. de Boer, A.J.G. Leenaers, W.W. van den Hoogenhof, *Glancing-incidence x-ray analysis of thin-layered materials: A review*, X-Ray Spectrometry, 24 (1995), 91-102.

[9] A.J.G. Leenaers, J.J.A.M. Vrakking, D.K.G. de Boer, *Glancing incidence X-ray analysis: more than just reflectivity*, Spectrochimica Acta Part B: Atomic Spectroscopy, 52 (1997), 805-812.

[10] K.N. Stoev, K. Sakurai, *Review on grazing incidence X-ray spectrometry and reflectometry*, Spectrochimica Acta Part B: Atomic Spectroscopy, 54 (1999), 41-82.

[11] R.S. Katiyar, P. Dawson, M.M. Hargreave, G.R. Wilkinson, *Dynamics of the rutile structure III. Lattice dynamics, infrared and Raman spectra of SnO_2*, Journal of Physics C: Solid State Physics, 4 (1971), 2421.

[12] P.S. Peercy, B. Morosin, *Pressure and Temperature Dependences of the Raman-Active Phonons in SnO_2*, Physical Review B, 7 (1973), 2779-2786.

[13] T. Lan, C.W. Li, B. Fultz, *Phonon anharmonicity of rutile SnO_2 studied by Raman spectrometry and first principles calculations of the kinematics of phonon-phonon interactions*, Physical Review B, 86 (2012), 134302.

[14] R. Loudon, *The Raman effect in crystals*, Adv. Phys., 13 (1964), 423-482.

[15] T. Livneh, Y. Lilach, I. Popov, A. Kolmakov, M. Moskovits, *Polarized Raman Scattering from a Single, Segmented SnO_2 Wire*, The Journal of Physical Chemistry C, 115 (2011), 17270-17277.

[16] H. Kuzmany, *Solid-State Spectroscopy*, second ed., Heidelberg, Dordrecht, London, New York, (2009).

[17] T. Sander, *Monitoring defect-induced perturbations of the ideal crystal structure of ZnO and Cu_2O by Raman spectroscopy*, PhD thesis, I. Physiakalisches Institut, Justus-Liebig-Univeristät Giessen, (2015).

[18] B. Kramm, *Photoelectrische Charakterisierung der Heterostruktur Kupferoxid-Zinkoxid*, Diplomarbeit, Justus-Liebig-Univeristät Giessen, (2011).

[19] H. Ibach, J.D. Carette, *Electron spectroscopy for surface analysis*, Springer, Berlin, Heidelberg, New York, (1977).

[20] P. Echlin, *Handbook of Sample Preparation for Scanning Electron Microscopy and X-Ray Microanalysis*, Springer, Cambridge Analytical Microscopy, UK, (2009).

[21] D.E. Newbury, D.C. Joy, P. Echlin, C.E. Fiori, J.I. Goldstein, *Advanced Scanning Electron Microscopy and X-Ray Microanalysis*, New York, (1986).

[22] N. Jalili, K. Laxminarayana, *A review of atomic force microscopy imaging systems: application to molecular metrology and biological sciences*, Mechatronics, 14 (2004), 907-945.
[23] P. Eaton, P. West, *Atomic Force Microscopy*, Oxford, (2010).
[24] M.K. Dietrich, *Sputterdeposition von H- und Ga-dotiertem ZnO*, Diplomarbeit, Justus-Liebig-Univeristät Giessen, (2009).
[25] C.F. Klingshirn, *Semiconductor Optics*, Springer, Berlin, Heidelberg, New York, (2007).
[26] P.K. Basu, *Theory of Optical Processes in Semiconductors: Bulk and Microstructures*, Clarendon Press, Oxford, (1997).
[27] T.H. Gfroerer, *Photoluminescence in Analysis of Surfaces and Interfaces*, John Wiley & Sons Ltd, Chichester, (2000), pp. 9209-9231.
[28] M. Nagasawa, S. Shionoya, *Urbach's rule exhibited in SnO_2*, Solid State Commun., 7 (1969), 1731-1733.
[29] A.A. Chernikov, *Time-Resolved Photoluminescence Spectroscopy of Semiconductors for Optical Applications beyond the Visible Spectral Range*, PhD thesis, the faculty of physics, Philipps-Universität, Marburg, (2011).
[30] D. Meister, *Elekrische und optische Charakterisierung von Galliumnitrid*, PhD thesis, I. Physikalisches Insitut, Justus-Liebig-Univeristät Giessen, (2001).

5 SnO_2 films on quartz glass

Quartz glass as a substrate material has many advantageous characteristics. This is reflected by the versatile applications. Applications of quartz glass include photomask substrates in the semiconductor industry, TFT substrates for LCDs, micro lens substrates for LCDs etc. SnO_2 as gas sensor is also often deposited on glass. Non-crystalline quartz glass is inexpensive compared to the single crystal substrates. It possesses high stability over a wide temperature range, high stability against a variety of solvents, high transmissivity over a wide range of wavelengths from UV to IR, and low dielectric loss even at GHz frequencies.

5.1 Influence of the substrate temperature on growth rate

A series of SnO_2 thin films was grown by CVD on quartz glass in this work. The relationship between the growth rate of SnO_2 films and the substrate temperature is shown in Fig. 5.1. All the films discussed in this subsection 5.1 were grown under similar conditions (oxygen gas flow of 20 sccm and SnI_2 evaporation rate of about 0.02 g/h), but different substrate temperatures and different deposition times. As can be seen in Fig. 5.1, the growth rate increases almost linearly from 24 nm/h at 450 °C to 243 nm/h at 650 °C. However, the growth rate decreases to 207 nm/h at 700 °C. This decrease in deposition rate at the highest temperature may be attributed to a depletion of the amount of tin-containing species reaching the reaction zone. When the substrate temperature was lower than 350 °C, no SnO_2 films could be obtained. In other words, the reaction $SnI_2 + O_2 \rightarrow SnO_2 + I_2$ was suppressed at temperatures below 350 °C.

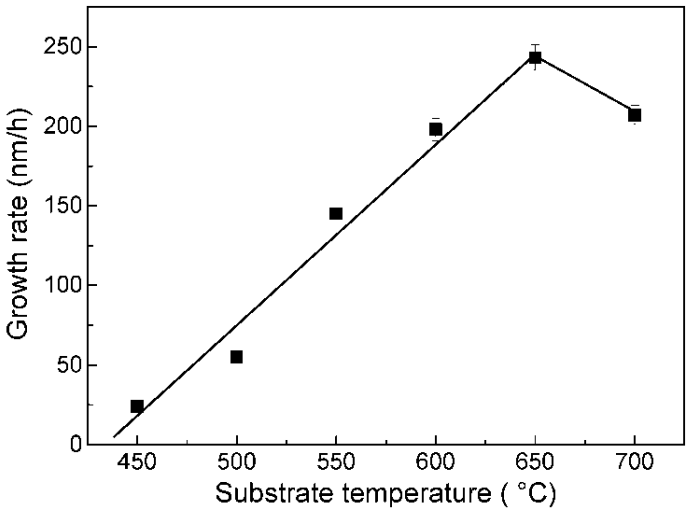

Fig. 5.1. Dependence of the growth rate on the substrate temperature. (The length of the uncertainty bars of some thin films are close to the symbol size.)

In fact, in addition to the substrate temperature, there are many experimental factors which may affect the growth rate of SnO_2 films as mentioned before. The dependence of the growth rate on the oxygen gas flow is discussed in detail in the chapter 6.

It should be noted that our initial idea was to obtain SnO_2 or SnO by adjusting the deposition parameters. However, when the temperature decreases, the growth rate decreases. When the oxygen gas flow is low, the reaction to form SnO_2 is slow, but no SnO could be observed in this study. This finding is explained by considering the Gibbs free energy of formation which is calculated for different experimental conditions in the chapter 3 (see Fig. 3.3). The formation energy of SnO_2 is clearly lower than that of SnO, so all films produced in this study show a pure SnO_2 phase without any SnO precipitates. Using another O-precursor which reacts via a ligand-exchange mechanism instead of involving oxidation reactions or applying a non-equilibrium growth technique might offer pathways to grow SnO. Actually, typical non-equilibrium physical vapor deposition techniques such as sputtering and PLD have already been used to prepare SnO films successfully [1-3].

In our experiments, SnO_2 films with a relatively high quality at a sufficient growth rate, are obtained at a substrate temperature between 500 and 700 °C while keeping the SnI_2 evaporation rate of 0.2 g/h. Almost all deposited films are colorless and transparent, while only films thicker than 1.5 µm show a whitish milky appearance caused by light scattering from the rough surface.

5.2 Structure and morphology by XRD and SEM

XRD measurements reveal that all films obtained in this work consist of pure rutile SnO_2 without any secondary phases such as SnO and Sn_3O_4. In Fig. 5.2, θ-2θ scans of two typical samples are presented, together with the standard powder diffraction pattern of SnO_2 for comparison. The film in Fig. 5.2(a) was deposited at a substrate temperature of 650 °C for 2 h with a thickness of 410 nm. As can be seen, all diffraction peaks of the film can be identified as reflections from crystal planes of SnO_2 with a tetragonal rutile structure, and the (110) and (101) reflections are dominant in this θ-2θ scan, well according to the standard diffraction data of SnO_2 powder. This observation is somewhat expected as the (110) plane represents the lowest energy face in a SnO_2 single crystal [4]. As reported in Ref. [4], the {110} faces make up the largest fraction of the surface area followed by the {101} faces and small {100} faces in single-crystalline SnO_2.

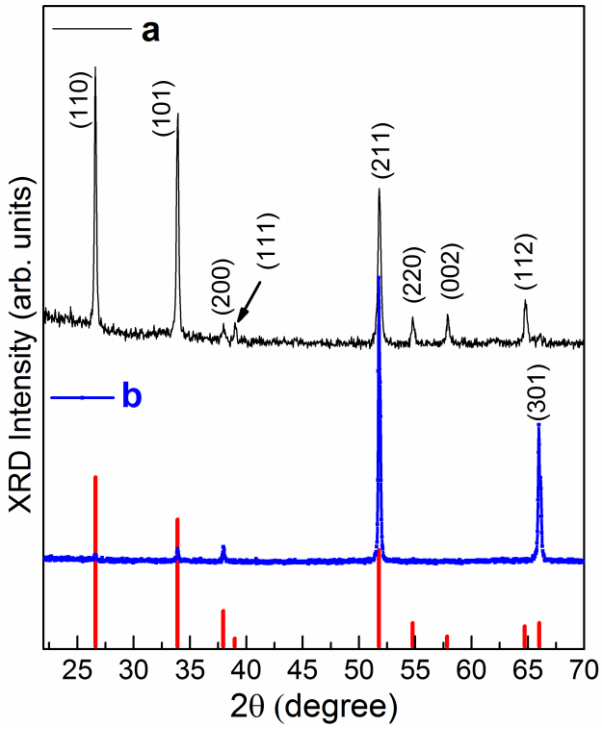

Fig. 5.2. XRD spectra of SnO_2 films deposited at a substrate temperature of 650 °C for (a) 2 h with a thickness of 410 nm, and (b) 6.5 h with a thickness of 1780 nm. The red lines correspond to the standard powder diffraction trace of SnO_2 (International Centre for Diffraction Data (ICDD) Powder Diffraction File (PDF) No. 41-1445).

For films thicker than 1 µm, the θ-2θ scan changed significantly. As shown in Fig. 5.2(b), the film deposited for 6.5 h with a thickness of 1780 nm exhibits the strongest reflection from (211) instead of (110), indicating a (211) preferred orientation of the film.

In this work, we found that the film thickness actually played a key role in the orientation of the resulting films. At the beginning of growth the film surface prefers to assume the lowest energy face of (110). As the growth continues, the crystallite size increases. When the film thickness exceeds a critical value, the (110) orientation is no longer preferred, but rather other orientations of (211) and (301) become more pronounced, as revealed by XRD. The work of Viirola *et al.* demonstrated in detail a similar orientation evolution of SnO_2 films on glass from (110)- to (211)-dominated upon increasing of the film thickness [5].

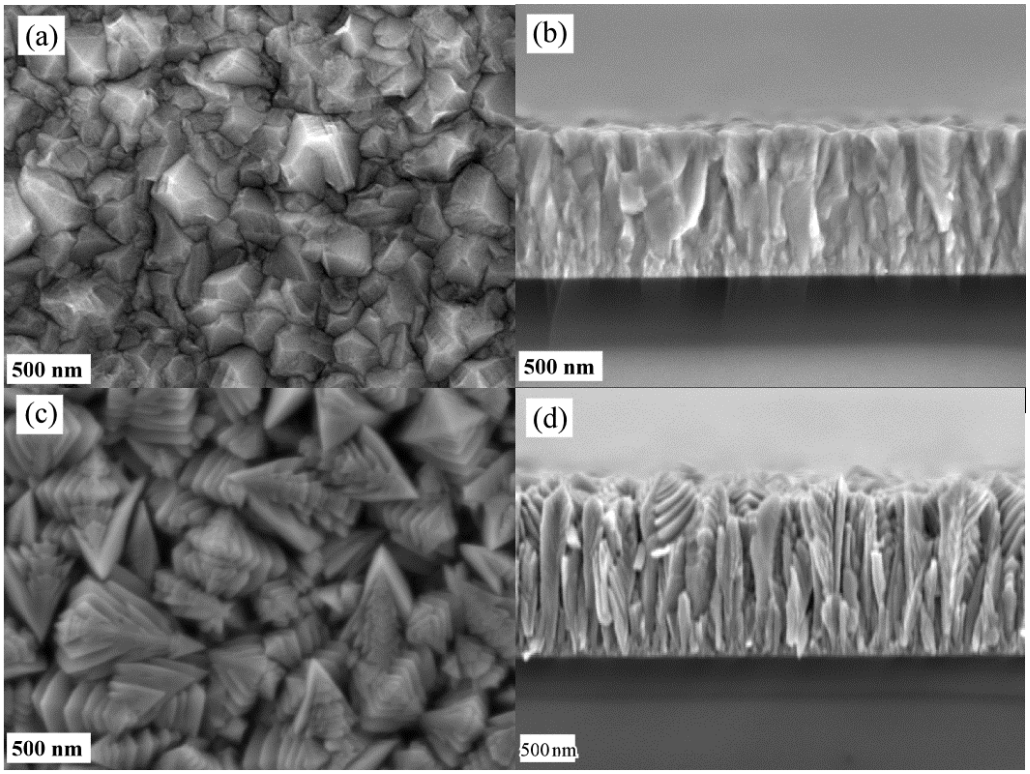

Fig. 5.3. Typical SEM images for SnO_2 thin films deposited for 3 h with a thickness of 870 nm (a, b), and for 6.5 h with a thickness of 1780 nm (c, d).

Fig. 5.3 shows the plane-view (a, c) and cross-sectional (b, d) SEM images of two samples, demonstrating the typical surface morphology and microstructure of SnO_2 films deposited on quartz glass. The top sample (corresponding to Fig. 5.3a, b) was grown at a substrate temperature of 550 °C for 3 h to a thickness of 870 nm. The grains have grain sizes in the range of 100 - 500 nm. The bottom sample (corresponding to Fig. 5.3c, d) was deposited at a substrate temperature of 650 °C for 6.5 h yielding a thickness of 1780 nm. It can be seen that most grains in the second sample have an arrow-like shape with a length over 500 nm (see in Fig. 5.3c). The arrow-shaped grains formed additional facets on the surface yielding a subtle grain structure. The ‘cracks’ in the grains are most likely a result of twinning, i.e., formation of stacking faults in the crystal lattice of the grains. Both cross-

sectional images show columnar grains of SnO_2 grown directly on the quartz glass substrates. The grains at the bottom were well compacted in both samples. However, the grains at the top become bigger and there are gaps between grains in Fig. 5.3d. These significant changes in grain shape and grain size could be attributed to the enhanced atomic diffusion and migration during the prolonged deposition at elevated temperature, in which crystalline grains grow along low stress directions, resulting in a faceted surface with larger roughness [6]. After comparing and analyzing about 30 samples, we find that the morphology of the SnO_2 films is strongly influenced by the film thickness and the growth temperature. The films thinner than 1 µm have smaller grain sizes and show a uniform and smooth surface and a dense structure. When the films become thicker, the grain sizes increase and the three-dimensional growth of the rutile SnO_2 grains lead to a rough surface and a loose structure of the films.

5.3 Optical properties

Fig. 5.4 shows the optical transmittance spectra of SnO_2 films of different thicknesses on quartz glass as a function of the incident light wavelength in the range from 200 to 2600 nm. The average transmittance in the visible range for all SnO_2 samples is over 80%, while it was about 93% for the quartz glass substrate. The absolute average transmittance (i.e. corrected for the substrate contribution) of the SnO_2 films is about 90%. The inset in Fig. 5.4 shows that the optical transmission edge of SnO_2 films shifts towards longer wavelengths with increasing film thickness. At a first glance, this thickness-dependent variation seems to be consistent with the general observation for very thin films that the optical absorption edge shifts towards higher energies/shorter wavelengths with decreasing thickness due to quantum size effects. However, as presented below (cf. Fig. 5.5) the absorption edge of the SnO_2 films determined from Tauc plots actually does not confirm this hypothesis. Thicknesses above 200 nm are too large to lead to quantum size effects. Possible reasons for the variation of the transmission with thickness in Fig. 5.4 need to be sought in the different orientations of the films, the morphology, the neglect of changes of the reflection, and the steep slope of the absorption as a function of energy close to the band gap.

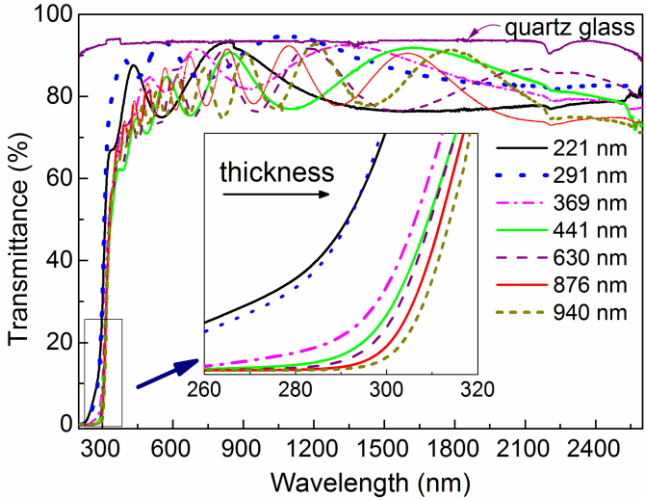

Fig. 5.4. Optical transmittance spectra of SnO_2 thin films with different thicknesses.

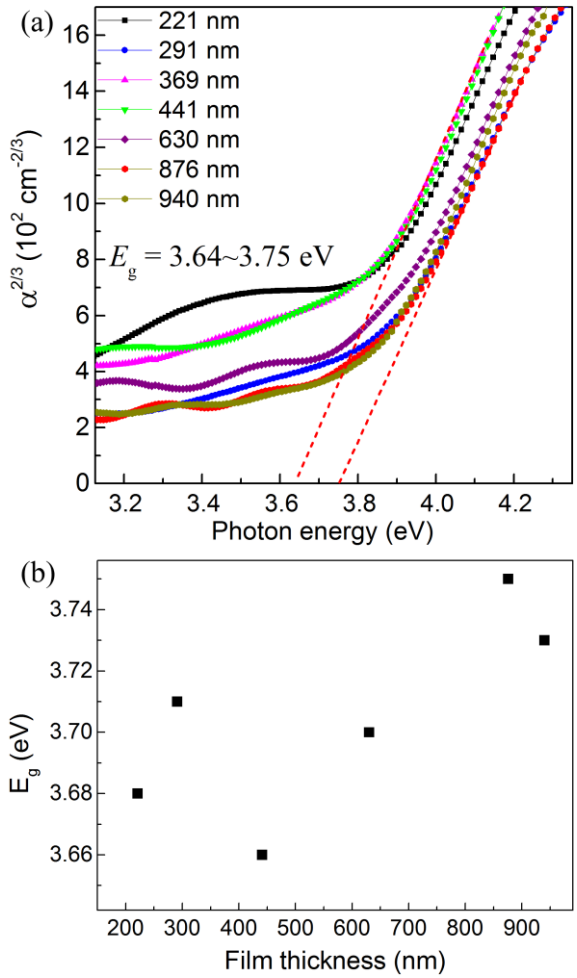

Fig. 5.5. (a) Plots of $\alpha^{2/3}$ as a function of photon energy ($h\nu$) for SnO_2 thin films of different thickness, (b) extracted band gaps E_g versus film thickness of the SnO_2 films on quartz glass.

For a direct forbidden transition, the energy-dependent absorption coefficient $\alpha(h\nu)$ can be expressed by the relation given by equation (2.2). The plots of $\alpha^{2/3}$ as a function of photon energy $h\nu$ for films with different thicknesses are shown in Fig. 5.5a. Extrapolating the linear portions of $\alpha^{2/3}$ - $h\nu$ plots to zero absorption yielded band-edge values between 3.64 and 3.75 eV for the SnO_2 films (see Fig. 5.5b). It was well documented in literature that SnO_2 single crystals show anisotropic absorption edges of 3.93 and 3.57 eV for radiation polarized parallel and perpendicular to the *c* axis of the crystal, respectively [7, 8]. As SnO_2 films produced in this study are polycrystalline showing no *c* axis preferential orientation, they exhibit optical absorption edges within the anisotropic absorption edges of SnO_2 single crystals. In a recent theoretical report, Schleife *et al.* [9] explained the difference in the experimentally observed gaps for *E* perpendicular and parallel to *c* as a result of the anisotropy in the dipole-allowed direct transitions from lower lying valence bands rather than due to the bands at the valence band maximum. In this study we could not use polarized light to identify the anisotropic absorption edges of particular films. Therefore, the films exhibit absorption edges in between the anisotropic absorption edges of SnO_2 single crystal, and no clear trends with thickness are observed in Fig. 5.5(b).

5.4 Conclusions

Polycrystalline SnO_2 thin films were fabricated on quartz glass substrates using CVD. X-ray diffraction shows that pure-phase SnO_2 films were formed and precipitates of other Sn_xO_y phases (such as SnO and Sn_3O_4) did not occur. Detailed analysis using XRD and SEM techniques reveals that the microstructures in terms of grain orientation, size and shape, depended on the thickness of the films. The (110) reflection is the most intense in films of thickness up to about 400 ~ 500 nm, but for thicker films the (211) reflection becomes dominant. The optical absorption edges of the films are in the range from 3.64 to 3.75 eV, which is independent of the film thickness, when the films are thicker than 200 nm.

References

[1] Y. Ogo, H. Hiramatsu, K. Nomura, H. Yanagi, T. Kamiya, M. Hirano, H. Hosono, *p-channel thin-film transistor using p-type oxide semiconductor, SnO,* Appl. Phys. Lett., 93 (2008) 032113.

[2] J. Um, B.-M. Roh, S. Kim, S. Eunkyung Kim, *Effect of radio frequency power on the properties of p-type SnO deposited via sputtering*, Materials Science in Semiconductor Processing, 16 (2013) 1679-1683.
[3] P.-C. Hsu, C.-J. Hsu, C.-H. Chang, S.-P. Tsai, W.-C. Chen, H.-H. Hsieh, C.-C. Wu, *Sputtering Deposition of P-Type SnO Films with SnO_2 Target in Hydrogen-Containing Atmosphere*, ACS Applied Materials & Interfaces, 6 (2014) 13724-13729.
[4] M. Batzill, U. Diebold, *The surface and materials science of tin oxide*, Progress in Surface Science, 79 (2005) 47-154.
[5] H. Viirola, L. Niinistö, *Controlled growth of tin dioxide thin films by atomic layer epitaxy*, Thin Solid Films, 249 (1994) 144-149.
[6] L.Y. Liang, Z.M. Liu, H.T. Cao, X.Q. Pan, *Microstructural, Optical, and Electrical Properties of SnO Thin Films Prepared on Quartz via a Two-Step Method*, ACS Applied Materials & Interfaces, 2 (2010) 1060-1065.
[7] R. Summitt, J.A. Marley, N.F. Borrelli, *The ultraviolet absorption edge of stannic oxide (SnO_2)*, Journal of Physics and Chemistry of Solids, 25 (1964) 1465-1469.
[8] M. Nagasawa, S. Shionoya, *Temperature Dependence of the Fundamental Optical Absorption Edge in Stannic Oxide*, J. Phys. Soc. Jpn., 30 (1971) 1118-1123.
[9] A. Schleife, J.B. Varley, F. Fuchs, C. Rödl, F. Bechstedt, P. Rinke, A. Janotti, C.G. Van de Walle, *Tin dioxide from first principles: Quasiparticle electronic states and optical properties*, Physical Review B, 83 (2011) 035116.

6 SnO_2 films on *c*-plane sapphire

Despite a fairly large lattice mismatch between SnO_2 and sapphire (single crystal of Al_2O_3), sapphire has several advantages as a substrate material: it is stable at high temperatures, optically transparent, and it is cheap compared to other crystalline substrates. Sapphire has many unique features such as high strength, high anti-corrosion, high anti-abrasion, low dielectric loss, good electrical insulation, with excellent mechanical and chemical characteristics. Therefore sapphire wafers are used extensively as a substrate for many epitaxial films and play an important role in the photo-electronics industry today. In this chapter we report on the epitaxial growth of SnO_2 films on *c*-sapphire using chemical vapor deposition (CVD). First, the influence of the oxygen flow rate on properties of SnO_2 thin films is discussed. Then, the growth mechanism of SnO_2 grown on *c*-plane sapphire is investigated.

6.1 Characterization of the quality of single crystal substrates

For the manufacturer of substrates, it is almost impossible to prepare a completely ideal cut, when cutting a large bulk crystal into substrates of defined orientation. The error in the surface orientation when cutting is referred to as miscut. The miscut is defined with respect to the crystal structure of the surface, and can be characterized by two angles: a polar angle θ and an azimuthal angle ϕ (in Fig. 6.1) [1]. In this work we present a simple way using XRD ω-scans to estimate the miscut polar angle θ of single crystal substrates.

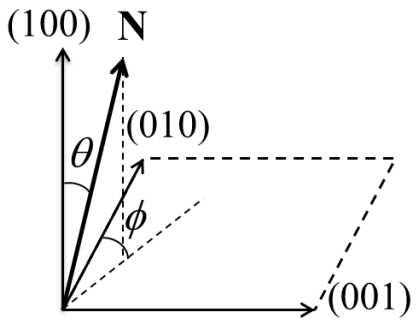

Fig. 6.1. A sketch of the miscut polar angle θ and in-plane angle ϕ.

The XRD measurements presented in this subsection were performed on a Siemens D5000 system, according to the following procedure.

To determine the miscut of *c*-sapphire substrates, we first measured θ-2θ scan to find the Al_2O_3 (0006) reflection. If we use slits of 0.1/0.1/0.005 mm and an increment of 0.002°, the reflections of Al_2O_3 (0001) can be separated into two reflections, which are caused by the Cu $K_{\alpha 1}$ (λ=1.54060 Å) and Cu $K_{\alpha 2}$ (λ=1.54443 Å) of the radiation source used (in Fig. 6.2). The (0006) peak of *c*-sapphire from Cu $K_{\alpha 1}$ locates at 41.675°.

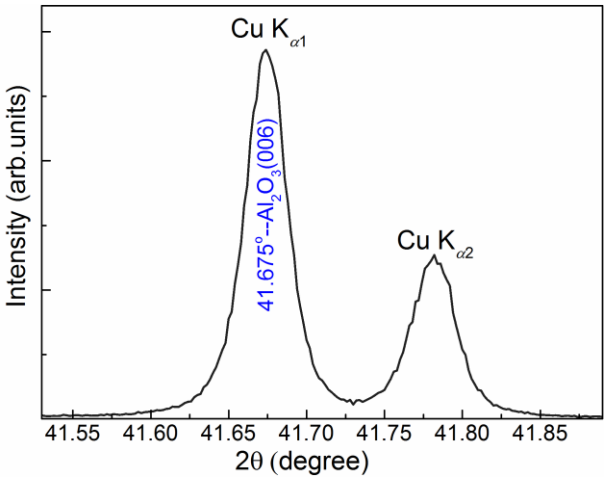

Fig. 6.2. XRD θ-2θ scan of a *c*-sapphire substrate.

Then, we focused on the (0006) reflex of the Al_2O_3 substrate caused by the Cu $K_{\alpha 1}$ radiation (the left peak in Fig. 6.2) and performed a rocking curve measurement of this reflection. The sample holder was adjusted using the 'Justierung Theta-Scan' function in the program 'Immediate Measurement'. We compared the adjusted position (angle) of sample holder (plate) with the initial position (angle) of it. This change of the angle was recorded. Then the substrate was rotated by steps of 45° along its surface axis. The corrected angle was measured again. The maximum angular difference between the adjusted sample holder position and the initial position is the polar angle θ. The corrected angle of the sample holder with the rotation angle of the substrate is depicted in Fig. 6.3(b). When the corrected angle of the plate is located at the maximum, the substrate is lying on the sample holder as shown in Fig. 6.4(a). After the substrate is rotated by 180°, the substrate is positioned on the sample holder as depicted in Fig. 6.4(b). The corrected angle of the plate between maximum and minimum is about 0.046° (= 0.051° - 0.005°) (Fig. 6.3b). Thus, the miscut polar angle θ for this *c*-sapphire substrate is about 0.023° ($\theta = \frac{\theta_{max}-\theta_{min}}{2}$ = (0.051°-0.005°)/2).

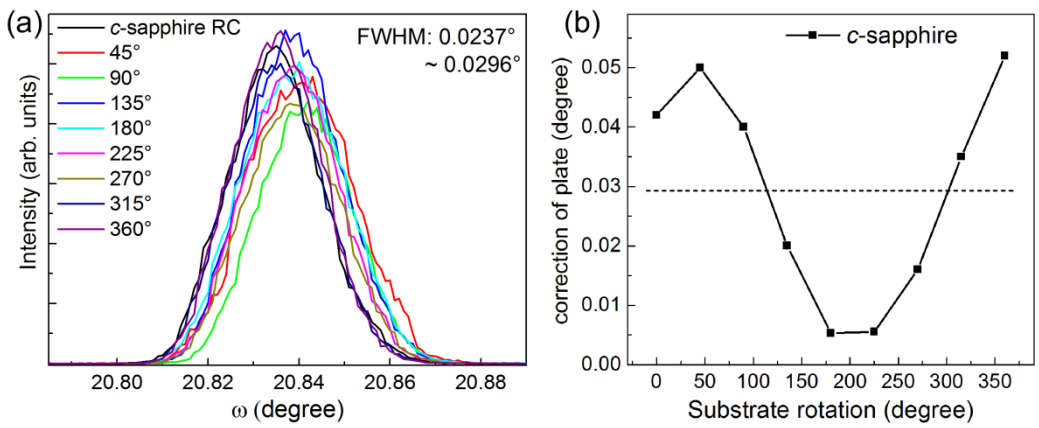

Fig. 6.3. (a) XRD rocking curves of Al_2O_3 (0006) reflections (the substrate is rotated by steps of 45° along the surface axis between measurements). (b) Corrected angle of the sample holder as a function of the substrate rotation angle.

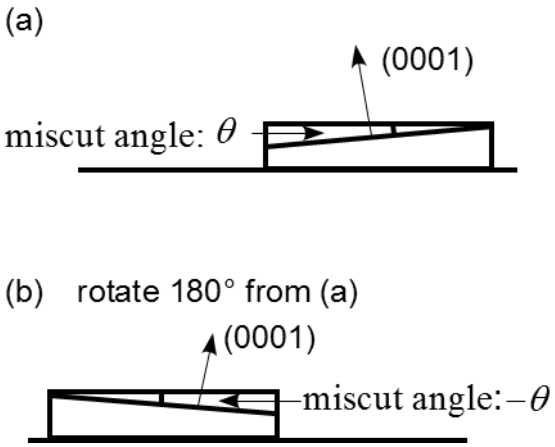

Fig. 6.4. a schematic diagram of the determination of the miscut polar angle by XRD measurement.

Fig. 6.4 shows a schematic diagram of the determination of the miscut polar angle of the cross-section for *c*-plane sapphire by XRD measurement.

6.2 Influence of oxygen flow rate on the properties of SnO_2 thin films

The partial pressure of the precursor used is an important parameter, which can obviously influence the quality of the deposited films in the CVD process. In this section we will discuss the influence of the oxygen flow rate used in the growth process on the properties of SnO_2 thin films on *c*-sapphire.

Before this subject is discussed, the structural similarities between *c*-sapphire and SnO_2 (100) are discussed. While sapphire has a rhombohedral structure, SnO_2 crystallizes in a tetragonal lattice. However, the epitaxial growth of SnO_2 (100) on Al_2O_3 (0001) may be possible due to the similarity of the octahedral oxygen sublattice of SnO_2 (100) and Al_2O_3 (0001) [2] as presented in Fig. 6.5. Diagrams (a) and (b) display the geometrical configurations of the Al_2O_3 (0001)- and the SnO_2 (100)-plane, respectively, with the rhombohedral structure of sapphire resembling a hexagonal lattice [3]. In this respect, the sapphire (0001) surface can be described by three equivalent rectangular unit cells rotated by 120° with respect to each other. SnO_2 (100) also possesses a rectangular unit cell. The latter matches either one of the three unit cells of the sapphire surface indicated in Fig. 6.5(a), thus favoring the formation of three distinct domain orientations. The lattice mismatch between Al_2O_3 <1$\bar{2}$10> (4.759 Å) and SnO_2 <0$\bar{1}$0> (4.738 Å) is only 0.4%, while it is about 16.0% for Al_2O_3 <$\bar{1}$010> (2.747 Å, the projection distance in the plane) and SnO_2 <001> (3.187 Å) [4]. Nevertheless, the mismatch between domains of six unit cells of SnO_2 in <001>-direction and seven unit cells of Al_2O_3 in <$\bar{1}$010>-direction is only 0.56%.

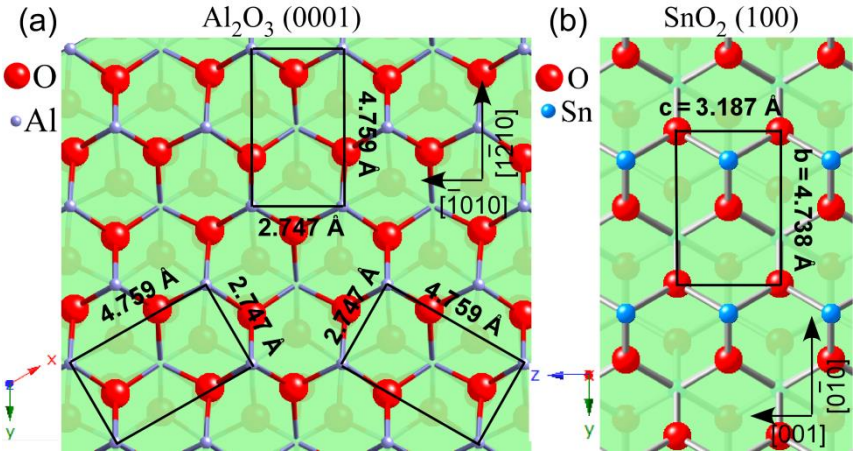

Fig. 6.5. Schematic diagrams of (a) Al_2O_3 (0001)-plane and (b) SnO_2 (100)-plane. The lattice constant of 2.747 Å along <$\bar{1}$010> direction is the projection of Al_2O_3 unit cell onto the (0001)-plane. All lattice constants are based on the ICDD PDF No. 46-1212 and 41-1445 for Al_2O_3 and SnO_2, respectively.

6.2.1 Influence of the oxygen flow rate on the growth rate

In section 5.1 we have discussed the influence of the substrate temperature on the SnO_2 growth rate. Here the growth rate of SnO_2 films in dependence on the O_2 flow rate is analyzed. A series of samples, which were deposited at a fixed substrate temperature (510 °C) and a constant evaporation rate of SnI_2 (0.016 g/h) while varying the O_2 flow rate in the mini CVD system, are studied. As can be seen in Fig. 6.6, the growth rate increases almost linearly from 40 to 244 nm/h with increasing the O_2 flow rate from 5 to 40 sccm. However, when the O_2 flow rate further increases to 60 sccm, the growth rate reaches only 290 nm/h, instead of ~360 nm/h expected from a linear extrapolation. Similar observations were reported by Ghoshtagore [5], who studied systematically the oxygen partial pressure dependence of the SnO_2 deposition rate while keeping the Sn-precursor $SnCI_4$ partial pressure constant in the CVD process, an initial linear increase followed by a plateau-like behavior was observed. The Sn-precursor with fixed evaporation rate, 0.016 g/h of SnI_2 in our experiments, can react only with a certain maximum amount of O_2 leading to a plateau in the dependence of the growth rate on O_2 flow rate according to Ref. [5]. In our case, the corresponding flow rate is 48 sccm. A further increase of O_2 (over supplied) will not result in an additional increase of the SnO_2 growth rate due to the limited SnI_2 supply.

In the following sections from 6.2.2 to 6.2.7, we will discuss these five samples, which were prepared at the fixed substrate temperature of 510°C, the constant evaporation rate of SnI_2 of 0.016 g/h, but at different oxygen flow rates of 5, 10, 20, 40 and 60 sccm. The samples are labeled as O1, O2, O3, O4 and O5, respectively.

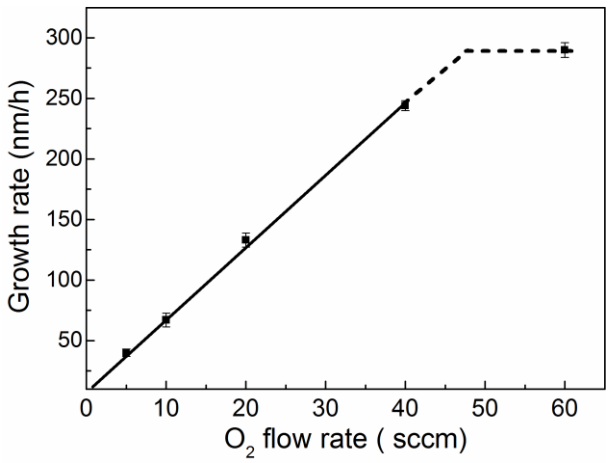

Fig. 6.6. The SnO_2 growth rate as a function of O_2 flow rate in the CVD process using a fixed evaporation rate of the tin-precursor SnI_2.

6.2.2 Structure of SnO_2 thin films on *c*-sapphire

A XRD θ-2θ scan of a typical SnO_2 film is shown in Fig. 6.7. The scan covers a 2θ range from 20° to 85°. In addition to the very sharp (0006) peak of the *c*-sapphire substrate, there are only two additional peaks located at about 38.2° and 81.8°. These peaks can be assigned to the (200) and (400) reflections of rutile SnO_2. Although a logarithmic scale is chosen for the intensity, no signs of other orientations or secondary phases are present in the pattern, indicating that a pure-phase tetragonal rutile SnO_2 film was grown on sapphire with an out-of-plane orientation of $SnO_2(100)\|Al_2O_3(0001)$. It is worth noting that, using CVD we could obtain pure-phase SnO_2 films with a genuine (100) orientation on *c*-sapphire up to film thicknesses of more than 1 µm.

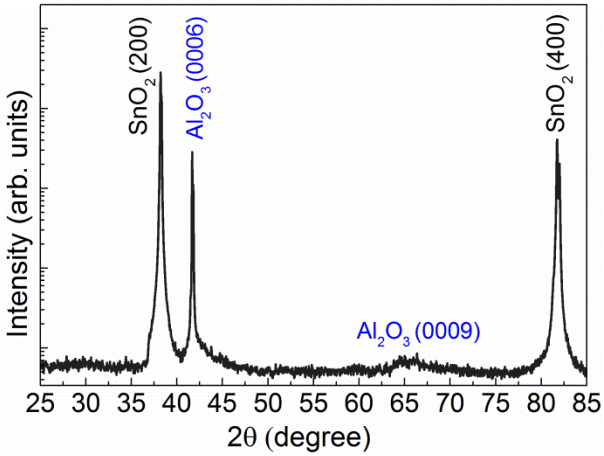

Fig. 6.7. θ-2θ scan of a typical SnO_2 film grown on *c*-sapphire at substrate temperature of 510 °C.

In Fig. 6.8(a), XRD θ-2θ scans of SnO_2 films deposited at different O_2 flow rates are compared. The scan range is restricted to the range between 36° and 45° for highlighting the (200) peak shift. The thickness of the films increases from 161 to 1162 nm with increasing the O_2 flow rate from 5 to 60 sccm. While the SnO_2 (200) peak position of the thinner films (O1 and O2) is close to that of powder SnO_2, the positions of the SnO_2 (200) peaks of thicker films shift gradually to higher angles. For the films (O4 and O5), the 2θ shift of 0.23° corresponds to 0.58% shrinkage of the lattice along the *a*-axis. This means there is a considerable amount of compressive stress present in the thick SnO_2 films while thinner films are almost free of stress along the *a*-axis. It is interesting to note that the (200) peak of the film O4 is narrow enough to reveal the doublet structure originating from Cu$K_{\alpha 1}$ and Cu$K_{\alpha 2}$ radiation of the X-ray source, implying a superior crystalline quality of this film.

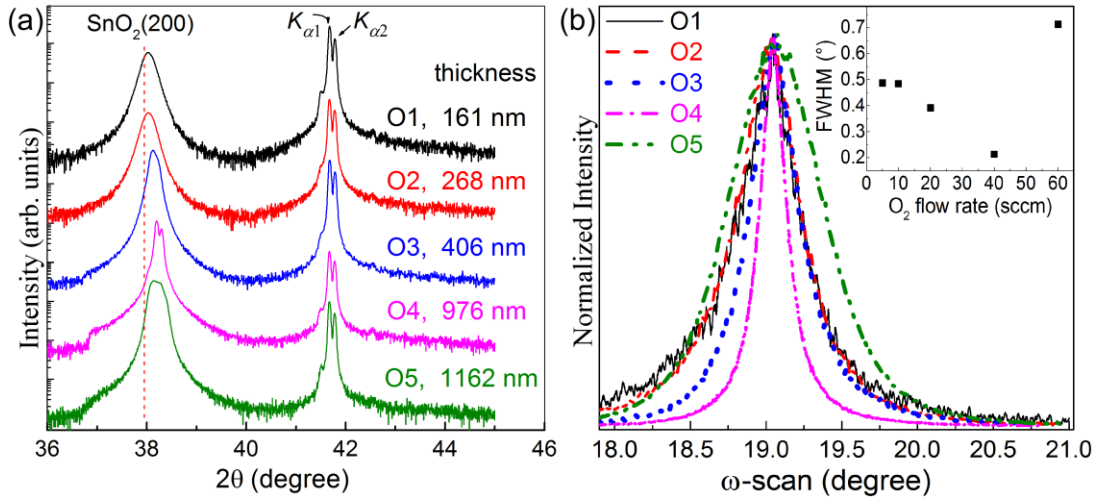

Fig. 6.8. XRD patterns of SnO_2 films deposited on *c*-sapphire at substrate temperature of 510 °C: (a) θ-2θ scan of SnO_2 films deposited at various O_2 flow rates (the film thickness is indicated), and (b) rocking curves at SnO_2 (200)-plane of films deposited at various O_2 flow rates (the inset shows the half width of the rocking curves as a function of the O_2 flow rate).

Fig. 6.8(b) depicts rocking curves of the (200) plane of SnO_2 samples grown at different O_2 flow rates. In the inset of Fig. 6.8(b) the corresponding full width at half maximum (FWHM) values of the rocking curves are shown. The FWHM first decreases with increasing O_2 flow rate, reaches a minimum of 0.21° for the sample O4 grown with 40 sccm O_2, and then increases to 0.71° for the sample O5. This indicates that the out-of-plane ordering of SnO_2 films is enhanced with increasing O_2 flow rate up to 40 sccm and then declines with further increase of the O_2 flow rate. The initial enhancement of the out-of-plane ordering of SnO_2 films might be due to the decrease of the concentration of oxygen vacancies (V_O) with increasing O_2 flow rate. However, the sample O5 grown with 60 sccm O_2 exhibits a significantly degraded out-of-plane ordering compared with the sample O4 that was grown at 40 sccm O_2. This is attributed to the over supplied O_2 which deteriorates the film quality. As discussed above, SnI_2 of 0.016 g/h can react at maximum with 48 sccm O_2 in the mini CVD system. Any O_2 additionally supplied does not contribute to the growth rate; it even deteriorates the film quality. The rocking curve measurements again show that sample O4 grown at 40 sccm O_2 has the best out-of-plane ordering among the five samples, consistent with the θ-2θ scan results.

6.2.3 Surface morphology by SEM

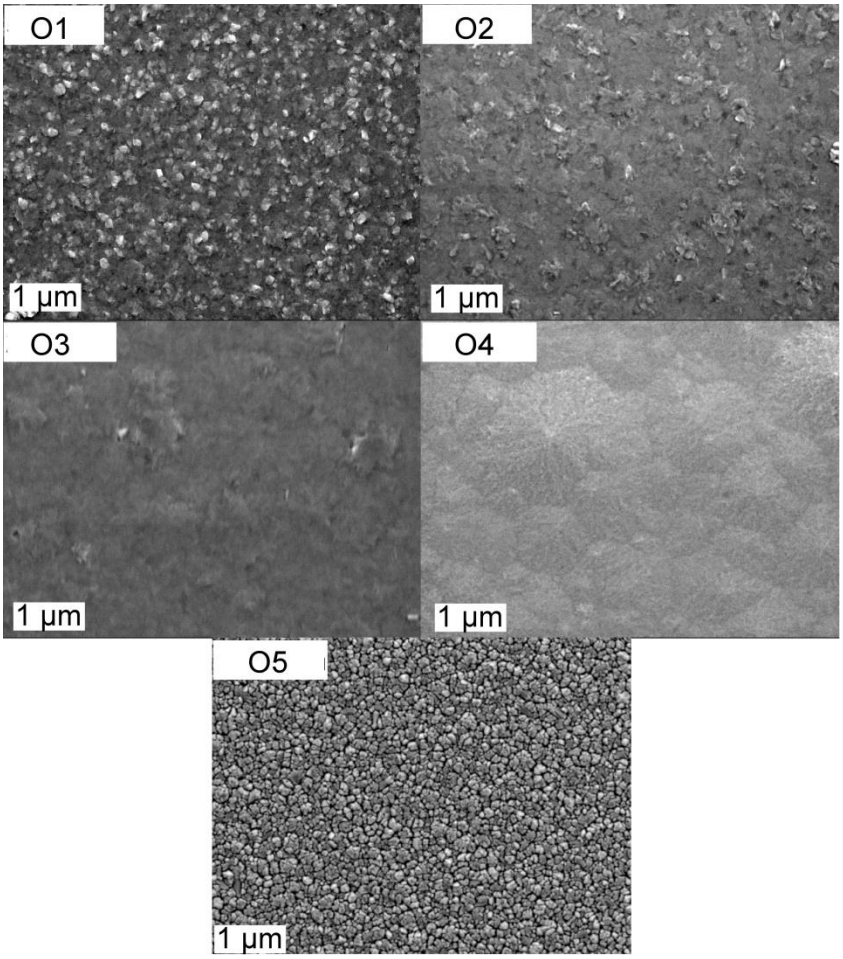

Fig. 6.9. SEM images of the surfaces of SnO_2 thin films deposited at different O_2 flow rates.

Fig. 6.9 shows the SEM images of the surfaces of samples O1 to O5. The surface of sample O1 is rough, showing many small grains (grain size < 80 nm) which are implanted in the flat matrix. For sample O2 the implanted grains are fewer, while for sample O3 there are almost no grains observable. Sample O4 exhibits a very flat surface consisting of crystal domains of µm-sizes (0.5 to 2 µm). Some domains have a hexagonal form reflecting the hexagonal structure of the substrate Al_2O_3 (0001). The hexagonal structure of the domains can be regarded as arising from the three equivalent orientations of the rectangular SnO_2 unit cells on the *c*-sapphire surface. The three equivalent rectangular unit cells are rotated by 120° with respect to each other (see Fig. 6.5). A SnO_2 (100) face could be based on either one of the three unit cells. Therefore the surface of high-quality SnO_2 thin films exposes hexagonal domains. The sample O5 grown at 60 sccm O_2 shows again a rough surface comprising many grains. The improvement of the surface smoothness and

crystallization of the films with increasing O_2 flow rate (from 5 to 40 sccm) indicates a gradual improvement of the overall crystalline quality of SnO_2 films (from O1 to O4), which is in good agreement with the XRD results presented in the previous section.

6.2.4 Composition analysis by XPS

Fig. 6.10(a) presents the full XPS spectra of a typical SnO_2 film recorded before and after cleaning of the surface by sputtering. Because the SnO_2 films had been exposed to ambient air for an extended period of time, the surface layer needed to be removed as it may be contaminated by hydrocarbons etc. To obtain the actual chemical composition of the films, the film surface was sputtered using a high dose of argon ions (ion energy of 1.5 keV) to remove the hydrocarbon contaminations. The C 1s peak that is present in the spectrum of the air-exposed film disappears after sputtering, assuring a sufficient cleaning of the film surface. The full scan reveals that the film is composed of Sn and O without any impurities. The weak peak which shifted by about 10 eV to lower energy with respect to Sn $3d_{5/2}$ is a satellite line from Sn $3d_{5/2}$ due to Al $K_{\alpha 3}$ excitation from the non-monochromated X-ray source of the XPS setup [6].

Fig. 6.10(b) shows core-level spectra of O 1s and Sn 3d for the samples grown at different O_2 flow rates. All the peak positions were corrected with respect to the C 1s peak at 284.6 eV, which was due to contamination of the film surface by air exposure. The Sn $3d_{5/2}$, Sn $3d_{3/2}$ and O 1s peaks of all films are located at 486.5, 494.9 and 530.3 eV, respectively, in good agreement with previous reports of Ansell [7] and Liang *et al.* [8]. Based on these works the chemical state of Sn^{4+} and bonding of O-Sn^{4+} can be unambiguously identified in the films, confirming that our CVD grown films consist of pure-phase SnO_2. The Sn 3d and O 1s peak positions of films grown at different O_2 flow rates hardly vary throughout the series (<0.1 eV), indicating that pure-phase SnO_2 can be obtained in a broad range of O_2 fluxes.

We further used XPS core-level spectra to determine the chemical stoichiometry of the CVD grown films. Fig. 6.10(c) shows the atomic ratio O/Sn of a typical film as a function of sputter-time. Quantification of the composition is carried out based on the O 1s and Sn 3d core-level XPS spectra by using the software CasaXPS. For sputtering of the film Ar^+ ions were gently introduced with an acceleration voltage of 0.5 kV and beam current of 0.7 µA. The quantification results in an atomic ratio of O/Sn close to 2.0 on the film surface, and decreasing O/Sn atomic ratio with increasing sputtering time. It is well known that ion bombardment of SnO_2 leads to preferential sputtering of oxygen [9]. Therefore, a freshly prepared film, where a sputter cleaning of the surface can be omitted, is best suited for a reliable composition examination.

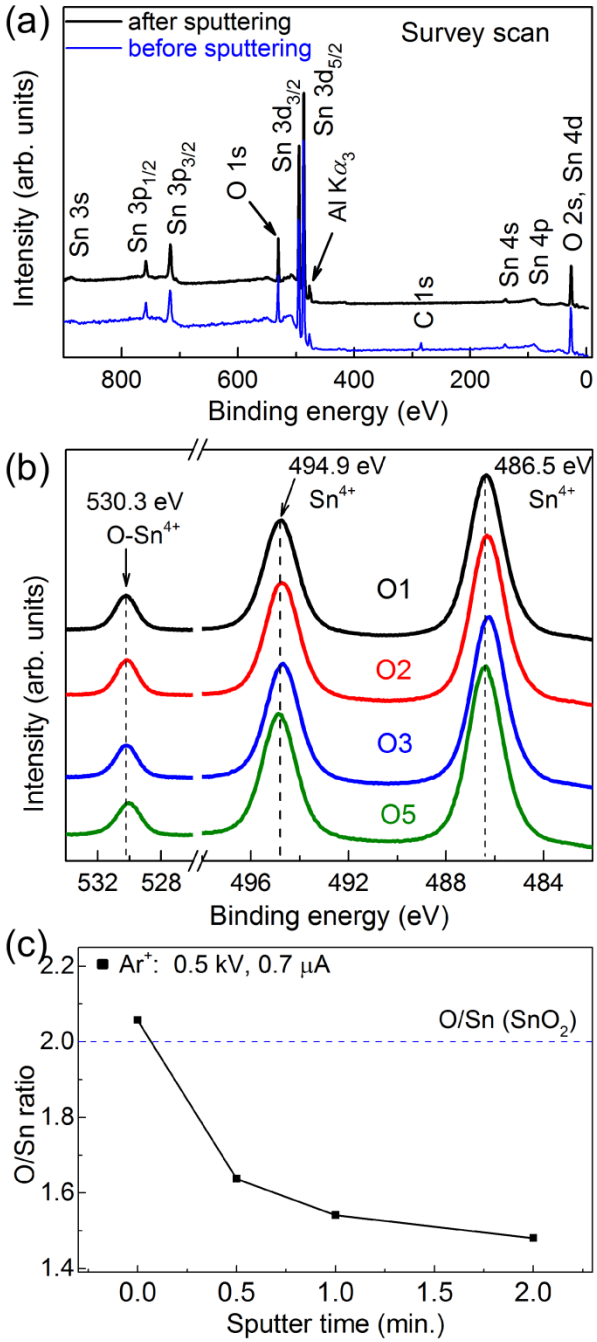

Fig. 6.10. (a) Full XPS spectra of a typical SnO_2 film measured before and after sputter cleaning of the surface. (b) O 1s and Sn 3d core-level XPS spectra of SnO_2 films grown at various O_2 gas flow rates. (c) Evolution of O/Sn atomic ratio as a function of sputtering time.

6.2.5 Raman spectra

Raman spectroscopy was further used to investigate the films in terms of phase structure and crystallinity. Fig. 6.11 shows Raman spectra of SnO_2 films deposited at different O_2 flow rates in comparison with that of the *c*-sapphire substrate. Usually three Raman phonon modes E_g, A_{1g}, and B_{2g} are about detected at 476, 634, and 782 cm^{-1}, respectively, for large single crystal or bulk polycrystalline SnO_2 [10, 11]. For the SnO_2 films grown on *c*-sapphire in this study only E_g (477 cm^{-1}) and A_{1g} (634 cm^{-1}) modes are detected, while the B_{2g} mode is absent. These findings are in accordance with the theoretical predictions for a (100) oriented SnO_2 film summarized in table (4.2). In this case only the A_{1g}, B_{1g}, and E_g modes are symmetry allowed confirming that the SnO_2 films grown on *c*-sapphire possess a (100) orientation.

Under the same measurement conditions, the Raman peak A_{1g} of the sample O4 is the strongest, and has the smallest half width. This means that the SnO_2 film deposited at 40 sccm O_2 has the best crystalline quality. The Raman scattering results are consistent with the XRD and SEM findings.

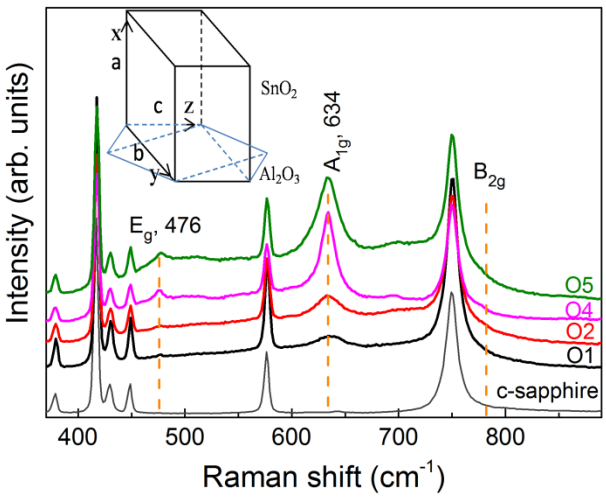

Fig. 6.11. Raman scattering spectra of SnO_2 (100) films grown at different O_2 flow rates on *c*-sapphire.

6.2.6 Optical properties

All five samples in this work are colorless and transparent with an average optical transmittance of over 75% in the wavelength range of 350 to 1400 nm (see Fig. 6.12). Taking into account that the transmittance of the *c*-sapphire substrate is 85%, then the absolute average transmittance of the SnO_2 films must be more than 85% in the visible and infrared range. The transmittance of the sample O4 (grown with 40 sccm O_2) is lower than that of the other samples. This might be due to stronger reflections at the surface and the film-substrate interface of this sample in comparison with other ones, as indicated by the well-defined oscillations shown in the transmittance spectrum of sample O4. Actually, SEM images presented above already reveal a very smooth surface of sample O4.

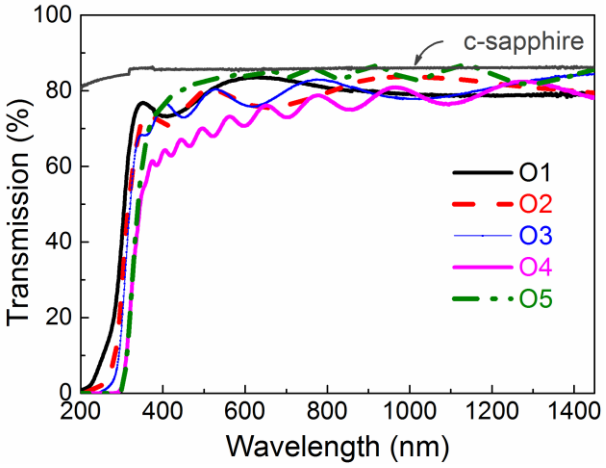

Fig. 6.12. Optical transmittance spectra for SnO_2 films grown at various O_2 flow rates.

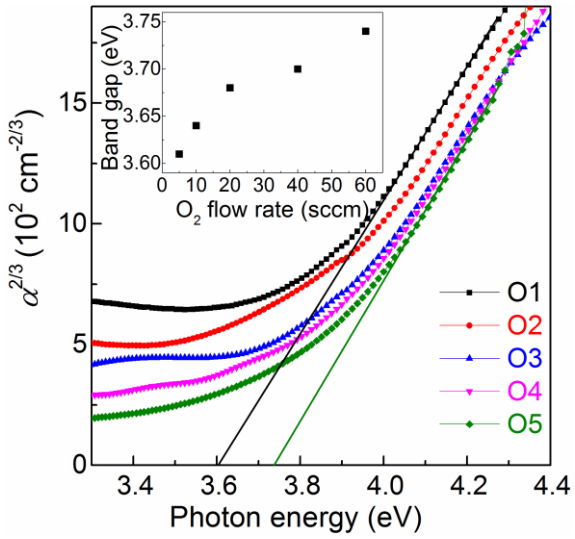

Fig. 6.13. Plots of $\alpha^{2/3}$ as a function of photon energy ($h\nu$) for SnO_2 films grown at various O_2 flow rates.

According to Tauc-theory the dependence of the absorption coefficient on photon energy can be described by E_g in the equation (2.2). Thus, E_g can be extracted from plots of $\alpha^{2/3}$ vs. photon energy. Such $\alpha^{2/3}$ curves of the films grown at different O_2 flow rates are plotted in Fig. 6.13 as a function of photon energy $h\nu$. Extrapolating along the linear portion of the $\alpha^{2/3}$ vs. $h\nu$ curve to zero absorption yields values between 3.61 and 3.74 eV, corresponding to the absorption edge of these SnO_2 films. As seen in the inset of Fig. 6.13, the optical band gaps of SnO_2 films widen gradually with increasing O_2 flow rate. This blue shift of the band edge absorption is observed even though the sample thickness increases with increasing O_2 flow rate. This result also is in accordance with the report of Ji *et al.* [12], and may be attributed to the diminishing of V_O and corresponding absorption in the films with an increase of the O_2 flow rate during the film deposition.

6.2.7 Electrical properties

Electrical properties of the SnO_2 films are evaluated by Hall-effect measurements, which reveal n-type conductivity for all five films. Fig. 6.14 shows the results of four samples deposited at different O_2 flow rates. As the O_2 flow rate increased, both the carrier concentration and mobility decreased from 3×10^{19} to 9×10^{17} cm^{-3}, and from 19 to 2 cm^2/Vs, respectively. This might be explained by the decrease of V_O concentration with increasing O_2 flow rate during the film growth. The mobility value of 19 cm^2/Vs for a carrier concentration of 3×10^{19} cm^{-3} is in agreement with the value of 37 cm^2/Vs reported by Dominguez *et al.* for a comparable carrier concentration [13]. The drop of the mobility by an order of magnitude with decreasing carrier concentration is probably an indication that scattering by charged grain boundaries plays a significant role in the SnO_2 films deposited. As the charge at the grain boundaries is screened at high carrier concentration, the effect of grain boundary scattering is less pronounced and the mobility is higher. This agrees with findings in Ref. [14]. As a result of the decrease of carrier concentration and mobility, the resistivity increased from 0.01 to 3 Ω cm. This result indicates that the carrier concentration, Hall mobility and resistivity of the SnO_2 films depend sensitively on the O_2 flow rate during the film deposition.

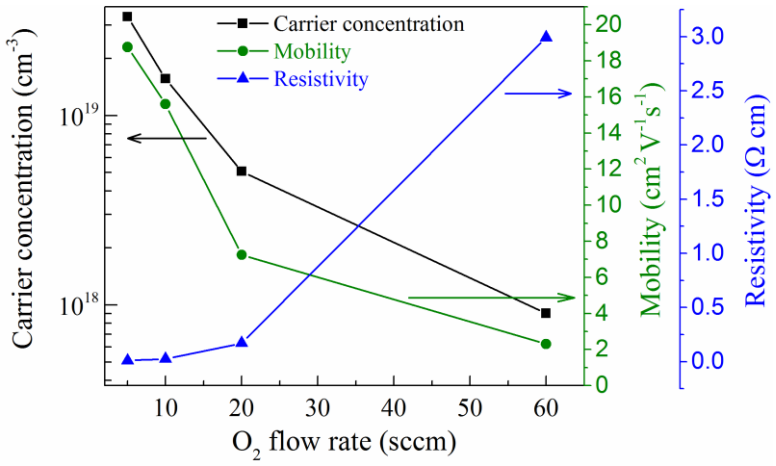

Fig. 6.14. Carrier concentration, Hall mobility and resistivity of SnO_2 films as a function of the O_2 flow rate during the film deposition.

6.2.8 Conclusions

A series of epitaxial SnO_2 films was deposited on *c*-sapphire at various O_2 flow rates. X-ray diffraction, X-ray photoelectron spectroscopy and Raman spectroscopy show that pure-phase SnO_2 films were produced with a rutile structure. Detailed analysis using XRD and SEM reveals that the crystal quality and the morphology of SnO_2 films are dependent on the O_2 flow rate during the film deposition, which causes a variation of the V_O density in the films. Only E_g and A_{1g} Raman modes appear for the SnO_2 films having (100) orientation, when the incident and scattered lights are perpendicular to the film surface, because the B_{2g} mode is forbidden in these scattering geometries. The optical absorption edge of the films increases from 3.61 to 3.74 eV with the increase of the oxygen flow rate. The carrier concentration and Hall mobility of the films decrease from 3×10^{19} to 9×10^{17} cm^{-3} and from 19 to 2 cm^2/Vs, respectively, while the resistivity increases from 0.01 to 3 Ω cm with increasing the O_2 gas flow rate from 5 to 60 sccm.

6.3 Growth mechanism of SnO_2 films on *c*-sapphire

There have been reports in the literature discussing the growth mechanism of SnO_2 (101) on *r*-sapphire [15, 16], but no such reports can be found for the growth of SnO_2 on *c*-sapphire. In this section we discuss the growth mechanism of SnO_2 (100) film on Al_2O_3 (0001). The analysis is based on the results presented in the previous sections, complemented by detailed XRD analysis complemented and SEM studies.

6.3.1 Structural of SnO_2 films

Fig. 6.15 shows XRD results of some samples deposited at substrate temperatures between 510 °C and 650 °C, with an O_2 flow rate of 40 sccm. The XRD θ-2θ scans in Fig. 6.15(a) of these SnO_2 films with different thicknesses are shown in an interval from 36° to 45°. The double peak at about 41.7° originates from the (0006) peak of *c*-plane sapphire. The peak at about 38° to 38.5° can be assigned to the (200) reflections from rutile SnO_2. Another peak at 81° is also observed (not shown in Fig. 6.15) which corresponds to the (400) reflection of SnO_2. No signs of secondary phases can be discerned in these patterns, indicating that the films grown on *c*-sapphire consist of pure-phase tetragonal rutile SnO_2 with a high degree of out-of-plane orientation of $SnO_2(100)\|Al_2O_3(0001)$.

The dashed vertical line in Fig. 6.15(a) indicates the position of the (200) reflection for bulk SnO_2 [17]. These XRD patterns show that with increasing film thickness the angular value of the SnO_2 (200) peak of the films gradually approaches that of bulk SnO_2 (200). At the same time this reveals the presence of compressive strain along the growth direction. However, with increasing thickness relaxation of the SnO_2 in the growth direction occurs. It is interesting to note that the (200) peak of films with a thickness above 200 nm is narrow enough to reveal the doublet structure originating from Cu $K\alpha_1$ and Cu $K\alpha_2$ radiation of the X-ray source, implying a high degree of crystalline order of the SnO_2 films.

The structural properties of the SnO_2 films are further evaluated by rocking curve (ω-scan) analysis. The FWHM of the rocking curve characterizes the out-of-plane atomic ordering. Fig. 6.15(b) shows rocking curves of the (200)-plane of SnO_2 films of different film thicknesses. The SnO_2 film with a thickness of 12 nm exhibits a rocking curve FWHM of 0.019°, with almost no broad diffuse scattering background (top curve in Fig. 6.15b). A similar behavior is observed for the sample with a thickness of 25 nm. For the film with 39 nm thickness, a low intensity bump around the peak starts to appear. This indicates that structural defects are formed, which give rise to out-of-plane disorder in the film. When the

film thickness is 92 nm, the peak shows apparently two components, a sharp line superposed on a broad diffuse scattering background. This implies that disorder in the film increases significantly. The sharp peak of the rocking curve gradually vanishes with increasing film thickness, and the broad diffuse scattering background becomes dominant. When the thickness exceeds about 0.5 µm, only the broad peak remains visible. The evolution of the rocking curve with film thickness suggests that the initially deposited SnO_2 (100) atomic layers are strained to match partly the Al_2O_3 (0001) and virtually only a small density of structural defects exists for the films with thicknesses of 12 and 25 nm. As the film thickness increases, the defect density rapidly increases accompanied by a gradual relaxation of the atomic structure to the bulk state of SnO_2.

However, for thick films the ω-scan FWHM value of (200) reflection decreases again, e.g. for the sample with a thickness of 2.37 µm (bottom curve in Fig. 6.15b). This sample was grown at a substrate temperature of 650°C with a SnI_2 evaporation rate of 0.2 g/h and O_2 gas flow rate of 40 sccm for two hours. Its ω-scan shows that the out-of-plane ordering improves again for films with thicknesses above about 1 µm. Inspecting various samples it was found that in this case the crystallites form large domains, and the defect density decreases. Similar effects have been reported also for the growth of GaN on sapphire [18]. This phenomenon is not affected by the substrate temperature, if the substrate temperature is in the range of 450 - 700 °C.

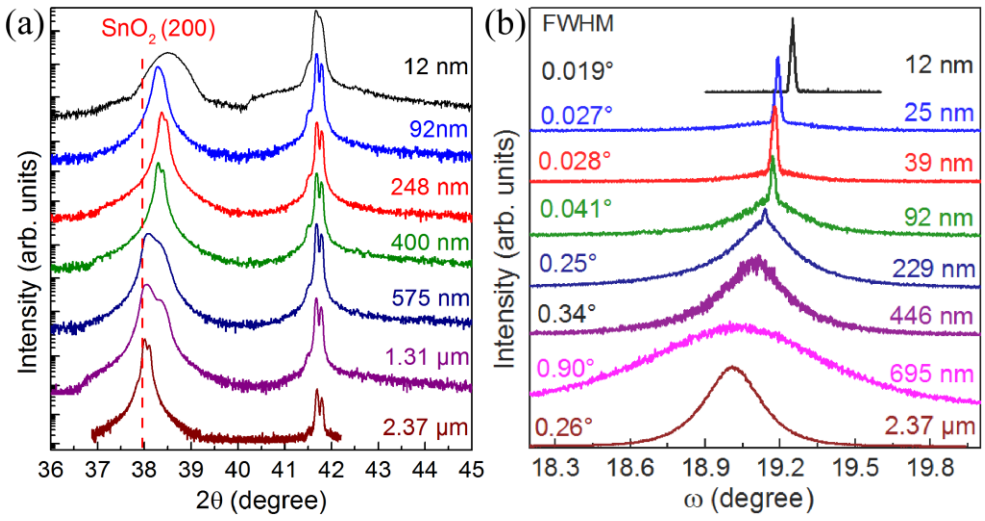

Fig. 6.15. XRD patterns of SnO_2 films deposited on *c*-sapphire at substrate temperature between 510 and 650 °C with an O_2 flow rate of about 40 sccm. (a) θ-2θ scans (on a logarithmic scale) of epitaxial SnO_2 films of various film thicknesses; (b) rocking curves of the (200)-plane of SnO_2 films of various thicknesses.

To gain information about the in-plane ordering, ϕ-scan measurements were performed on a sample with a thickness about 980 nm deposited at a substrate temperature of 550 °C, and an O_2 flow rate of 40 sccm. Fig. 6.16 presents the XRD ϕ-scan recorded in the SnO_2 {110}- and Al_2O_3 {11$\bar{2}$3}-plane, as well as SnO_2 {101}- and Al_2O_3 {10$\bar{1}$2}-plane, respectively. It should be noted that the {110}- and {101}-plane of rutile SnO_2 single crystals both have a two-fold symmetry along the [100] rotation axis. In contrast, the SnO_2 films exhibit a six-fold symmetry originating from the formation of the three types of domains discussed in section 6.2 (see Fig. 6.5). According to our analysis of the ϕ-scans, the in-plane alignment can be described as $SnO_2[0\bar{1}0] \| Al_2O_3<1\bar{2}10>$ or equivalently $SnO_2[001] \| Al_2O_3<\bar{1}010>$.

In agreement with our finding, Dominguez and Liu *et al.* found the existence of domains of a rectangular shape and an 120° relative rotation in the plane-view TEM and corresponding selected-area electron diffraction patterns [2, 19].

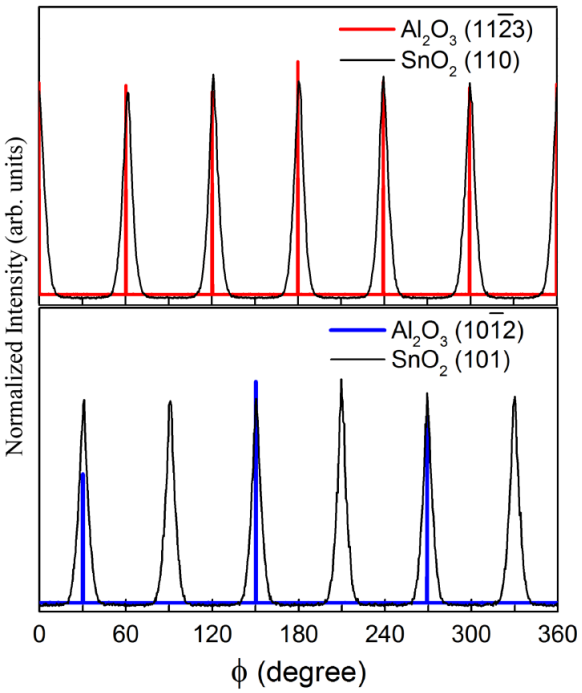

Fig. 6.16. Four-circle XRD ϕ-scans of a SnO_2 films with a thickness of 980 nm, which was deposited at a substrate temperature of 550 °C. The scans were recorded at SnO_2 {110} (2θ = 26.5°, χ = 44.6°) and Al_2O_3 {11$\bar{2}$3} (2θ = 43.3°, χ = 61.2°), as well as SnO_2 {101} (2θ = 33.9°, χ = 55.7°) and Al_2O_3 {10$\bar{1}$2} (2θ = 25.6°, χ = 57.6°).

To characterize the crystallinity of the films, HRXRD in-plane measurements were performed for a SnO_2 sample which was deposited at a substrate temperature of 455 °C for 4 hours yielding a thickness of 230 nm. Fig. 6.17(a) shows the ω-2θ scan around the symmetric SnO_2 (200) reflection. A slightly asymmetric (200) peak with weak thickness

interference fringe structure is visible. The analysis of the fringe structure yields a thickness of the SnO_2 film of 230 nm, in good agreement with the value of 248 nm estimated from the interference oscillations detected in the optical transmittance. The (200) peak of the film is located at 38.368°, which is shifted towards higher angle compared to bulk SnO_2. The corresponding *a*-axis lattice parameter is calculated to be 4.688 Å, i.e. smaller than that of the bulk SnO_2 (4.738 Å), indicating that compressive strain exists in the film along the growth direction of [100].

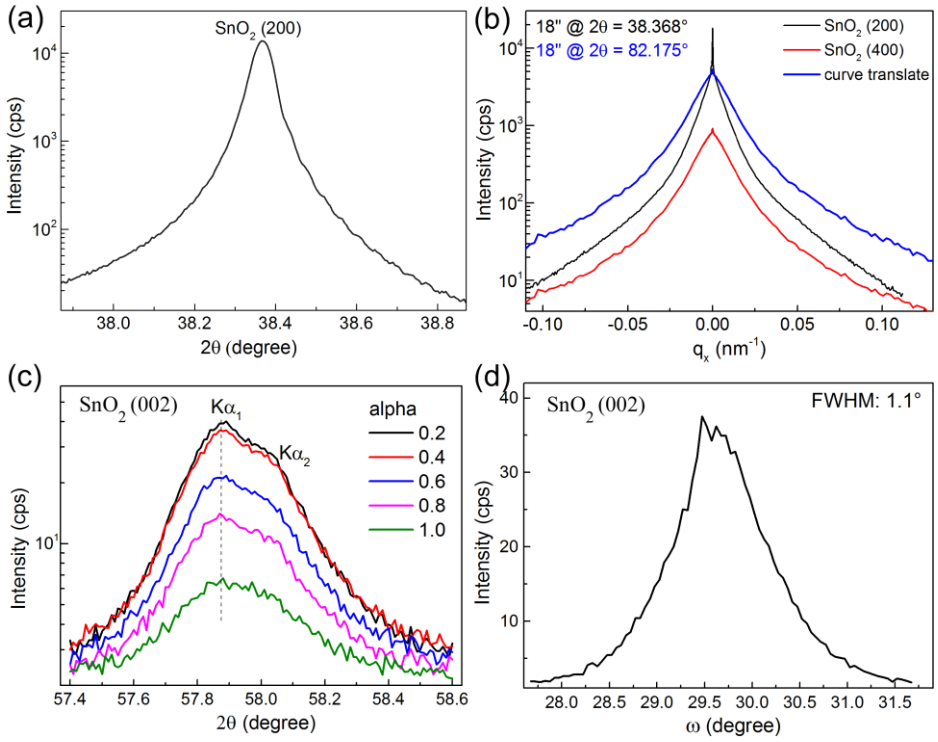

Fig. 6.17. HRXRD results of a SnO_2 film with a thickness of 230 nm, (a) θ-2θ scan of the film out-of-plane; (b) transverse scans through the SnO_2 (200) and (400) reflections; (c) GIID measurement at the in-plane SnO_2; (002) reflection with depth profile; (d) ω-scan at SnO_2 (002) reflection.

Fig. 6.17(b) displays the symmetric ω-scans (converted to q_x) at the SnO_2 (200)- and (400)-planes of the same sample. Each of the diffraction traces consists of a two-component contribution with an extremely sharp (resolution limited) Bragg part at the SnO_2 (200) or (400) position and a broad background due to diffuse scattering, (as seen before in Fig. 6.15b). The FWHM of the sharp peak for both reflections is 18". This very narrow line shape of the peak implies long-range structural correlations. The intensity ratio of the sharp to the diffuse part decreases with the diffraction order. The origin of the diffuse scattering is due to the angular spreading of the *a*-axis orientation (tilt), vertical domain boundaries, and dislocations in the film. In fact, the FWHM of the diffuse scattering increases in q_x (1/nm) with the order of diffraction, but decreases in ω (degree).

Similar observations were reported for GaN on sapphire [20] and other systems with anisotropic substrate-layer adhesion, a theoretical description was first given by Miceli and Palmström [21]. The diffraction behavior stems from anisotropic defect systems which form highly localized strain fields. The kind and disorder of the main defects define the vanishing of the Bragg part as well as the shape and broadening of the diffuse background with the order of diffraction. Moreover, the evolution with thickness (Fig. 6.15b) can be described in the same manner. Starting with the two-line shape model for thin films, the vanishing defect anisotropy leads in case of the thick films to the common Bragg broadening caused by bulk dislocations etc (the bottom curve in Fig. 6.15b).

Fig. 6.17(c) shows the depth profile of GIID θ-2θ measurements at the SnO_2 (002) Bragg reflection, which is obtained by varying the incoming angle α of the X-ray beam. At α = 0.2° (the top curve), the curve shows the reflection at the very near surface region of the SnO_2 film, at α = 1.0° (the bottom curve), the curve reveals the reflection from the entire thickness of the SnO_2 film. The peak maximum stays almost constant with increasing penetration depth. The data of Fig. 6.17(c) were fitted to Pseudo-Voigt functions in order to separate Cu $K\alpha_1$ and Cu $K\alpha_2$ contributions of the incident radiation (not shown here). According to the fitted position of the Cu $K\alpha_1$ reflection, the lattice parameter *c* of the SnO_2 film is calculated to be 3.184 Å, very close to the value of 3.187 Å for bulk SnO_2. It indicates that due to very large lattice mismatch between SnO_2 (100) and Al_2O_3 (0001), the in-plane growth along the *c*-axis of SnO_2 is almost relaxed already at a very early stage of the growth.

Fig. 6.17(d) shows the ω-scan at the SnO_2 (002) reflection. The FWHM is 1.1°, obviously larger than the FWHM (18 arc seconds) of the out-of-plane (200) reflection, indicating the strong anisotropic initial growth, i.e. the substrate is evidently less efficient in organizing the film orientation in-plane than out-of-plane. Similar observations were reported for the heteroepitaxial growth of GaN on *c*-sapphire substrates [22]. Likely reasons are the large lattice mismatch between SnO_2 and Al_2O_3 of 16% along the SnO_2 [002] direction.

Two- or three-dimensional reciprocal space mappings (2D- and 3D-RSM) are often utilized to characterize the degree of strain relaxation, lattice parameters and assessment of defect propagation. Fig. 6.18(a) is an asymmetric 3D ω-2θ scan of the sample with thickness of 230 nm, whose HRXRD spectra are shown in Fig. 6.17. The two weak peaks at about 93° and 91° correspond to the SnO_2 (420) and (411) reflections, respectively. The intensity of the (411) reflection is stronger than that of (420) reflection. The intensity distribution of the reflections (420) and (411) is in agreement with the ICDD PDF No. 41-1445.

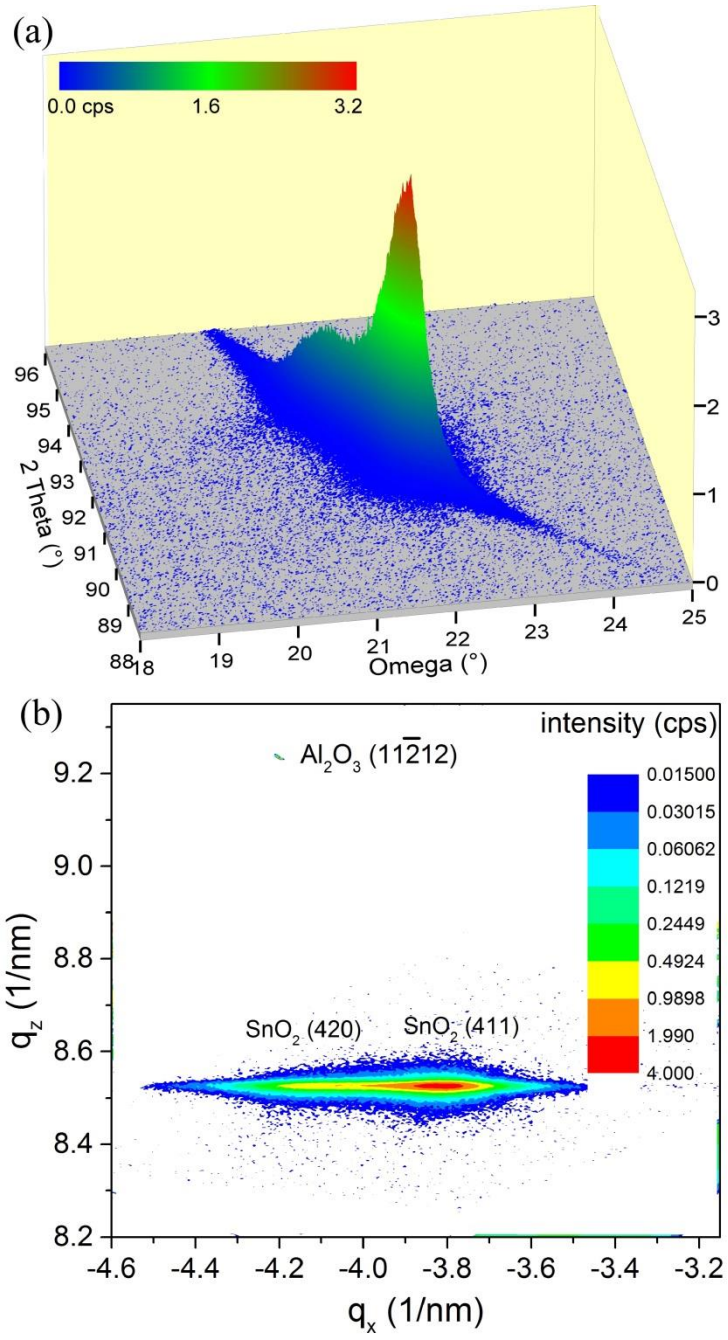

Fig. 6.18. SnO_2 film with a thickness of 230 nm, whose HRXRD spectra shown in Fig. 6.17: 3D-Omega map over 2θ (a), and 2D-RSM (b) around the SnO_2 (420) and (411), and around Al_2O_3 ($11\bar{2}12$) Bragg reflections.

Fig. 6.18(b) shows the converted RSM of this film. The intensity distribution (-4.201, 9.234) corresponding to the ($11\bar{2}12$) reflection of sapphire is confined in a very narrow region of reciprocal space. This behavior is expected for the diffraction from single crystals. According to the RSM measurement the lattice parameter *a* and *c* of Al_2O_3 are 4.761 and 12.995 Å, respectively. These results are consistent with the ICDD PDF No.46-1212 for Al_2O_3 (a = 4.7587 Å and c = 12.9929 Å).

In contrast, the diffuse background scattering of SnO_2 extends over a much wider region of reciprocal space. According to the q_z value (~ 8.52 nm^{-1}) of the SnO_2 (420) Bragg reflection the lattice parameter *a* of this film is 4.69 Å. It is in good agreement with the result, which is estimated from the data in Fig. 6.17(a). Due to the influence of the SnO_2 (411) Bragg reflection, the lattice parameter *b* of this film cannot be estimated.

The SnO_2 (020) reflection is not accessible using GIID measurement. In order to evaluate the in-plane lattice parameter *b* precisely, reciprocal space mapping (RSM) was carried out on a sample deposited at a substrate temperature of 650 °C with a thickness of about 500 nm (due to the small thickness, the SnO_2 (420) reflection of the sample shown in Fig. 6.18 is very weak, not enough to estimate the lattice parameter *b* of SnO_2 film correctly).

Fig. 6.19(a) shows the RSM of the symmetric SnO_2 (200) and Al_2O_3 (0006) reflections. The peak of SnO_2 (200) is running strictly in the q_z direction, indicating its origin to be located parallel to the surface in real space. The SnO_2 reflection extends over much wider regions of the reciprocal space due to the diffuse background scattering, which is caused by the structure defects in the SnO_2 film. Particular with regard to the q_x broadening, the RSMs indicate reduced in-plane coherence lengths. According to the q_z values (4.234 nm^{-1} for SnO_2 (200), and 4.617 nm^{-1} for Al_2O_3 (0006)) of the reflections in the RSM, the lattice parameters *a* of the SnO_2 film and *c* of the Al_2O_3 substrate are determined to be 4.724 Å and 12.995 Å. The two tilted lines in Fig. 6.19(a) are due to a detector streak (DS), which is caused by an electronic artifact of the area detector. Therefore, they are not of interest here.

Fig. 6.19(b) shows the RSM of the asymmetric (420) and (411) reflections of this SnO_2 film, and the $(11\bar{2}12)$ reflection of the Al_2O_3 substrate. The peak around (-4.20 nm^{-1}, 8.47 nm^{-1}) corresponds to the SnO_2 (420) reflection and indicates that the lattice parameters *a* and *b* of SnO_2 are 4.722 Å and 4.762 Å, respectively. These results demonstrate that the out-of-plane *a*-axis is slightly compressed, and the in-plane *b*-axis is elongated compared to bulk SnO_2 for this film with a thickness of 500 nm. It should be noted that the lattice parameter *b* of SnO_2 is very close to that of the Al_2O_3 unit cell 4.759 Å. This demonstrates that the in-plane *b*-axis of the SnO_2 film matches the substrate very well.

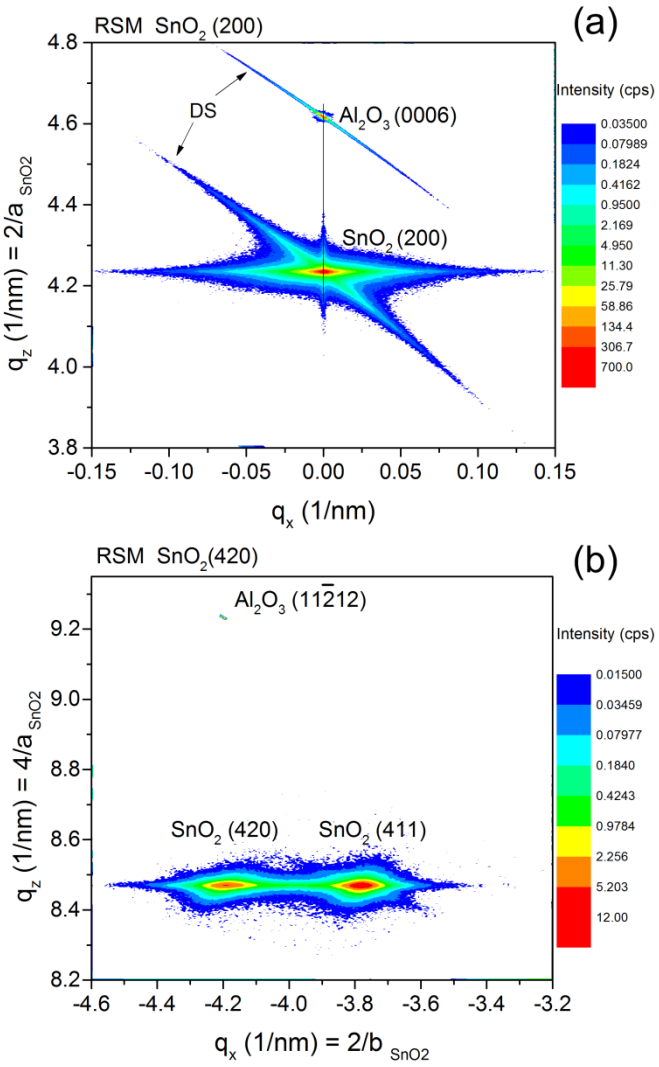

Fig. 6.19. Reciprocal space mapping of a 500 nm SnO_2 film deposited at a substrate temperature of 650 °C with an O_2 flow rate of 40 sccm. (a) RSM of the symmetric SnO_2 (200) and Al_2O_3 (0006) reflections, (b) RSM of the asymmetric (420) and (411), and (11$\bar{2}$12) Bragg reflections of SnO_2 film and Al_2O_3 substrate, respectively.

6.3.2 Determination of the characteristic thickness of the growth mode change

The lattice parameter *a* of the SnO_2 films as a function of the film thickness obtained by XRD is plotted in Fig. 6.20(a). The blue dashed line indicates the lattice parameter *a* of bulk SnO_2. Although the samples were grown at different substrate temperatures, O_2 gas flow rates and deposition duration etc. the data reveal a clear trend, i.e. the lattice parameter *a* of the SnO_2 (100) films on *c*-sapphire shifts towards the value of bulk SnO_2

with increasing film thickness. This suggests that the SnO_2 (100) atomic layers first deposited are strained to match the Al_2O_3 (0001) along the *b*-axis of SnO_2 and a coherent interface along this direction is formed (see discussion of Fig. 6.19), but along the *c*-axis it is relaxed (discussion of Fig. 6.17c). Thus, along the growth direction the lattice parameter *a* is compressed (see discussion of Fig. 6.15a and Fig. 6.17a). As the layer thickness increases, the strain energy also increases. When the thickness is large enough, relaxation occurs and the crystalline lattice of the film approaches its bulk structure.

The FWHM of the rocking curves of the SnO_2 (200)-plane reflections are plotted in Fig. 6.20(b), (black squares) as a function of the film thickness. Very thin films exhibit a similar rocking curve FWHM of 0.02°, but beyond 50 nm, this value drastically increases. It should be noted that the nominal film thickness, where the FWHM of the peak starts to increase, is characteristic for the change of growth mode of SnO_2 (100) on Al_2O_3 (0001), where it changes from isolated island growth with the three different preferential orientations to a merging of these islands leading to a significant formation of additional strain, domain boundaries, planar defects, and stacking faults, which lead to the appearance of the broad diffuse scattering in the ω-scans. This characteristic thickness should therefore be slightly smaller than 50 nm.

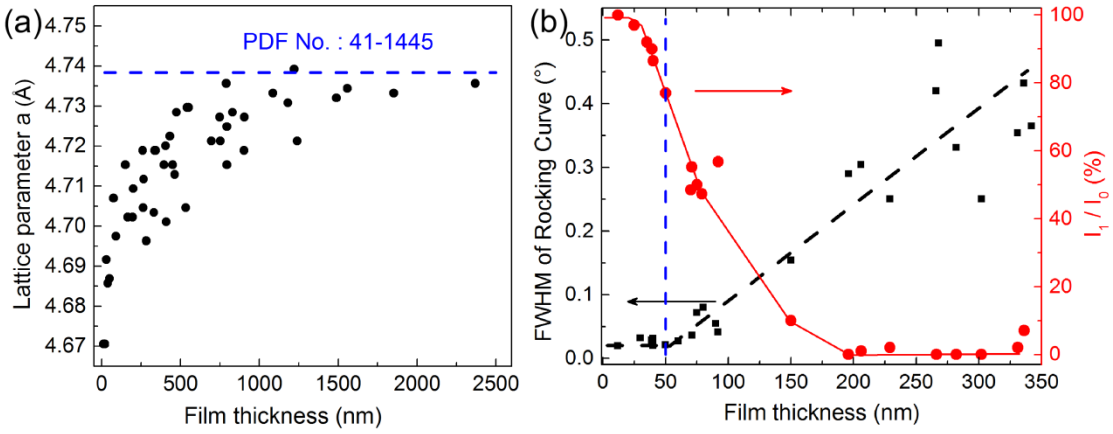

Fig. 6.20 (a) Experimental lattice parameter *a* of SnO_2 films as a function of SnO_2 film thickness. (b) FWHM of the rocking curve of the SnO_2 (200) reflection (black squares) and ratio (red circles) of the intensity of the sharp peak and the intensity of the total peak of the ω-scan of the SnO_2 (200) reflection as a function of film thickness. The dashed vertical line indicates the characteristic thickness of 50 nm.

In Fig. 6.15(b), the diffraction patterns consist of two components, an extremely sharp line and a broad background. The red solid line in Fig. 6.20(b) shows the intensity ratio I_1/I_0 of the films as a function of film thickness. I_1 denotes the intensity of the sharp peak in the ω-scan of the SnO_2 (200) reflection, which can be attributed to the initially deposited layer and stands for very good out-of-plane ordering. I_0 is the total intensity of the ω-scan

of the SnO_2 (200) reflection (seen in Fig. 6.15b). The steep decrease of the I_1/I_0 ratio at about 50 nm suggests that a transformation of the growth mode of the SnO_2 (100) films on *c*-sapphire takes place after the initial stages of the growth.

6.3.3 Morphology of SnO_2 films

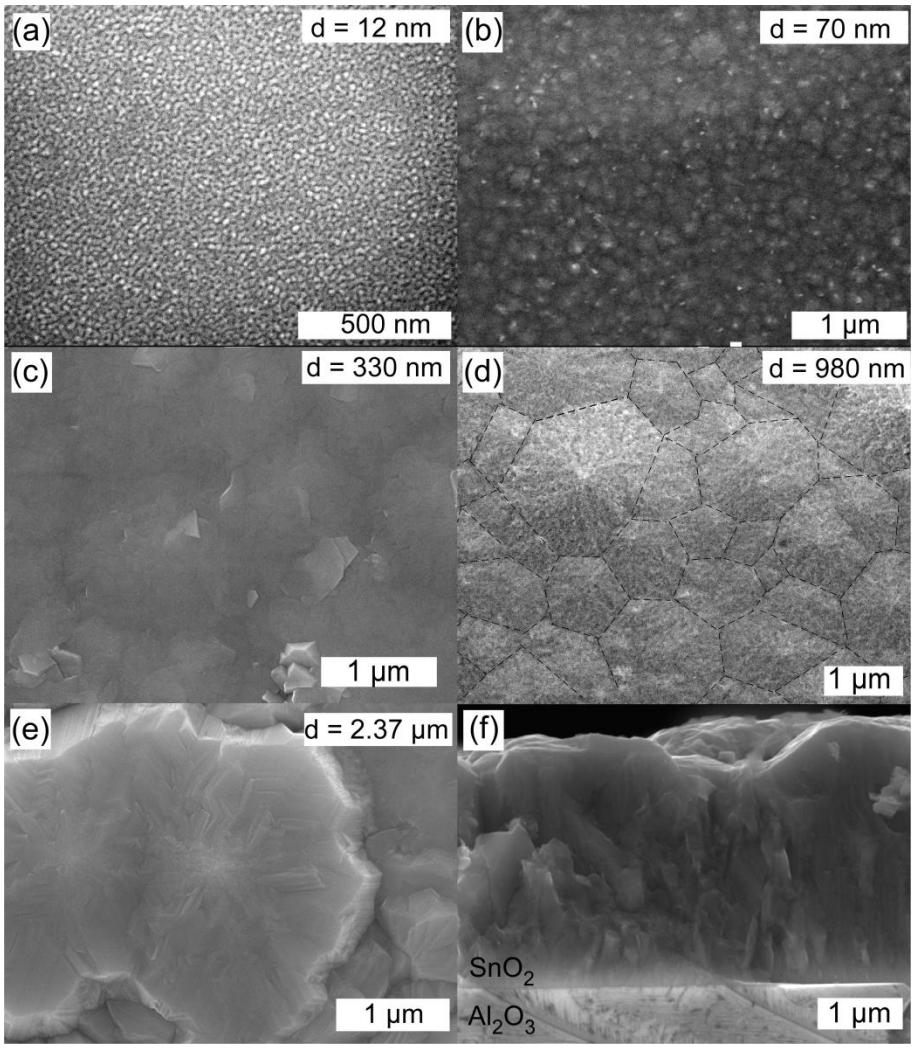

Fig. 6.21. SEM images of SnO_2 films, (a) a film with a thickness of 12 nm, ω-scan FWHM of 0.019°, (b) a film with a thickness of 70 nm, FWHM of 0.036°, (c) a film with a thickness of 330 nm, FWHM of 0.182°, (d) a film with a thickness of 980 nm, FWHM of 0.213°, (e) a film with thickness of 2.37 µm, FWHM of 0.26°; (f) the cross-section view of the film in Fig. e.

SEM measurements were performed to obtain information on grain or domain boundaries and on the film morphology which might yield additional insight how the growth process takes place. The surface morphologies of films of different thicknesses are shown in Fig.

6.21(a)-(e). Fig. 6.21(a) shows the surface of a 12 nm SnO_2 sample. The surface consists of small grains uniformly distributed with grain sizes between 10 and 20 nm. It does not reveal a closed surface. In Fig. 6.21(b) the surface of a film of about 70 nm thickness is shown. The crystalline grains seem to coalesce in this film. When the film thickness reaches 330 nm (in Fig. 6.21c), the sample exhibits a flat surface consisting of crystalline domains of µm-sizes. Increasing the film thickness further some domains start to exhibit a hexagonal shape (in Fig. 6.21d). That can be regarded to arise from the three possible orientations of the rectangular SnO_2 unit cells on the hexagonal *c*-sapphire surface. The three equivalent rectangular unit cells are rotated by 120° with respect to each other. Therefore the surface of high-quality SnO_2 thin films exposes hexagonal domains, in accordance with the symmetry deduced from the XRD ϕ-scans presented above, which showed a six-fold instead of two-fold symmetry of the SnO_2 films (its ϕ-scan show in Fig. 6.16). Fig. 6.21(e) and f show the plan-view and cross-sectional morphology of the film with a thickness of 2.37 µm. The XRD θ-2θ scan and ω-scan of this film were shown in Fig. 6.15 as the bottom curves. Large crystal domains are observed in the plan-view. These huge SnO_2 domains also are visible in the cross-section image.

6.3.4 Optical properties of SnO_2 films

Fig. 6.22 shows the optical transmittance spectra of SnO_2 samples with a range of thickness as a function of the incident light wavelength in the range of 200 - 1300 nm. For all films the average transmittance in the visible range is over 75%, while it was about 85% for *c*-sapphire. The absolute average transmittance of the SnO_2 films is thus more than 85%. The transmittance above the band gap of the thin films with thickness 12, 25, 71 and 92 nm does not completely go down to 0, which is not only due to their small thickness, but possibly due to the growth following a Volmer-Weber mode, i.e. the initial growth is three-dimensional mode. Many grains form SnO_2 islands on the substrate. The SnO_2 films are not completely closed yet and small gaps remain between the SnO_2 islands. Therefore a fraction of photons with energies above the band gap of SnO_2 may pass through the gaps between the islands. The transmittance of the high energy photons decreases with increasing film thickness, because spatial openings between the crystallites decrease due to the coalescence of the islands with increasing film thickness. When the thickness of film reaches about 100 nm, the film is almost completely closed. Therefore the transmittance of the light with the energy above the band gap of SnO_2 for thick films goes down to 0.

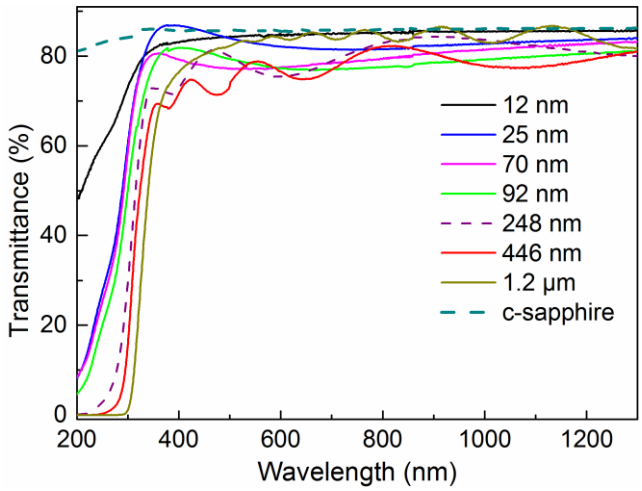

Fig. 6.22. Optical transmittance spectra of epitaxial SnO_2 (100) films with different thicknesses.

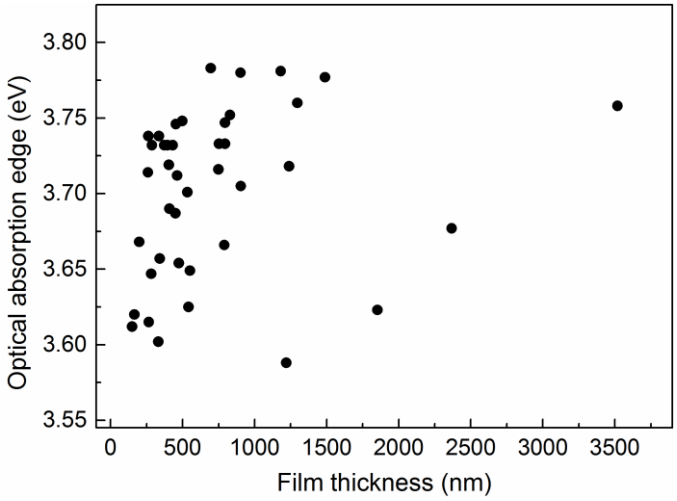

Fig. 6.23. Optical absorption edge of the epitaxial SnO_2 (100) films on *c*-sapphire with different thicknesses.

Following the Tauc-theory, $\alpha^{2/3}$ curves of the films grown on *c*-sapphire were analyzed as a function of photon energy $h\nu$ (not shown here). Extrapolating along the linear portion of the $\alpha^{2/3}$ vs. $h\nu$ curve to zero absorption yields the values of the optical absorption edge. The optical absorption edge of all SnO_2 films, whose lattice parameter *a* is shown in Fig. 6.20(a), is plotted in Fig. 6.23 as a function of the film thickness. The optical absorption edge of these films is in the range of 3.59 - 3.78 eV. It is independent of the film thickness. The reason is the same as that discussed in section 5.3. We did not use polarized light to identify the anisotropic absorption edges of the films. Therefore, the films exhibit absorption edges in between the anisotropic absorption edges of SnO_2 single crystal, and no clear trends with thickness are observed.

6.3.5 Growth mechanism

Based on the analysis described above, we believe that heteroepitaxial growth of SnO_2 on *c*-sapphire initially starts in a Volmer-Weber growth mode. The SnO_2 growth begins by the nucleation of discrete islands with rectangular unit cells about 3.187 (relaxed) and 4.759 Å (strained) in-plane. There are three possible orientations of these unit cells of the SnO_2 islands with respect to the *c*-sapphire substrate. These orientations are rotated by 120° with respect to each other. With increasing deposition time, the islands grow, and finally coalesce forming a continuous film. This transition from island growth to a continuous film occurs at a thickness of about 50 nm. At that stage the density of domain boundaries, grain boundaries and other defects increases dramatically (seen Fig. 6.24a, b). This growth model is supported by our results for SnO_2 films with thicknesses below 1 µm (Fig. 6.15 and Fig. 6.20). When the thickness of film increases further, larger SnO_2 domains form and the density of defects in the film decreases again (Fig. 6.24c). The ordering of the film becomes better (as, for instance, seen for the sample with a thickness of 2.37 µm in Fig. 6.15 and Fig. 6.21). The film with a thickness of 2.37 µm possesses large domains and less domain boundaries compared to the films with thicknesses in the range from 300 nm - 1 µm. A similar situation was found by Vasheghani Farahani *et al.* for SnO_2 (101) films on *r*-sapphire. Those authors suggested that the dislocations originate at the interface between film and substrate, and their density decreases with increasing film thickness [16]. In our case, the different defects start to occur at a film thickness of about 50 nm, when the initially separated nuclei forming the grains start to coalesce and grain boundaries are formed. This defect formation is significant as three different orientations of the unit cells of the SnO_2 nuclei and domains exist on *c*-sapphire. Above 1 µm film thickness the defects density decreases again due to the formation of larger SnO_2 domains (see in Fig. 6.24c). These findings are independent of growth temperature in the range of substrate temperatures from 455 °C to 650 °C.

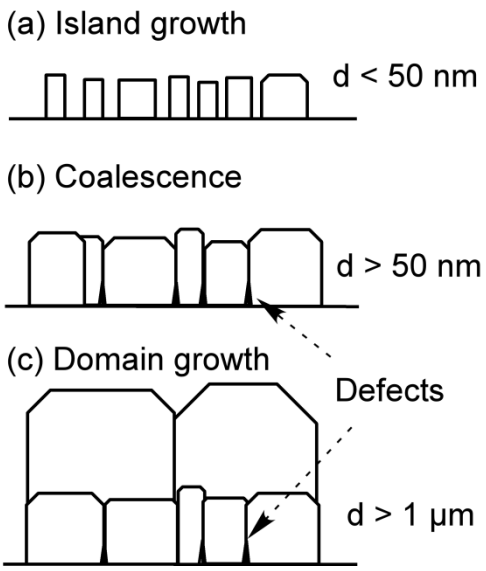

Fig. 6.24. Schematic diagrams showing the growth process of SnO_2 on *c*-sapphire as cross-section views.

6.3.6 Conclusions

Epitaxial SnO_2 (100) films grown on *c*-sapphire were studied. XRD and HRXRD analysis showed that pure-phase SnO_2 films with a rutile structure were formed. Detailed analysis using HRXRD and SEM reveals that the crystalline quality and the morphology of SnO_2 films vary significantly with film thickness. The SnO_2 epitaxy on *c*-sapphire starts in the Volmer-Weber growth mode. In the initial growth, the in-plane unit cell constants of SnO_2 along *c* axis and *b* axis are 3.187 (relaxed) and 4.759 Å (strained), respectively. At a characteristic layer thickness of about 50 nm the islands begin to merge, until ~100 nm leading to a closed SnO_2 (100) film growth on *c*-sapphire with a characteristic domain structure.

References

[1] R. Bachelet, F. Valle, I.C. Infante, F. Sánchez, J. Fontcuberta, *Step formation, faceting, and bunching in atomically flat $SrTiO_3$ (110) surfaces*, Appl. Phys. Lett., 91 (2007), 251904.

[2] J.E. Dominguez, L. Fu, X.Q. Pan, *Epitaxial nanocrystalline tin dioxide thin films grown on (0001) sapphire by femtosecond pulsed laser deposition*, Appl. Phys. Lett., 79 (2001), 614-616.

[3] B.B. Kosicki, D. Kahng, *Preparation and Structural Properties of GaN Thin Films*, Journal of Vacuum Science & Technology, 6 (1969), 593-596.

[4] *a) Joint Committee for Powder Diffraction (JCPDS) File No. 46-1212, International Center for Diffraction Data (ICDD), 1990. b) JCPPDS File No. 41-1445, ICDD*, (1989).

[5] R.N. Ghoshtagore, *Mechanism of CVD Thin Film SnO_2 Formation*, J. Electrochem. Soc., 125 (1978), 110-117.

[6] A.R. Knudson, D.J. Nagel, P.G. Burkhalter, K.L. Dunning, *Aluminum X-Ray Satellite Enhancement by Ion-Impact Excitation*, Phys. Rev. Lett., 26 (1971), 1149-1152.

[7] R.O. Ansell, T. Dickinson, A.F. Povey, P.M.A. Sherwood, *Quantitative use of the angular variation technique in studies of tin by X-ray photoelectron spectroscopy*, Journal of Electron Spectroscopy and Related Phenomena, 11 (1977), 301-313.

[8] L.Y. Liang, Z.M. Liu, H.T. Cao, X.Q. Pan, *Microstructural, Optical, and Electrical Properties of SnO Thin Films Prepared on Quartz via a Two-Step Method*, ACS Applied Materials & Interfaces, 2 (2010), 1060-1065.

[9] R.G. Egdell, S. Eriksen, W.R. Flavell, *Oxygen deficient SnO_2 (110) and TiO_2 (110): A comparative study by photoemission*, Solid State Commun., 60 (1986), 835-838.

[10] R.S. Katiyar, P. Dawson, M.M. Hargreave, G.R. Wilkinson, *Dynamics of the rutile structure III. Lattice dynamics, infrared and Raman spectra of SnO_2*, Journal of Physics C: Solid State Physics, 4 (1971), 2421.

[11] P.S. Peercy, B. Morosin, *Pressure and Temperature Dependences of the Raman-Active Phonons in SnO_2*, Physical Review B, 7 (1973), 2779-2786.

[12] Y.-C. Ji, H.-X. Zhang, X.-H. Zhang, Z.-Q. Li, *Structures, optical properties, and electrical transport processes of SnO_2 films with oxygen deficiencies*, physica status solidi (b), 250 (2013), 2145-2152.

[13] J.E. Dominguez, X.Q. Pan, L. Fu, P.A. Van Rompay, Z. Zhang, J.A. Nees, P.P. Pronko, *Epitaxial SnO_2 thin films grown on ($\bar{1}012$) sapphire by femtosecond pulsed laser deposition*, J. Appl. Phys., 91 (2002), 1060-1065.

[14] H. Hosono, D.C. Paine, *Handbook of Transparent Conductors*, Springer, New York Heidelberg Dordrecht London, (2010).

[15] M.E. White, M.Y. Tsai, F. Wu, J.S. Speck, *Plasma-assisted molecular beam epitaxy and characterization of SnO_2 (101) on r-plane sapphire*, J. Vac. Sci. Technol. A, 26 (2008), 1300-1307.

[16] S.K. Vasheghani Farahani, T.D. Veal, A.M. Sanchez, O. Bierwagen, M.E. White, S. Gorfman, P.A. Thomas, J.S. Speck, C.F. McConville, *Influence of charged-dislocation density variations on carrier mobility in heteroepitaxial semiconductors: The case of SnO_2 on sapphire*, Physical Review B, 86 (2012), 245315.

[17] G.J. McCarthy, J.M. Welton, *X-Ray Diffraction Data for SnO_2. An Illustration of the New Powder Data Evaluation Methods*, Powder Diffraction, 4 (1989), 156-159.

[18] K. Hiramatsu, S. Itoh, H. Amano, I. Akasaki, N. Kuwano, T. Shiraishi, K. Oki, *Growth mechanism of GaN grown on sapphire with A1N buffer layer by MOVPE*, J. Cryst. Growth, 115 (1991), 628-633.

[19] D. Liu, Q. Wang, H.L.M. Chang, H. Chen, *Variant structure in metal-organic-chemical-vapor-deposition-derived SnO_2 thin films on sapphire (0001)*, J. Mater. Res., 10 (1995), 1516-1522.

[20] J. Bläsing, A. Krost, J. Hertkorn, F. Scholz, L. Kirste, A. Chuvilin, U. Kaiser, *Oxygen induced strain field homogenization in AlN nucleation layers and its impact on GaN grown by metal organic vapor phase epitaxy on sapphire: An x-ray diffraction study*, J. Appl. Phys., 105 (2009), 033504.

[21] P.F. Miceli, C.J. Palmström, *X-ray scattering from rotational disorder in epitaxial films: An unconventional mosaic crystal*, Physical Review B, 51 (1995), 5506-5509.

[22] B. Heying, X.H. Wu, S. Keller, Y. Li, D. Kapolnek, B.P. Keller, S.P. DenBaars, J.S. Speck, *Role of threading dislocation structure on the x-ray diffraction peak widths in epitaxial GaN films*, Appl. Phys. Lett., 68 (1996), 643-645.

7 SnO_2 thin films on *r*-sapphire

Before this subject is discussed, the structural similarities between *r*-sapphire and SnO_2 (101) are discussed. The lattice mismatch (11.3%) between SnO_2 and the *r*-plane sapphire along SnO_2 $[10\bar{1}]$ is smaller than that between SnO_2 and *c*-plane sapphire (16.0%). Many studies have investigated the structure, morphology, stoichiometry, optical etc. properties of SnO_2 films on *r*-sapphire. In our study we deposited a series of SnO_2 thin films on *r*-sapphire by CVD to investigate the various properties of the films.

The epitaxial relationship between the grown SnO_2 (101) film and Al_2O_3 $(01\bar{1}2)$ is illustrated in Fig. 7.1. The lattice parameters are based on ICDD PDF No. 46-1212 and 41-1445 for Al_2O_3 and SnO_2, respectively.

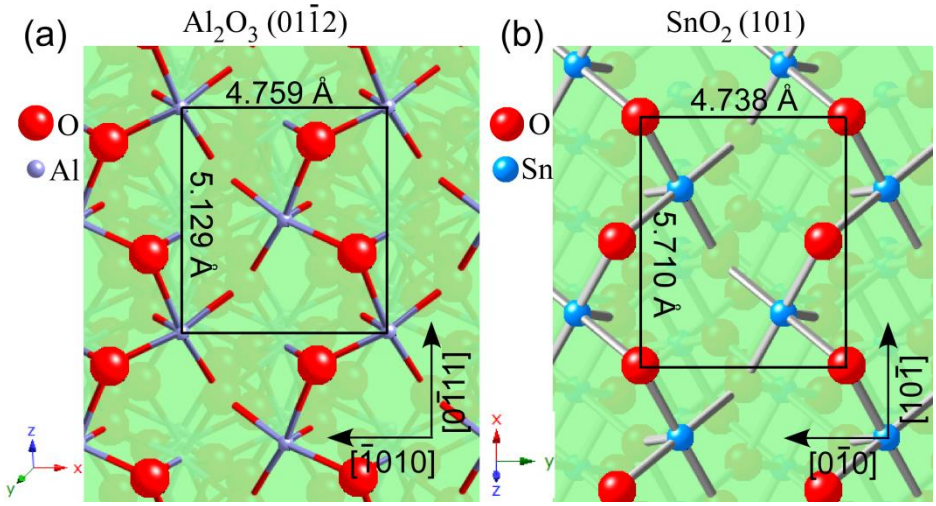

Fig. 7.1. Schematic diagram of the crystalline: (a) Al_2O_3 $(01\bar{1}2)$-plane, (b) SnO_2 (101)-plane. The surface unit cells are also indicated.

7.1 Characterization of the quality of the *r*-sapphire substrate

Using essentially the same experimental procedure as discussed in section 6.1 the miscut polar angle θ of the *r*-sapphire substrate is determined by XRD ω-scans. Fig. 7.2(a) shows the ω-scans of the $(10\bar{1}2)$ reflection of an Al_2O_3 sapphire. The substrate is rotated by steps of 45° along the surface axis. The corrected angle of the sample plate is recorded in Fig.

7.2(b). According to the corrected angles between maximum and minimum, the miscut polar angle is 0.083° (= $\frac{0.12°-(-0.046°)}{2}$) for this typical *r*-plane sapphire sample.

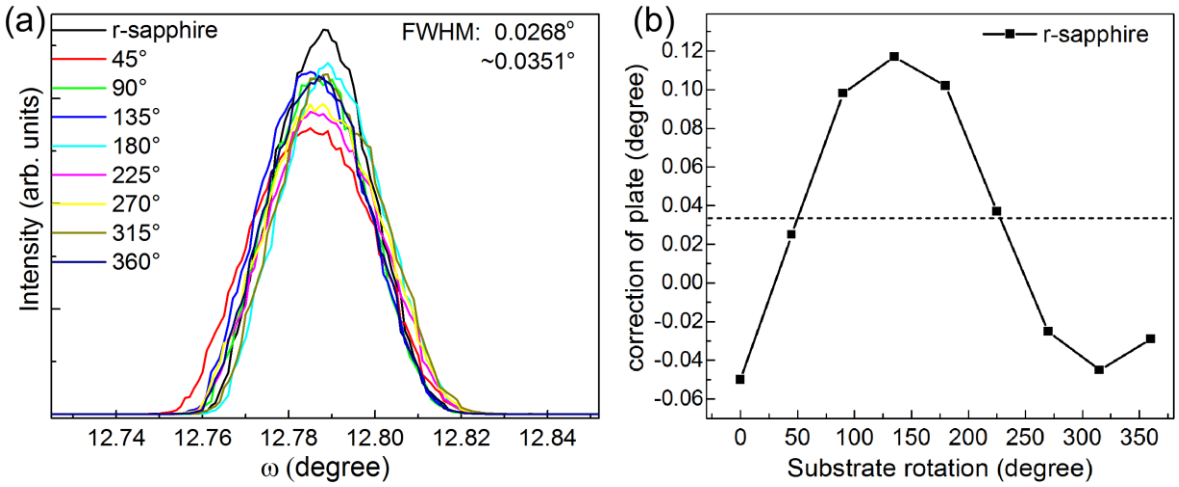

Fig. 7.2. (a) XRD rocking curves of Al_2O_3 ($10\bar{1}2$) reflection. (b) The corrected angle of the sample holder as a function of the substrate rotation.

7.2 Ultra-thin SnO_2 films on *r*-sapphire

An ultra-thin SnO_2 film was deposited on *r*-sapphire at a substrate temperature of 700 °C, with a precursor evaporation rate of Sn metal of 0.0017 g/h, and an O_2 gas flow rate of 4 sccm. The corresponding XRD θ-2θ scan is presented in Fig. 7.3. In the scan interval from 20° to 85°, apart from the ($10\bar{1}2$), ($20\bar{2}4$) and ($30\bar{3}6$) peaks of the *r*-plane sapphire, there are two additional peaks located at about 33.9° and 71.4°. These peaks are assigned to (101) and (202) reflections of SnO_2, respectively. No signs of secondary phases can be discerned in the pattern, indicating that the films grown on *r*-sapphire consist of pure-phase tetragonal rutile SnO_2 with an out-of-plane orientation of $SnO_2(101)\|Al_2O_3(10\bar{1}2)$. The inset of Fig. 7.3 depicts the rocking curve of the (101)-plane of this film. The out-of-plane FWHM is not as narrow as that of ultra-thin SnO_2 films on *c*-sapphire.

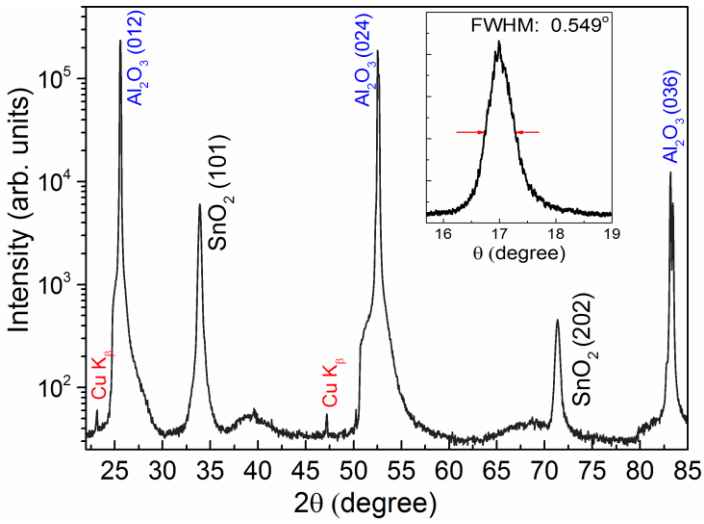

Fig. 7.3. XRD θ-2θ scan of an ultra-thin SnO_2 film on an *r*-sapphire substrate, which was deposited at a substrate temperature of 700 °C, with an evaporation rate of Sn metal of 0.0017 g/h, and an O_2 gas flow rate of 4 sccm. The inset depicts the rocking curve of the SnO_2 (101) reflection.

Fig. 7.4 shows the plane-view SEM image of this ultra-thin SnO_2 film. The surface consists of rectangular grains with grain sizes between 100 to 300 nm. The rectangular shape coincides with the rectangular SnO_2 and Al_2O_3 unit cells (Fig. 7.1). The film is evidently not closed.

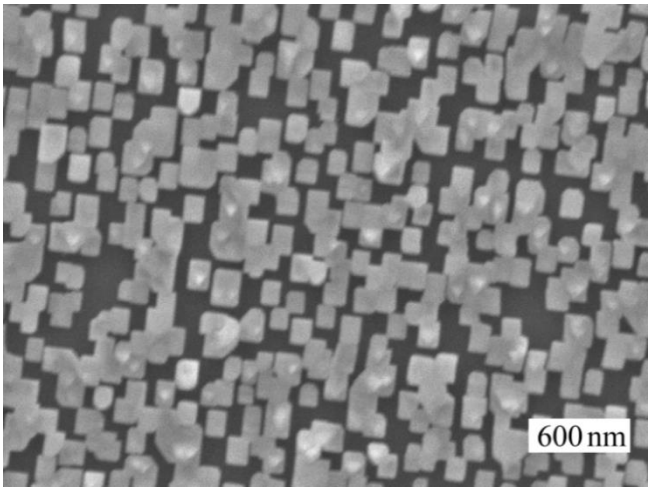

Fig. 7.4. Plane-view SEM image of the ultra-thin SnO_2 film.

Fig. 7.5 shows the optical transmittance of this ultra-thin SnO_2 film as a function of the incident light wavelength in the range of 200 - 1900 nm. The transmittance above the band gap (< 344 nm) of SnO_2 does not completely go down to 0. This is the case because the film is not closed (see Fig. 7.4).

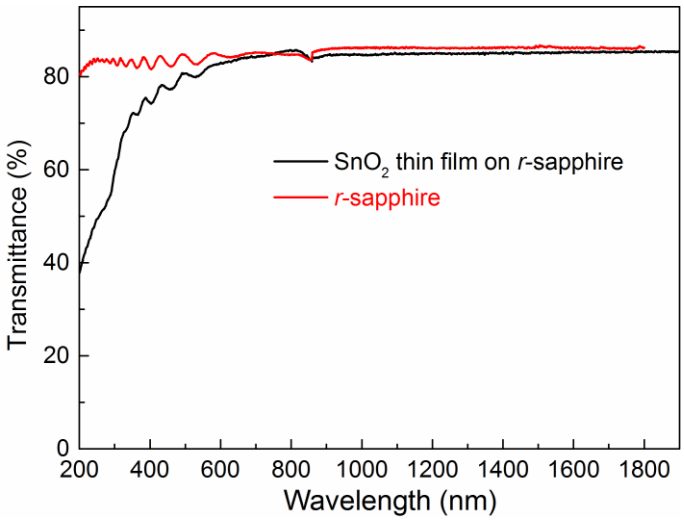

Fig. 7.5. The optical transmittance spectra of the ultra-thin SnO_2 film (black), and pure Al_2O_3 substrate (red), respectively.

7.3 The tilt in SnO_2 films on *r*-sapphire

In this section, we determine the tilt of the SnO_2 film, which occurs during the growth process of SnO_2 films on *r*-plane sapphire using XRD and SEM, and analyze the corresponding data in detail.

A film was deposited at a substrate temperature of 650 °C for 6.5 h yielding a film thickness of 1.35 µm. Fig. 7.6(a) and (b) show a XRD θ-2θ scan, and the rocking curve of the (200) reflection of the SnO_2 film on *r*-sapphire, respectively. Apart from the Al_2O_3 reflections, there are two additional peaks of SnO_2 (101) and (202) reflections located at 33.9° and 71.3°, respectively. The FWHM of the rocking curve of the (101) reflection of this film is 0.330°. The intensity of the SnO_2 reflections is lower than that of Al_2O_3 reflections.

In the rocking curve measurements it became evident that, when the SnO_2 (101) reflection became stronger by adjusting the sample table, the Al_2O_3 $(01\bar{1}2)$ reflection became very weak, or even disappeared. As an example, Fig. 7.6(c) shows θ-2θ scans of the sample before and after the adjusting the initial angle position of the sample table. The peak of SnO_2 (101) reflection in the red curve is about 100 times stronger than that before the adjustment of the sample table (see the black curve), but the peaks of *r*-sapphire in the red curve disappear due to the adjustment. This finding indicates that the SnO_2 (101)-plane is not completely parallel to the Al_2O_3 $(01\bar{1}2)$-plane, i.e. a tilt between them exists.

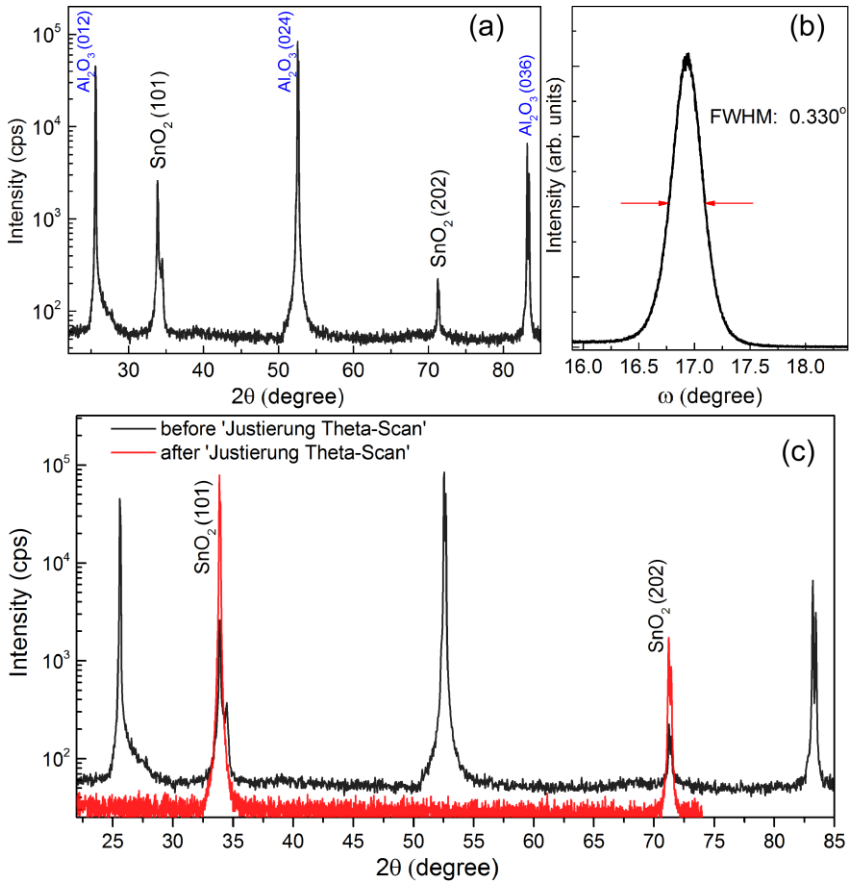

Fig. 7.6. (a) XRD θ-2θ scan of an SnO_2 film deposited at a substrate temperature of 650 °C for 6.5 h yielding a thickness of 1.35 µm, and (b) rocking curve at SnO_2 (200) reflection of this film. (c) Comparison of the XRD θ-2θ scans of this film before and after 'Justierung Theta-Scan'.

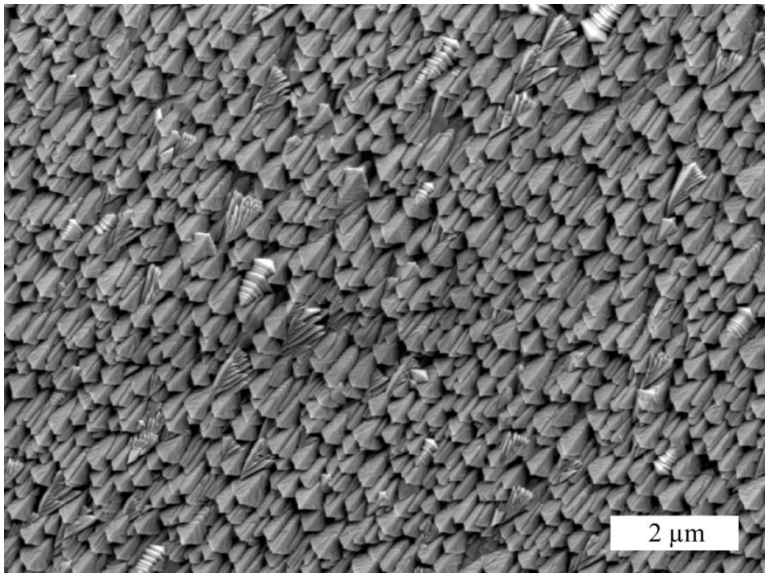

Fig. 7.7. Plane-view SEM image of the SnO_2 film on *r*-sapphire, whose XRD results are shown in Fig. 7.6.

Fig. 7.7 shows a plane-view SEM image of this film. The bird-feather-shaped crystalline grains have grain sizes between 200 and 500 nm. The feather-tips of the grains exhibit a preferential orientation. This image also visualizes the tilt between the facets of the grains and the substrate.

In section 6.1 we discussed how to measure the miscut polar angle θ of the substrate. Here we use the same method to determine the tilt between the SnO_2 (101)-plane and the *r*-sapphire substrate plane. Again a series of the rocking curves was measured where the sample was rotated by steps of 45° along the substrate normal. The series of curves obtained is shown in Fig. 7.8(a). The position of the peak maximum of the ω-scans varies with the rotation angle of the sample. The angle difference between SnO_2 (101)-plane and the sample holder plane as a function of rotation angle about the substrate normal is depicted in Fig. 7.8(b). The variation of the angle between the SnO_2 (101)-plane and the sample holder plane reveals a sine form. The tilt of the SnO_2 (101) plane of this film is about 1.0° with respect to the substrate surface, i.e. the Al_2O_3 $(10\bar{1}2)$-plane. As discussed in section 7.1, the miscut polar angle of *r*-sapphire is about 0.083°. The tilt of the SnO_2 film on *r*-sapphire is not caused by the miscut of the substrate.

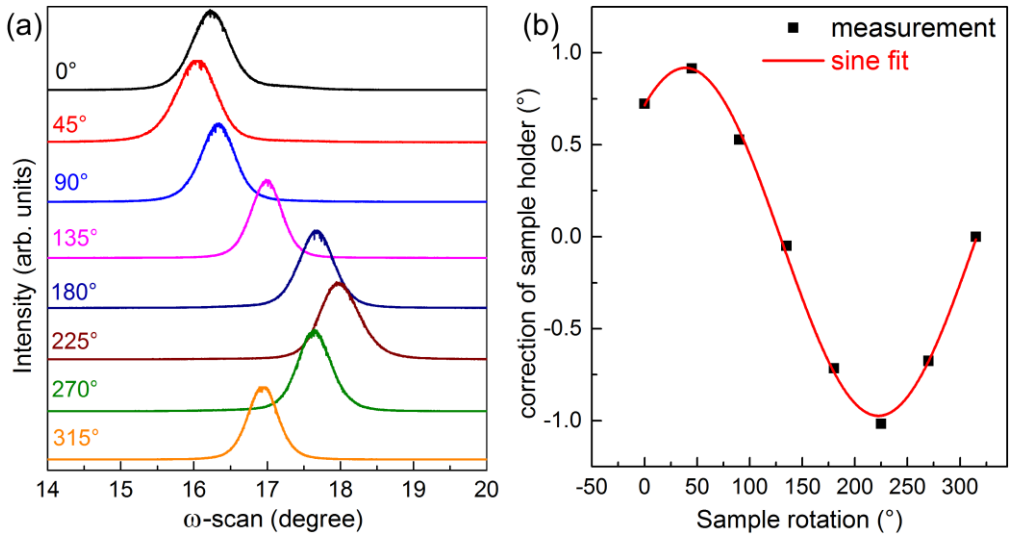

Fig. 7.8. (a) XRD rocking curves of SnO_2 (101) reflection for different rotation angles about the substrate normal axis. (b) The angle difference between the sample holder plane and the SnO_2 (101)-plane as a function of rotation angle.

Fig. 7.9(a) shows XRD θ-2θ scan of an SnO_2 film deposited at a lower substrate temperature of 550 °C for 6 h with a film thickness of 970 nm. The diffraction peaks of the film can be identified as reflections of the (101) crystal planes of SnO_2. Due to the logarithmic scale for the XRD intensity, SnO_2 (200) and (321) reflections are also observed. However, the SnO_2 (101) plane is obviously the preferred orientation (more than 100 times

stronger in intensity than the (200) and (321) reflections), indicating that the SnO_2 (101) plane is to a good approximation parallel to the substrate Al_2O_3 ($10\bar{1}2$) surface plane.

The X-ray rocking curve of the SnO_2 (101) reflection is plotted in Fig. 7.9(b). It exhibits a double peak structure where the intensity of the peak at lower angle is stronger than that of the other. The data of the rocking curve are fitted by two Gaussian functions in order to separate the two peaks. The FWHMs of the two peaks are 0.793° and 1.092°.

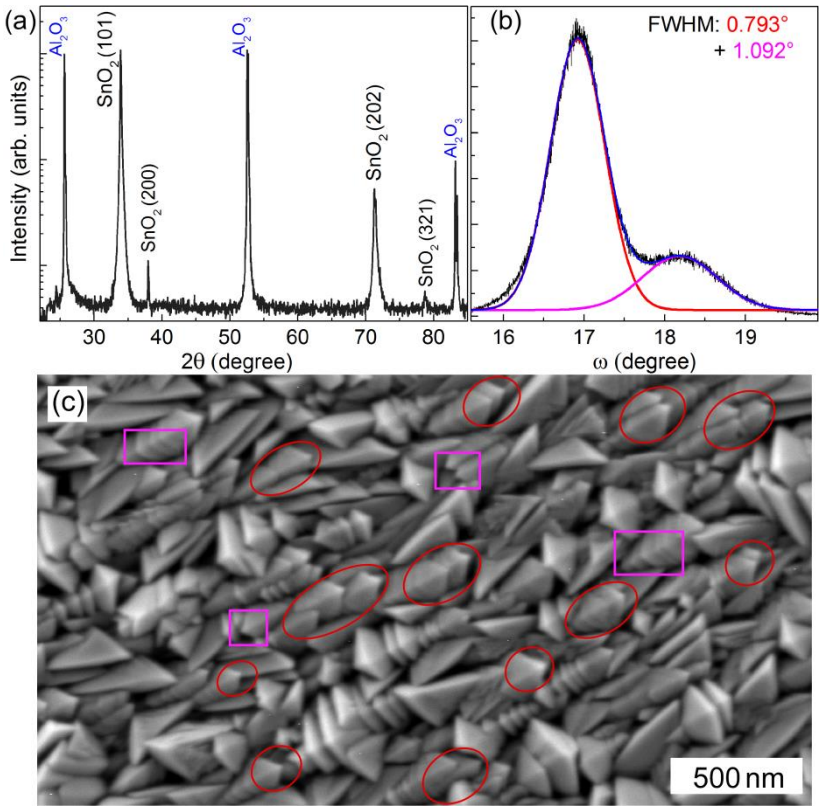

Fig. 7.9. (a) XRD θ-2θ scan of a film deposited at a substrate temperature of 550 °C for 6 h with a thickness of 970 nm, and (b) rocking curve at SnO_2 (101) reflection of this film. (c) The plane-view SEM micrograph of this SnO_2 film.

The plane-view SEM micrograph of this film is shown in Fig. 7.9(c). The bird-feather-shaped crystalline grains are also observed as for the film grown at 650 °C (cf. Fig. 7.7). However, their preferential orientation is less pronounced, i.e. there are also grains of other shapes, whose facets can be attributed to the other SnO_2 planes. This is consistent with the results of the θ-2θ scan in Fig. 7.9(a). The feather-tips in the SEM image are not all pointing towards one direction, some also point in the opposite direction. The orientation of the feather-tips in circles is directed towards the upper right of the image, whereas that of the tips in the squares is directed towards the bottom left of the image. There are much more crystalline grains pointing to the upper right than to the bottom left. This is in good agreement on the intensity distribution in Fig. 7.9(b).

Fig. 7.10(a) shows the θ-2θ scan of a film, deposited at an intermediate substrate temperature of 600 °C for 3 h yielding a thickness of about 1 µm. The SnO_2 (101) and (202) reflections are still preferential, but the other orientations (200), (110), and (321) become more pronounced compared with the samples, whose XRD-results are shown in Fig. 7.6 and Fig. 7.9. The X-ray rocking curve of SnO_2 (101) reflection is shown in Fig. 7.10(b). The peaks of the double-peak structure possess almost similar intensity. The FWHMs are 1.049° and 1.288°.

Fig. 7.10(c) shows the plane-view SEM micrograph of this film. The bird-feather-shaped crystalline grains are clearly pointing towards two opposite directions. In the SEM image circled tips pointing in the one direction are almost as many as tips enclosed by rectangles pointing in the other direction. This is consistent with the behavior of the two distributions of rocking curve in Fig. 7.10(b). The stone-shaped crystalline grains, which give rise to the reflections of other SnO_2 planes such as (200), (110), and (321), are much more than in the other two samples (cf. Fig. 7.7Fig. 7.9c). This is in agreement with the results of the XRD θ-2θ scan of this sample.

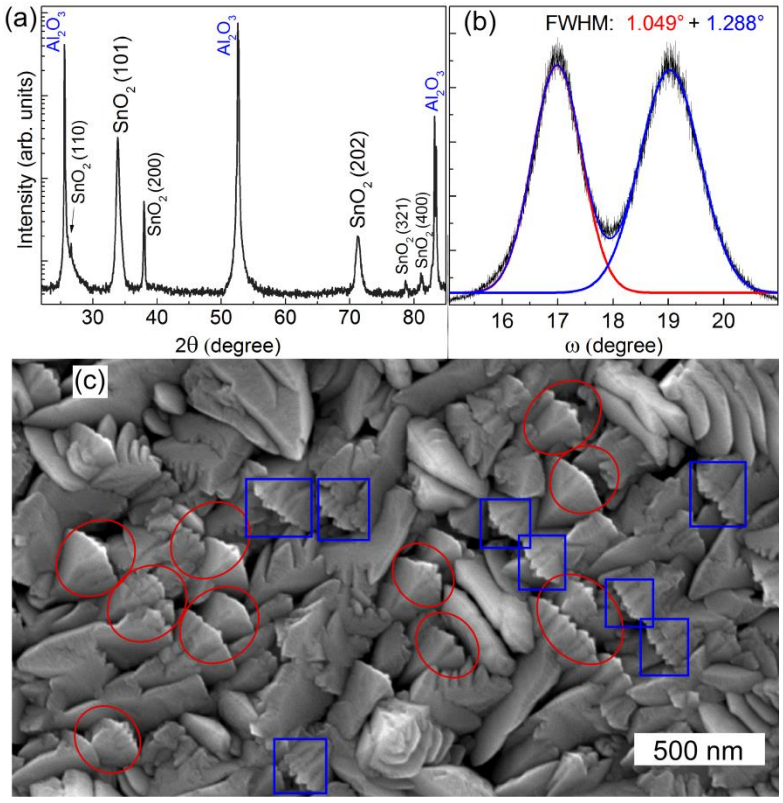

Fig. 7.10. (a) XRD θ-2θ scan of a SnO_2 film deposited at a substrate temperature of 600 °C for 3 h with thickness of about 1 µm, (b) rocking curve at SnO_2 (200) reflection of this film. (c) The plane-view SEM micrograph of this SnO_2 film.

The corresponding series of ω rocking curves is presented in Fig. 7.11(a) for the film deposited at 600 °C for 3 h. At angles of rotation along the substrate normal of 135° and 315° there is only a single rocking curve peak. This indicates that the scattering plane (defined by incident and diffracted wave vectors) is parallel to the direction, in which the feather-tips are pointing. We plot the variations of the angles of the slight narrow (black) and the wide (red) rocking curve peaks between the SnO_2 (101)-plane and the sample holder plane in Fig. 7.11(b), respectively. The tilt of the crystalline grains is about 2° to the substrate surface. However, in section 7.1 the miscut polar angle of *r*-sapphire substrate was estimated to only about 0.083°. This result indicates that the miscut of *r*-sapphire is not the main reason to give rise to the tilt of the SnO_2 (101) plane on *r*-sapphire. Pan *et al.* reported also that a misorientation exists in SnO_2 thin films on *r*-plane sapphire [1]. The formation reason of the tilt in the films etc. needs to be clarified in the further work.

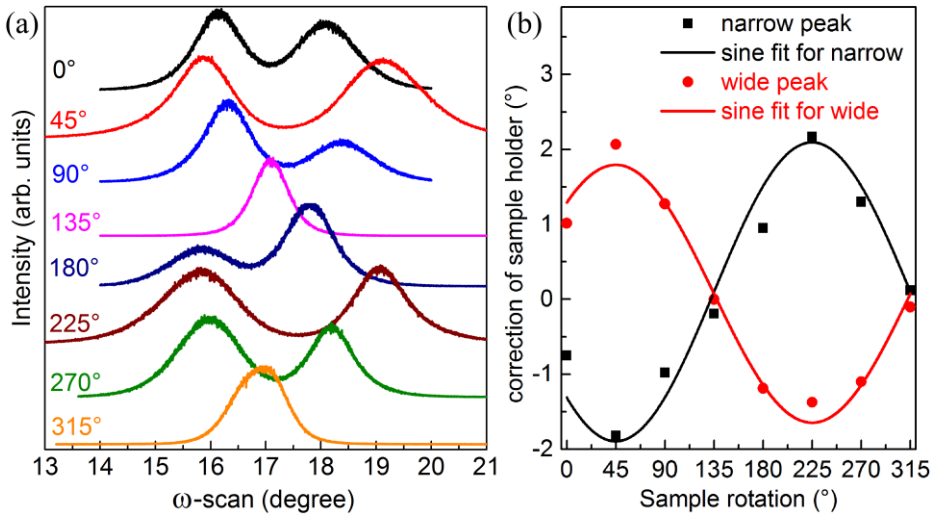

Fig. 7.11. (a) XRD rocking curves of SnO_2 (101) reflection at the different rotation angles of the sample about the substrate normal for the SnO_2 film grown at 600 °C. (b) Extracted angle between the sample holder plane and the SnO_2 (101)-plane from the two peaks of the rocking curves. The black rectangles and red spots become from the experimental values of the little narrow and fat peak in ω-scan, respectively. The lines are the sine fitted curves.

7.4 Lattice parameters of SnO_2 films

In order to investigate the lattice parameters of SnO_2 films on *r*-sapphire, ϕ-scans of selected samples were obtained. Fig. 7.12(a) presents the ϕ-scans of an SnO_2 film with a thickness of 1.35 µm recorded at SnO_2 {110}, Al_2O_3 {0006}, SnO_2 {200}, and Al_2O_3 $\{11\bar{2}3\}$ reflections. Its XRD results and SEM image are shown in Fig. 7.6 and Fig.

7.7, respectively. According to the results of the ϕ-scans, the in-plane orientation relationships are SnO_2 [010]∥Al_2O_3 <10$\bar{1}$0> and SnO_2 [10$\bar{1}$]∥Al_2O_3 <0$\bar{1}$11>. These results agree well with the diagram illustrated in Fig. 7.1 and also with other studies of SnO_2 films grown by MBE [2, 3], femtosecond pulsed laser ablation [1], pulsed-electron-beam deposition [4], sputtering [5], ALD and CVD [6, 7] etc. Well-separated reflections in the ϕ-scans demonstrate a good in-plane and out-of-plane orderings of the SnO_2 film, and reveal an epitaxial growth of SnO_2 film on *r*-sapphire. Fig. 7.12(b) shows the narrow θ-2θ scans of SnO_2 (101)-, (110)-, and (200)-planes, whose 2θ values are 33.93°, 26.57°, and 37.92°, respectively. Using the 2θ values of the SnO_2 (101)-, (110)-, and (200)-planes the lattice parameters of this SnO_2 film are estimated using crystal geometry equation (4.3) in Chapter 4. The lattice parameters *a* (out-of-plane), *b* (in-plane) and *c* (in-plane) derived for this SnO_2 film on *r*-sapphire are 4.74 Å, 4.74 Å, and 3.18 Å, respectively. They are in perfect agreement with the bulk lattice parameters of SnO_2 (4.738 Å, 4.738 Å, and 3.187 Å). These results reveal that the film is relaxed, as the film thickness reaches 1.35 µm. It should be noted that in the most SnO_2 films on *c*-sapphire with a thickness of about 1 µm strain was still present (see in chapter 6, Fig. 6.8).

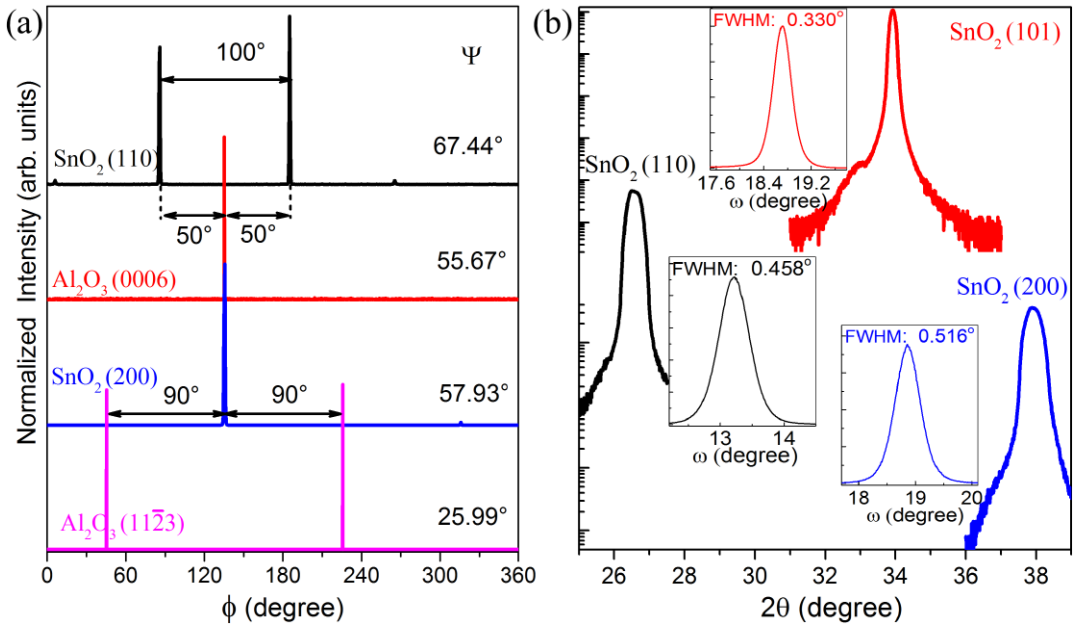

Fig. 7.12. (a) Multiple off-axis ϕ-scans of the SnO_2 film on r-sapphire grown at 650 °C. The diffraction peak and inclination angle (ψ) are indicated for each measurement. (b) The narrow θ-2θ scans of the SnO_2 (101)-, (110)-, and (200)-planes, which 2θ values are 33.93°, 26.57°, and 37.92°, respectively. The corresponding rocking curves using same color are depicted in the insets.

In Fig. 7.12(b) the peak of the θ-2θ scan of SnO_2 (101) reflection is sharper than those of the other two peaks of (110) and (200) reflections. FWHM and position of the Bragg peak can be used to determine the crystallite size *D* by the Scherrer method. While the crystallite size is associated with the coherent crystal length and is deduced from θ-2θ scans by using the Scherrer equation (4.2). The Scherrer coherence lengths of 49 nm, 19 nm, and 17 nm are determined for this film along the direction of the scattering vector of SnO_2 (101)-, (110)-, and (200)-planes, respectively. The Scherrer coherence lengths are obviously smaller than the grain sizes, which are observed in SEM image of this film (Fig. 7.7). This reason can be found in Ref. [8]. The results suggest that the out-of-plane Scherrer coherence length is larger than the in-plane coherence length. The insets of Fig. 7.12(b) depict rocking curves of the SnO_2 (101)-, (110)-, and (200)-planes with ω-scan FWHM values of 0.330°, 0.458°, and 0.516°, respectively, These values show that the in-plane ordering is better than the out-of-plane ordering of this film.

7.5 Conclusions

Epitaxial SnO_2 (101) films were grown on *r*-sapphire by CVD. XRD analysis shows that pure-phase SnO_2 films with a rutile structure were obtained. SEM reveals that the initial SnO_2 film possesses rectangular shape, which coincides with the rectangular unit cells of SnO_2 (101)- and $Al_2O_3(10\bar{1}2)$-plane. The epitaxial relationships between the SnO_2 films and the substrates are $SnO_2(101) \parallel Al_2O_3(10\bar{1}2)$ in the out-of-plane orientation, and $SnO_2[010] \parallel Al_2O_3\langle 100\rangle$ and $SnO_2[10\bar{1}] \parallel Al_2O_3\langle \bar{1}\bar{2}1\rangle$ in the in-plane orientation. Detailed analysis using XRD indicates that a tilt exists between the SnO_2 films and the *r*-sapphire substrates. The misoriented angle of the films is about 1° ~ 2°. It is obviously bigger than the miscut polar angle of the *r*-sapphire substrate.

References

[1] J.E. Dominguez, L. Fu, X.Q. Pan, *Effect of crystal defects on the electrical properties in epitaxial tin dioxide thin films*, Appl. Phys. Lett., 81 (2002) 5168-5170.

[2] M. Batzill, J.M. Burst, U. Diebold, *Pure and cobalt-doped SnO_2(101) films grown by molecular beam epitaxy on Al_2O_3*, Thin Solid Films, 484 (2005) 132-139.

[3] M.E. White, M.Y. Tsai, F. Wu, J.S. Speck, *Plasma-assisted molecular beam epitaxy and characterization of SnO_2 (101) on r-plane sapphire*, J. Vac. Sci. Technol. A, 26 (2008) 1300-1307.

[4] R.J. Choudhary, S.B. Ogale, S.R. Shinde, V.N. Kulkarni, T. Venkatesan, K.S. Harshavardhan, M. Strikovski, B. Hannoyer, *Pulsed-electron-beam deposition of transparent conducting SnO_2 films and study of their properties*, Appl. Phys. Lett., 84 (2004) 1483-1485.
[5] Y.H. Choi, S.H. Hong, *H_2 sensing properties in highly oriented SnO_2 thin films*, Sensors and Actuators B: Chemical, 125 (2007) 504-509.
[6] A. Tarre, A. Rosental, A. Aidla, J. Aarik, J. Sundqvist, A. Hårsta, *New routes to SnO_2 heteroepitaxy*, Vacuum, 67 (2002) 571-575.
[7] J. Sundqvist, J. Lu, M. Ottosson, A. Hårsta, *Growth of SnO_2 thin films by atomic layer deposition and chemical vapour deposition: A comparative study*, Thin Solid Films, 514 (2006) 63-68.
[8] D. Balzar, *Voigt-function model in diffraction line-broadening analysis*, Oxford, 1999.

8 SnO_2 films grown at high temperature

Due to the large lattice mismatch between SnO_2 and sapphire, it is difficult to obtain high quality thick SnO_2 films on sapphire substrates. Mostly if the thickness of SnO_2 films is above 1 µm on sapphire, the SnO_2 samples are opaque (with a whitish milky appearance). Here we demonstrate that transparent SnO_2 films with thicknesses above 3 µm can be obtained by CVD at a substrate temperature of 900 °C. Such samples were grown on *c*- and *r*-plane sapphire as well as on quartz glass. Only the SnO_2 film with a thickness of 8 µm on quartz glass grown at high substrate temperature is opaque, all others are transparent. The films deposited were characterized using XRD, HRXRD, SEM, AFM, Raman, PL, and optical transmittance.

8.1 Deposition conditions of SnO_2 films at high temperature

The detailed description of the experimental procedure is given in chapter 3. The deposition conditions and some results for the films deposited at high substrate temperature are listed in Table 8.1).

Table 8.1. Deposition conditions of SnO_2 films grown at high temperature.

Precursor	SnI_2, O_2
Substrate	*c*-, *r*-plane sapphire, and quartz glass
Substrate temperature	900 °C
Reactor pressure	30 mbar
Evaporation rate of SnI_2	0.7 g/h
Oxygen flow rate	40 sccm
Growth time	2 h
Film thickness	3.5 µm (on *c*-sapphire), 4.75 µm, 3.6 µm (on *r*-sapphire), ~8 µm (on quartz glass)

8.2 Structure of the SnO_2 films

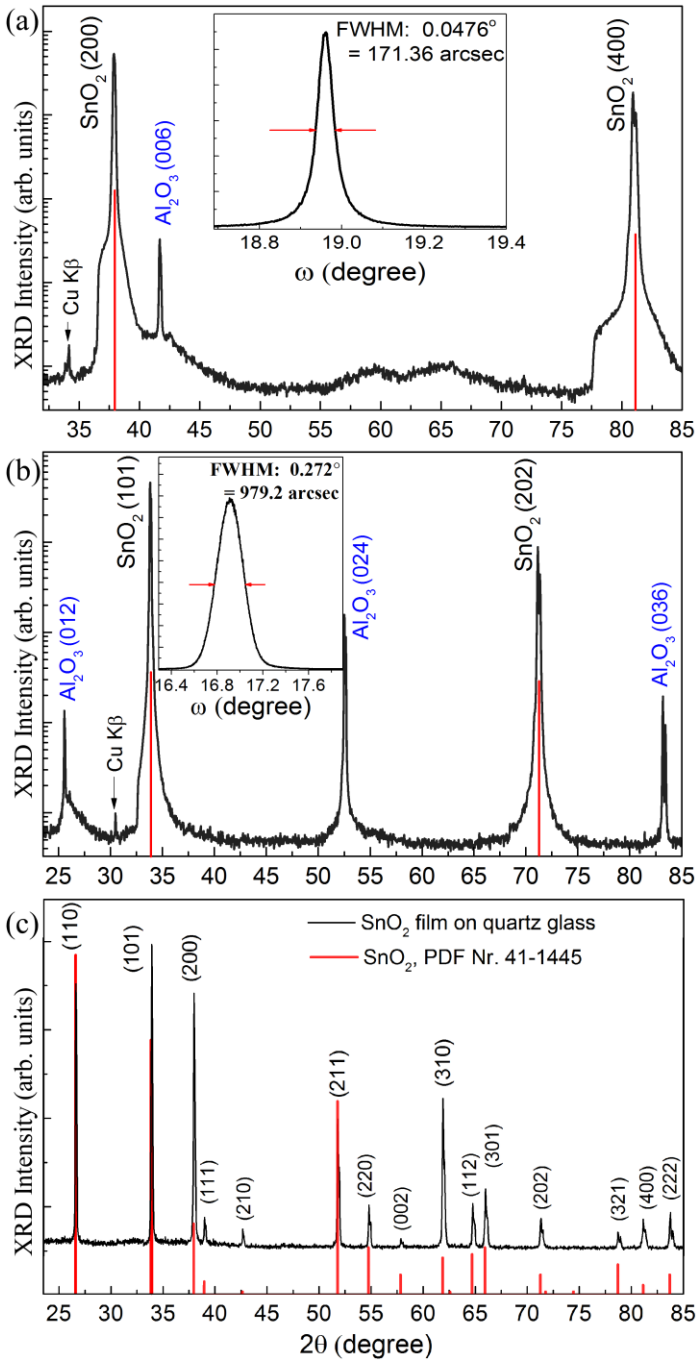

Fig. 8.1. XRD θ-2θ scans of SnO_2 films deposited at a high substrate temperature of 900 °C, (a) on *c*-sapphire with a thickness of 3.5 µm, the inset is the ω-scan of the SnO_2 (200) reflection; (b) on *r*-sapphire with a thickness of 4.7 µm, the inset is the ω-scan of the SnO_2 (101) reflection; and (c) on quartz glass with a thickness of ~8 µm. The red lines show the standard powder diffraction spectrum of SnO_2 (ICDD PDF #41-1445) for comparison.

Fig. 8.1 shows the XRD θ-2θ scans of the SnO_2 films grown in the same growth run at a high substrate temperature of 900 °C on the three different kinds of substrate. The scans cover a 2θ range from 20° to 85°. Apart from the sharp reflections of the sapphire substrates, there are only reflections of rutile SnO_2 based on ICDD PDF No. 41-1445. The red lines show the standard powder diffraction spectrum of SnO_2 for comparison.

Fig. 8.1(a) indicates that a pure-phase tetragonal rutile SnO_2 film is obtained on *c*-sapphire with an out-of-plane orientation relationship of $SnO_2(100)\|Al_2O_3(0001)$. The inset shows the rocking curve of the (200) reflection of the SnO_2 film. The FWHM of the rocking curve is only 0.0476° (using the 2-circle XRD at IPI, Uni. Giessen) indicating the high degree of out-of-plane ordering of this film. Fig. 8.1(b) shows the out-of-plane orientation relationship of $SnO_2(101)\|Al_2O_3(01\bar{1}2)$ of the SnO_2 film on *r*-sapphire. The FWHM of the rocking curve of the SnO_2 (101) reflection is 0.272°. Compared with other SnO_2 films on *r*-sapphire grown at low temperature this film with a thickness of 4.7 µm possesses a very good out-of-plane ordering. Fig. 8.1(c) indicates that the SnO_2 film on quartz glass is polycrystalline as expected. The strong reflections in this film are the following: (101), (110), (200), (310), and (211).

The analysis of the rocking curve measurements for the two SnO_2 films on *r*-sapphire grown at high temperature indicates that the tilt in these films is very small, namely about 0.1°. This value is comparable with the miscut polar angle of the substrate of 0.083°. A tilt of the SnO_2 film with respect to the *r*-sapphire is absent in this case.

Fig. 8.2 shows the 4-circle HRXRD ϕ-scans and narrow θ-2θ scans of the SnO_2 film with a thickness of 3.5 µm on *c*-sapphire grown at high temperature. The ϕ-scans of the {110}- and {101}-planes of the SnO_2 film both exhibit a six-fold symmetry along the [100] rotation axis, indicating that the 120° rotation of the domains in this film exists. The inhomogeneous intensity of the peaks is caused by the irregular shape of the small sample (rectangular, about 12×7 mm^2). It does not indicate that the domains along one direction grow preferentially compared with the domains along the other two directions. In Fig. 8.2(b) the peak of (200) reflection is located at 37.86°, very close to the value of 37.95° for bulk SnO_2. The FWHM of the very sharp peak of (200) reflection in the θ-2θ scan is 0.0265°. Using the Scherrer equation (4.2), the coherent crystal length along [200] direction is deduced to 317 nm. To the best of our knowledge, this is the largest coherent crystal length found for SnO_2 films with thicknesses of more than 1 µm on sapphire. The large coherent length of this film reveals the length scale of the perfect structure along the growth direction. However, the peak of the (110) and (101) reflections are very wide, and possess even double peak structures indicating that the in-plane ordering is less good.

The FWHMs of the rocking curves of the film are also different (the insets in Fig. 8.2b). The out-of-plane value is only 0.039° (actually, it is comparable to the value of

0.0476° measured using 2-circle XRD in Fig. 8.1a), indicating an excellent ordering of this film in the out-of-plane direction. Whereas the FWHMs of the rocking curve of the (110) and (101) reflection are 1.6° and 0.77°, respectively. The results reveal the strong anisotropic growth of the SnO_2 film on *c*-sapphire even at high substrate temperature. The reasons are not only the large lattice mismatch between SnO_2 and Al_2O_3, but also the different symmetry between the SnO_2 (200)-plane and Al_2O_3 (0001)-plane, i.e. rutile versus hexagonal structure. The findings are in agreement with the results of Rue *et al.* that the heteroepitaxial growth with a large mismatch between a film and a substrate is oriented well in the out-of-plane direction, but that the degree of in-plane epitaxy is low [1].

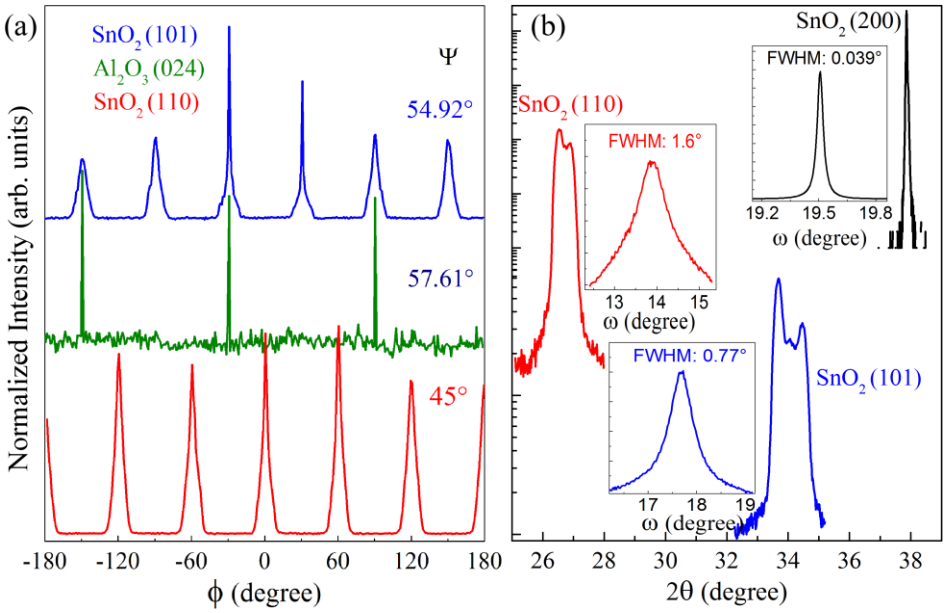

Fig. 8.2. (a) Multiple off-axis ϕ-scans of the SnO_2 film on *c*-sapphire with a thickness of 3.5 µm grown at 900 °C. The diffraction peak and inclination angle (ψ) are indicated for each measurement. (b) The narrow θ-2θ scans of the SnO_2 (200)-, (110)-, and (101)-planes, and the corresponding rocking curves shown in the insets.

Fig. 8.3 presents the HRXRD ϕ-scans and narrow θ-2θ scans of the SnO_2 film with a thickness of 3.6 µm on *r*-sapphire grown at high temperature as comparison. The well-separated reflections of ϕ-scans in Fig. 8.3(a), and the much smaller FWHMs rocking curve of (110) and (200) reflections of the film on *r*-sapphire compared with the FWHMs rocking curve of (101) and (110) reflections of the film on *c*-sapphire demonstrate a much better in-plane ordering of the SnO_2 film on *r*-sapphire than on *c*-sapphire. The detailed discussion for the SnO_2 film grown on *r*-sapphire at 650 °C can be found in chapter 7 (Fig. 7.12). A few details are worth noting. First, the inclination angles Ψ of (110)- and (200)-plane of this film are much closer to the calculated values (66.76° for (110)-, and 56.07° for (200)-plane) compared to the thinner sample in Fig. 7.12 grown at a temperature

of 650 °C. This result also indicates that the tilt of the film grown at high temperature is very small.

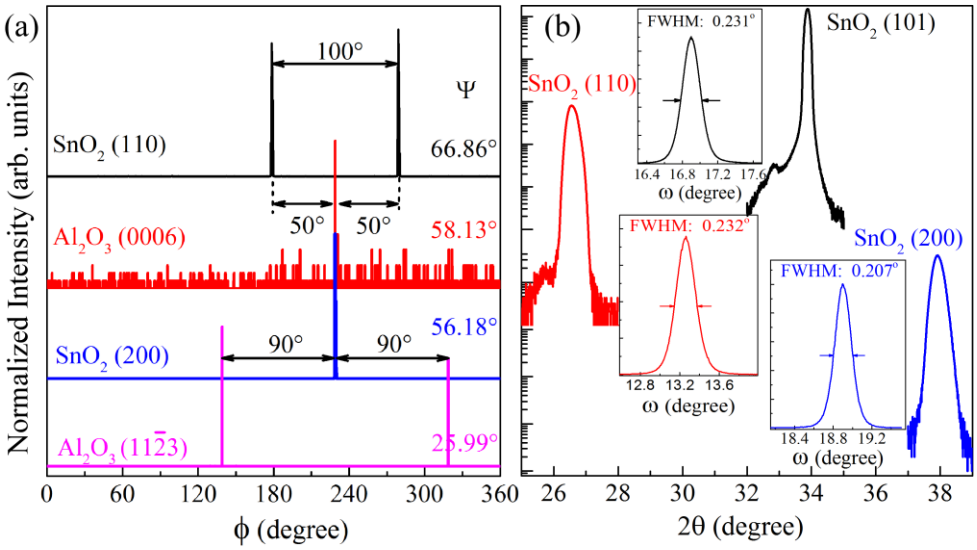

Fig. 8.3. (a) Multiple off-axis ϕ-scans of the SnO_2 film on *r*-sapphire with a thickness of 3.6 µm grown at 900 °C. The diffraction peak and inclination angle (ψ) are indicated for each measurement. (b) The narrow θ-2θ scans of the SnO_2 (101)-, (110)-, and (200)-planes, whose 2θ values are 33.89°, 26.58°, and 37.95°, respectively. The corresponding rocking curves are shown in the insets.

Second, in Fig. 8.3(b) the FWHMs of the rocking curves of this film are considerably smaller than those of the SnO_2 film in Fig. 7.12, i.e. with values of 0.231°, 0.232°, and 0.207° compared to 0.330°, 0.458°, and 0.516° for (101), (110), and (200) reflections, respectively. According to the Scherrer equation, the coherence lengths of this film are 53, 25, and 28 nm along the direction of the scattering vector of SnO_2 (101)-, (110)-, and (200)-planes, respectively. These coherence lengths are larger than those of the films grown at low temperatures (see section 5.4), which are 49, 19, and 17 nm, respectively. These findings prove that the in-plane and out-of-plane ordering of the films grown on *r*-sapphire at high temperature is better than that of films grown at low temperature.

8.3 Morphology of the SnO_2 films

The SEM images in Fig. 8.4 show plane-views of the surface of the SnO_2 film on *c*-sapphire with a thickness of 3.5 µm. Large circularly shaped crystal domains with sizes in the range of 30 to 40 µm are observed. Fig. 8.4(b) shows a magnified image of the top area of such a crystal domain. The top of the domains appears to be flat, and not to exhibit a grain structure but rather a terraced structure.

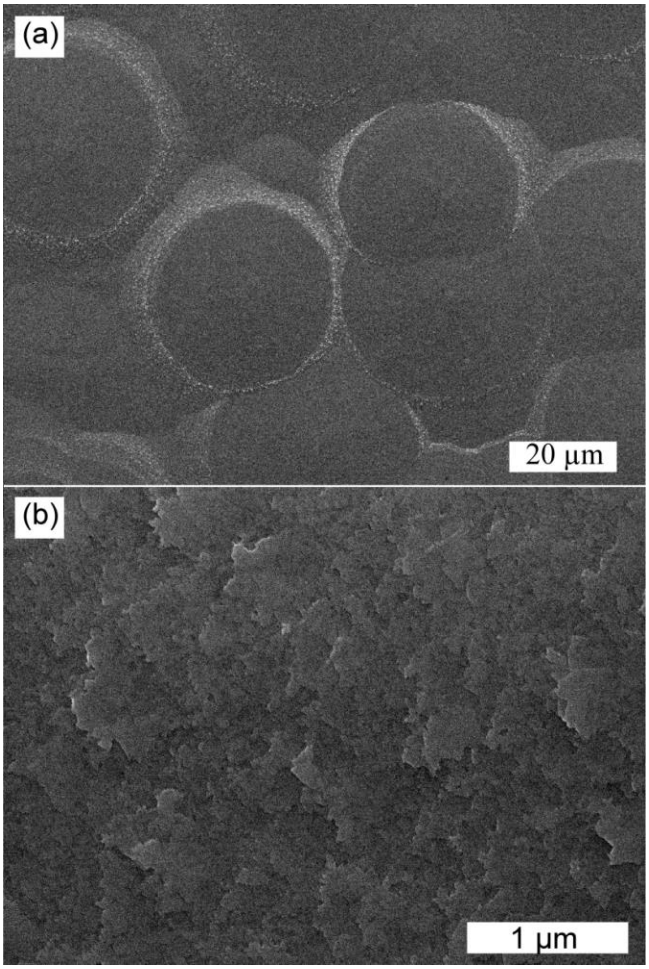

Fig. 8.4. The plane-views of the SEM images for the SnO_2 film on *c*-sapphire grown at high temperature.

Fig. 8.5 shows the cross-sectional morphology of the SnO_2 film on *c*-sapphire. According to this measurement the thickness of the film is about 3.7 µm, which is in good agreement with the value of 3.5 µm determined by optical transmittance measurements. The film is compact. The surface of the SnO_2 film looks homogeneous. However, it is worth noting, the initial growth of the film on *c*-sapphire is columnar. The region close to

the substrate surface, where columnar growth occurs, extends to a distance from the substrate of about 500 to 800 nm, after then the columns slowly disappear. No grains and grain boundaries can be observed in the SEM image.

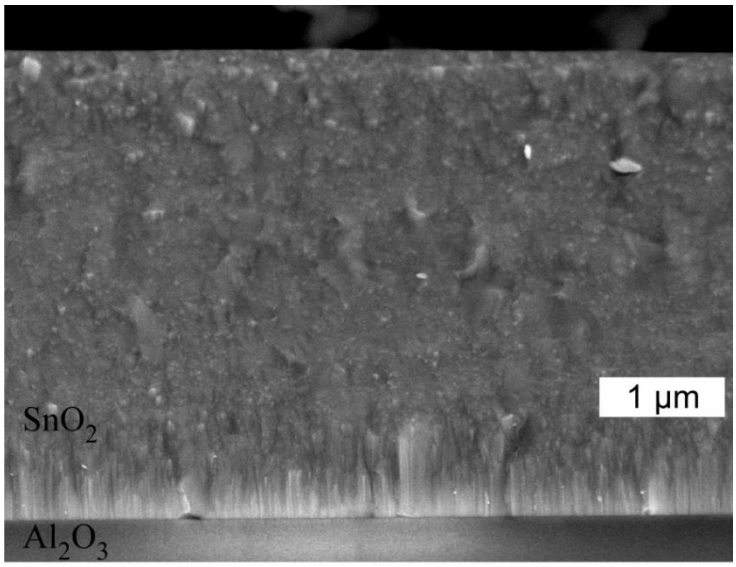

Fig. 8.5. Cross-sectional view of the SnO_2 film on *c*-sapphire. The thickness of this film is about 3.5 µm.

For comparison, Fig. 8.6 shows the plane-view SEM images of the surface of the SnO_2 film grown on *r*-sapphire with a thickness of 4.75 µm (the other film with the thickness of 3.6 µm exhibits a similar morphology). Again, the entire surface is flat, scarcely any grain is observed on the top surface, apart from some rectangular and pyramid shape domains which are implanted into the flat matrix (in Fig. 8.6a).

Fig. 8.6(b) shows such a rectangular domain, which can be regarded as arising from the rectangular structure of the SnO_2 unit cell on the *r*-sapphire surface. This rectangular domain size is more than 30 µm wide. Fig. 8.6(c-e) is a series of SEM images of the same pyramid shaped domain at different magnifications. From these gradually magnified images it becomes obvious that the pyramid shaped domain consists of rectangular shaped layers. However, one side of the pyramid grew more slowly, forming terraces on the edge. Fig. 8.6(f) shows a magnified image of the area enclosed by the small white rectangle in Fig. 8.6(c). The terraced structure of the surface is on the nanometer scale and can be clearly discerned.

Fig. 8.7 shows the cross-sectional morphology of the SnO_2 film on *r*-sapphire with a thickness of 4.7 µm. The film is very compact, no grain formation is observed. The surface of the SnO_2 film looks homogeneous. In contrast to the SnO_2 film on *c*-sapphire no interface region with columnar growth is observed indicating that *r*-sapphire is indeed the better substrate choice for growing epitaxial SnO_2 on sapphire.

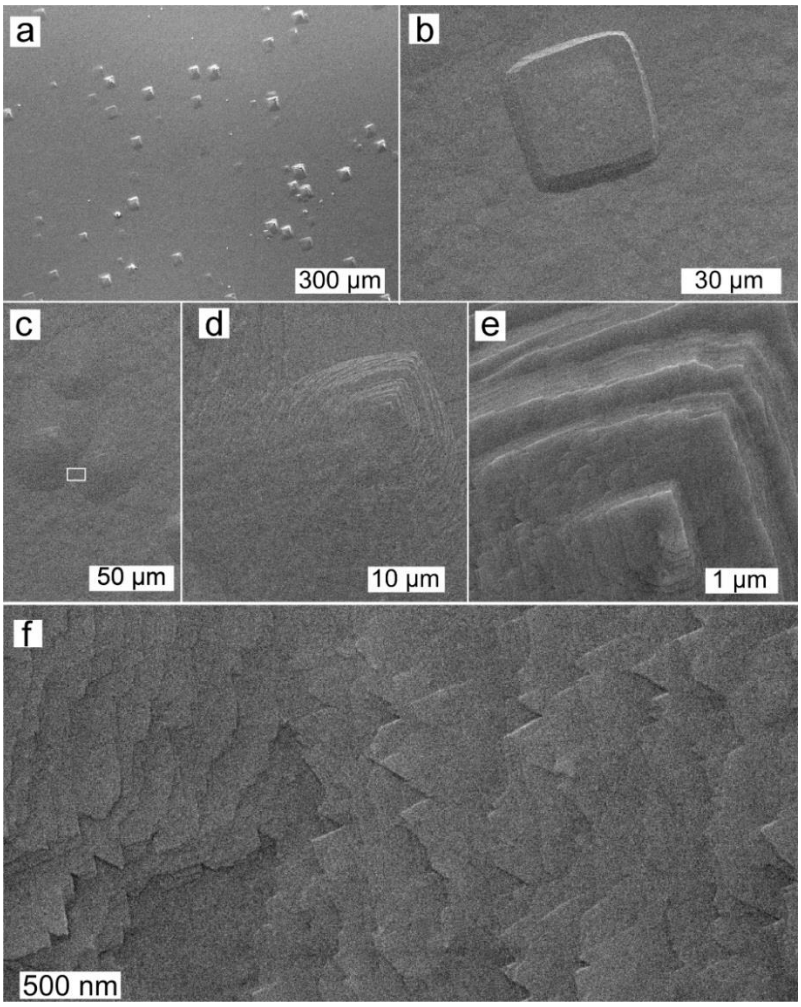

Fig. 8.6. The plan-views of the SEM images for the SnO_2 film on *r*-sapphire grown at high temperature.

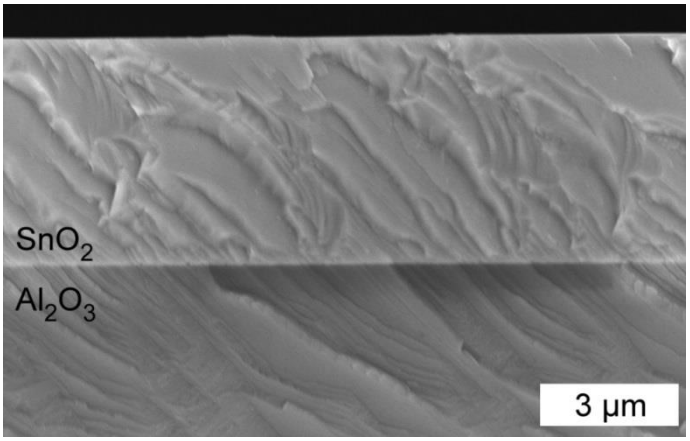

Fig. 8.7. Cross-sectional view of the SnO_2 film on *r*-sapphire. The thickness of this film is about 4.7 µm.

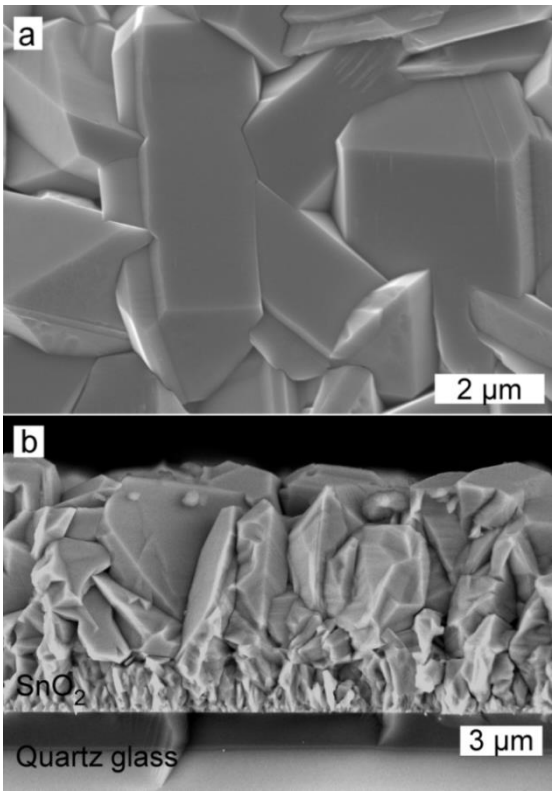

Fig. 8.8. The surface and cross-sectional views of the SnO_2 film on quartz glass.

For comparison, Fig. 8.8 shows the plan-view and cross-sectional morphologies of the SnO_2 film deposited on quartz glass with a thickness of about 8 µm. Large single crystals (monocrystalline) with sizes between 2 and 7 µm reveal well defined facets. These crystallites accumulate randomly and compactly, forming a mosaic-like arrangement. Near the interface, the SnO_2 grains are smaller, but the grains become much larger towards the top part of the film. The surface of this film is very rough compared with the SnO_2 films on *c*-sapphire (Fig. 8.4) and on *r*-sapphire (Fig. 8.6). It exhibits a roughness on the µm-scale rather than on the nm-scale.

AFM was used to further characterize the structural properties of the films grown at high temperatures. In Fig. 8.9 an AFM image and the corresponding line profile of a characteristic circular domain are displayed. The domain is circular with a diameter of about 40 µm. The line profile shows that the top area of the domain is cone-shaped with a cone height of about 0.4 µm, and not as flat as suggested by the SEM image of the surface. The root mean square (RMS) of the height fluctuation of this 50×50 μm^2 area is about 200 nm.

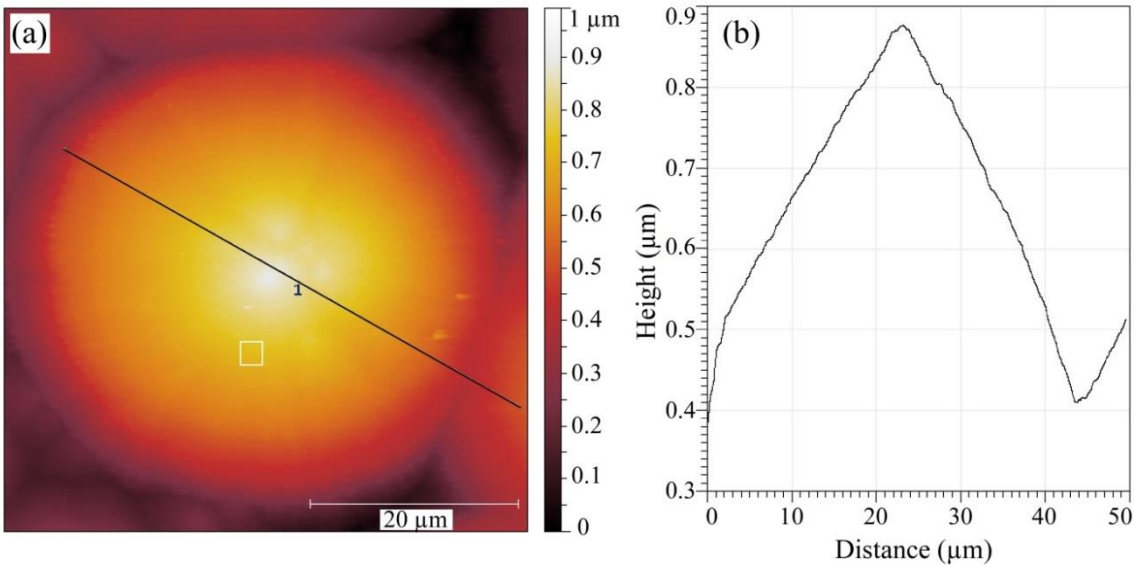

Fig. 8.9. (a) AFM image of the surface of the SnO_2 film on *c*-sapphire. (b) AFM line profile along the black line indicated in the left image.

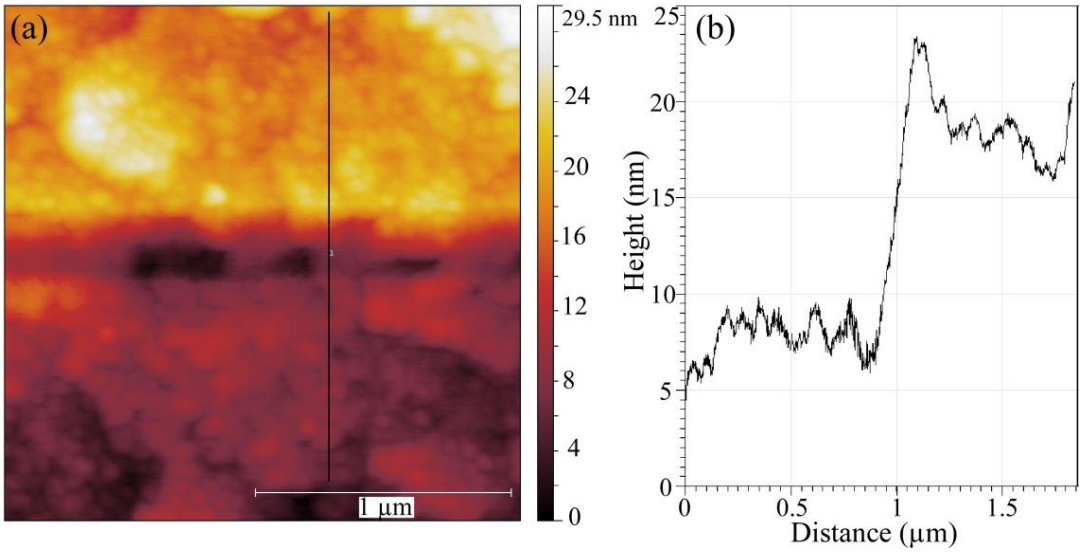

Fig. 8.10. (a) AFM image of the area enclosed by a small white rectangle in Fig. 8.9a. (b) AFM line profile along the vertical line indicated in the left image.

Fig. 8.10 shows a magnified image of the area enclosed by a small white square in Fig. 8.9(a). In this 2×2 μm^2 area there are 2 terraces. It is consistent with the result of the SEM study (see Fig. 8.4b). The line profile shows that the terrace height is only about 10 nm. The RMS of the height fluctuation of this area is 6 nm.

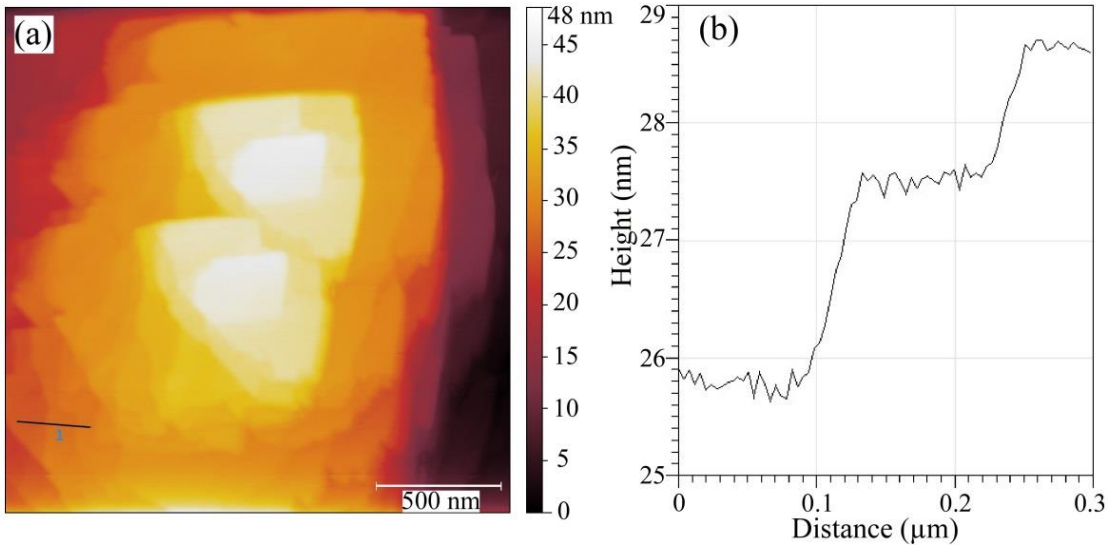

Fig. 8.11. (a) AFM image of the surface of the SnO_2 film on *r*-sapphire. (b) AFM line profile along the black line indicated on the bottom left of the left image.

The AFM micrograph of the SnO_2 film on *r*-sapphire is presented in Fig. 8.11 for a scanning area of 2×2 μm^2, the RMS of the roughness of this film is 10 nm. This value is of the same magnitude and only slightly larger than that of the SnO_2 (100) on *c*-sapphire (6 nm). In figure (a), the layered structure is clearly visible, supporting the observation made in Fig. 8.6(f). Fig. 8.11 shows the AFM line profile along the black line depicted on the bottom left of figure (a). It reveals that the height of the terraces is in the range of 1 to 2 nm, i.e. just the thickness of a few SnO_2 unit cells. These terraces are flat.

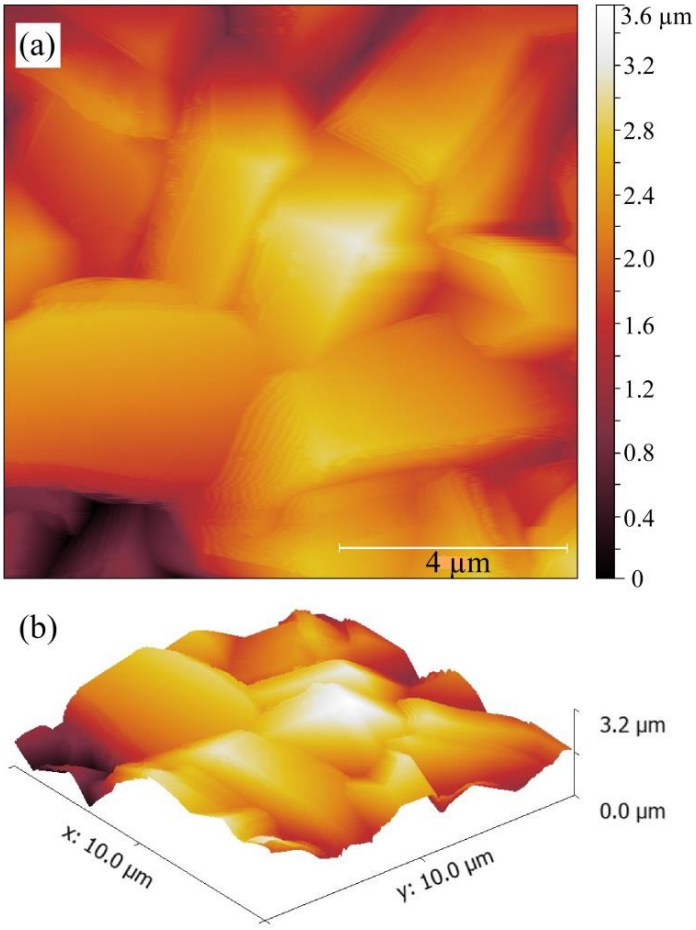

Fig. 8.12. 2D and 3D AFM images of the surface of the SnO_2 film on quartz glass for a scanning area of 10×10 µm^2.

In Fig. 8.12 the top-view (2D) and three-dimensional (3D) AFM images of SnO_2 film on quartz glass are presented for comparison. The typical grain sizes of the film are about 4 µm in length or width. The RMS of the height fluctuation in this scanning area of 10×10 µm^2 is 0.5 µm. This indicates that the surface of the SnO_2 film on quartz glass is very rough due to the random arrangement of the large faceted grains. The results are consistent with the cross-sectional SEM image of this film (see Fig. 8.8b).

8.4 Raman spectra

The Raman spectra of SnO_2 films grown on the three different substrates at high substrate temperatures are presented in Fig. 8.13. In graphs (a) and (b), the Raman spectra of the substrates are depicted for comparison. The three Raman-active phonon modes of E_g, A_{1g}, and B_{2g} symmetry character at about 476, 634, and 778 cm^{-1}, respectively, are observed in the spectra of the samples on *r*-sapphire and on quartz glass. In case of the SnO_2 film on *c*-sapphire the B_{2g} mode is absent. This finding is in accordance with the theoretical predictions summarized in table (4.1) and the experimental observations of the SnO_2 films grown at the low temperature of 510 °C discussed in section 6.2.5. The fourth Raman-active mode B_{1g} observed at the Raman shift of about 121 cm^{-1} by Peercy *et al.* [2] was also detected in our SnO_2 films (see the inset in Fig. 8.13c), but exhibits only a weak signal intensity. Katiyar *et al.* performed a careful search of this region using different excitation wavelengths and reported that this mode typically has an intensity a thousand times weaker than that of the A_{1g} mode [3].

Next to the Raman-active phonons, three additional features at about 497, 541, and 696 cm^{-1} are visible in the spectra in Fig. 8.13. Weak Raman bands at 497 and 695 cm^{-1} were also observed by Peng in the spectra of SnO_2 nanobelts synthesized from Sn and SiO_2 powders [4]. Abello *et al.* proposed that IR modes could become weakly activated due to structural disorder and suggested that the weak Raman bands at 497 and 695 cm^{-1} might correspond to the IR-active transverse optical (TO) and longitudinal optical phonons (LO) of A_{2u} symmetry character, respectively [5]. The weak Raman band at 541 cm^{-1} was also observed by Dieguez *et al*. in the Raman spectrum of nanometric SnO_2 particles [6]. They proposed that the appearance of the signal at about 541 cm^{-1} was a consequence of the disorder activation. Structural disorder is for example induced by intrinsic or extrinsic point defects that break the perfect translational symmetry of the ideal crystal structure. As a consequence, the Raman selection rules may be modified such that normally Raman forbidden lattice vibrations, e.g. infrared active modes or silent modes, become Raman active. Alternatively, the additional features might originate from second or higher order scattering processes. For example, the broad signal at about 497 cm^{-1} might be caused by the difference mode $E_u^{(3)}(LO) - E_u^{(1)}(LO)$ or the overtone process $2E_u^{(1)}$. Further experiments are required to clarify their origin unambiguously. (The values of modes $E_u^{(x)}$ can be found in Ref. [7].)

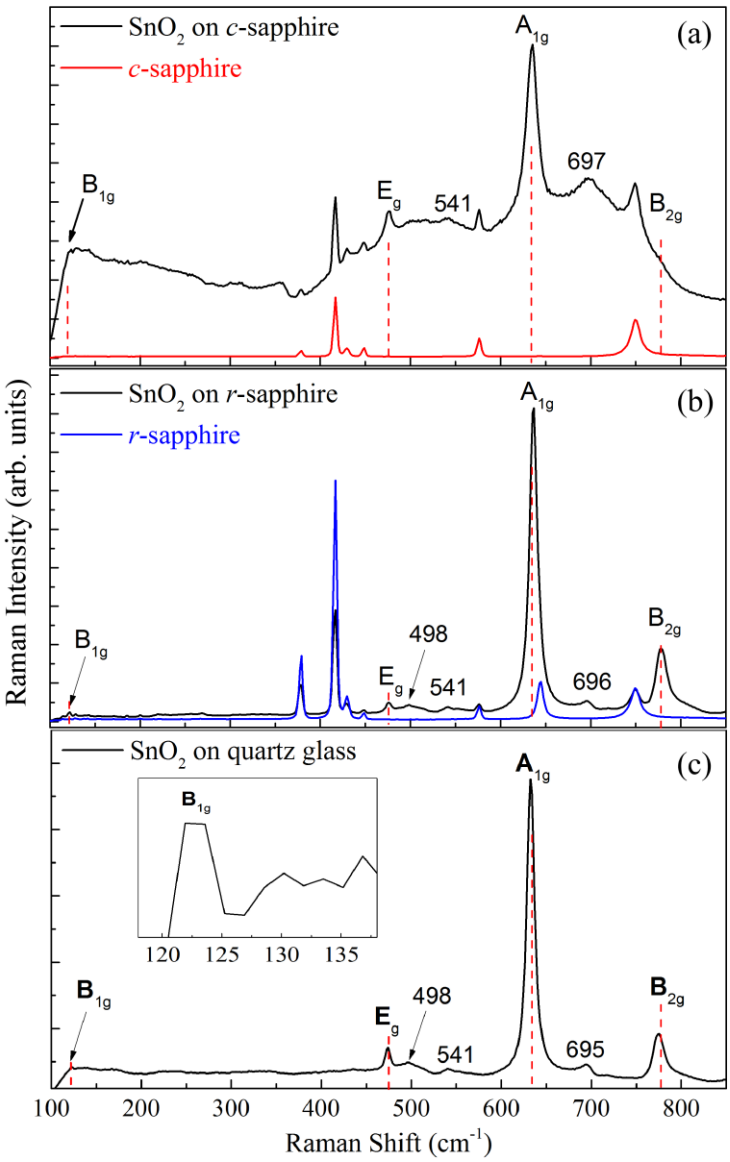

Fig. 8.13. Raman spectra of SnO_2 films grown at a high substrate temperature of 900 °C: (a) SnO_2 (100) on *c*-sapphire; (b) SnO_2 (101) on *r*-sapphire; (c) polycrystalline SnO_2 film on quartz glass. The red dashed lines indicate the positions of the Raman-active modes of B_{1g}, E_g, A_{1g}, and B_{2g}.

To study the angle dependence of the phonon modes of SnO_2, the sample was rotated by 360° about the normal of the sample surface (see Fig. 4.3). Introducing a polarization filter in the optical path of the scattered light from the sample, allows one to analyze parallel aligned polarization vectors of the incident laser light and the scattered radiation from the sample. If the polarization filter is combined with a half-wave plate, perpendicularly polarized light is detected. The theoretically expected intensity dependence on sample rotation can be found in section 4.1.3 tables (4.1) and (4.2).

The B_{1g} mode was too weak to extract quantitative information on intensity variation. We do not discuss the experimental results of the B_{1g} mode in this work.

Fig. 8.14 shows the intensities of the Raman-active modes A_{1g} and E_g of SnO_2 (100) on *c*-sapphire for parallel and perpendicularly aligned incident and scattered polarization vectors versus the rotation angle of the SnO_2 film about the normal of the (100)-plane. All accessible Raman modes are independent of the rotation angle. According to the theoretical calculations in table (4.1), the scattered intensities of the Raman-active modes A_{1g} and E_g should explicitly depend on the rotation angle of the sample. As shown by 4-circle HRXRD ϕ-scan in section 8.2, the SnO_2 film on *c*-sapphire consists of domains rotated by the 120°. If the three types of domains rotated by 120° with respect to each other all contribute to the same extent to the scattering process, the calculated intensities of the Raman-active modes A_{1g} and E_g are constant, i.e., the intensities of the Raman modes are independent of the rotation angle of the film. Our experimental results are in accordance with such considerations.

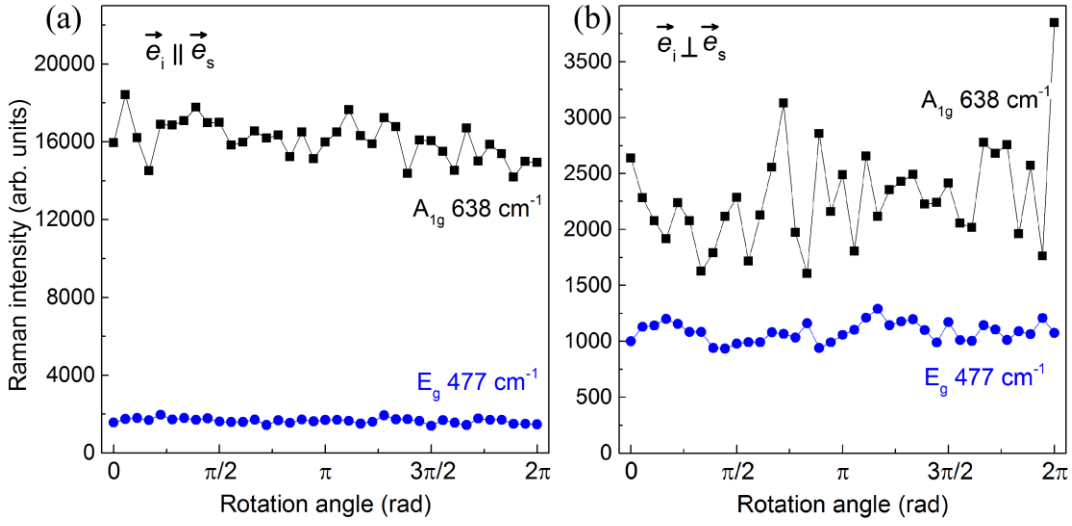

Fig. 8.14. Intensity of the Raman signals of the SnO_2 (100) on *c*-sapphire versus sample rotation about the normal of the (100)-plane for (a) parallel and (b) perpendicularly aligned incident and scattered polarization vectors.

The intensities of the lattice vibrations of A_{1g}, B_{2g}, and E_g symmetry character of SnO_2 (101) on rotation about the normal axis are depicted in Fig. 8.15. The scattered intensities depend explicitly on the rotation angle of the sample. Each phonon reveals a specific dependence on rotation. The E_g mode for both parallel and perpendicularly polarized light is weak.

All the results of the modes A_{1g}, B_{2g}, and E_g for the parallel oriented incident and scattered polarization vectors can be fitted with the equations given in table (4.2) (see solid lines in Fig. 8.15a). However, it is not possible to determine the ratio of the Raman tensor elements *a* and *b* of the A_{1g} mode unambiguously since the fitting procedure is overdetermined. Further it must be noted that the E_g mode does not vanish completely

upon rotation as expected by theory. This result might indicate that the laser spot is not rotated about a single sample location in experiment.

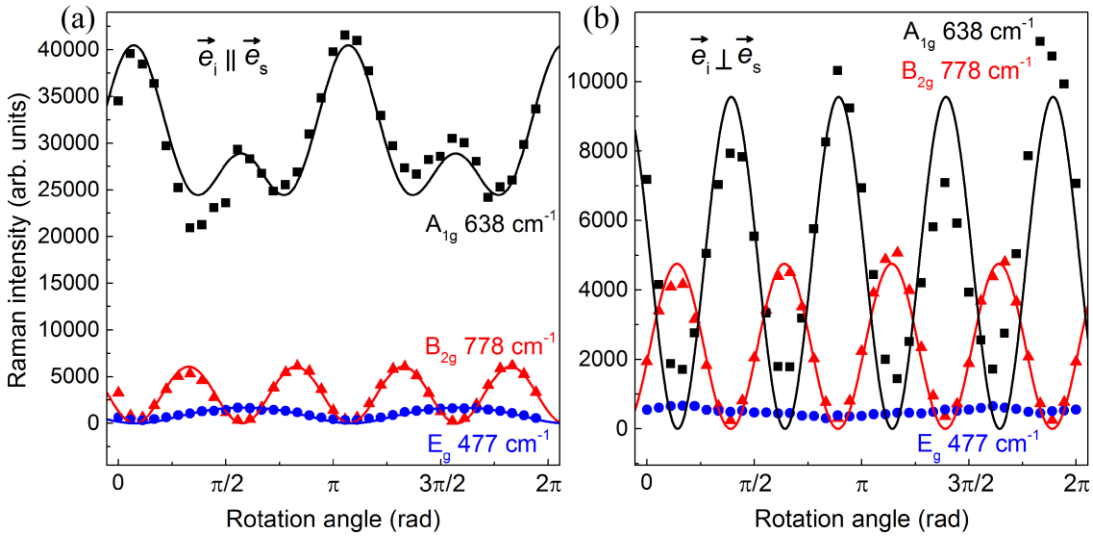

Fig. 8.15. Intensity of the Raman signals of the SnO_2 (101) on *r*-sapphire versus sample rotation about the normal of the (101)-plane for (a) parallel and (b) perpendicularly aligned incident and scattered polarization vectors. The solid lines are fits to the angle dependences based on the functions in section 4.1, table (4.2).

Fig. 8.15(b) depicts the intensities of modes A_{1g}, B_{2g}, and E_g for the perpendicularly aligned incident and scattered polarization vectors versus the rotation angle. The intensity dependence of phonon of B_{2g} symmetry character is well represented by the model function given in table (4.2). The E_g mode cannot be fitted since its signal intensity is too low. At first sight, the function describing the A_{1g} mode reflects the experimental findings. However, the A_{1g} mode does not vanish completely upon rotation in contrast to the theoretical prediction leading to large errors of the fitted parameters *a* and *b*. The reason for that unexpected offset is not clear yet.

8.5 Photoluminescence spectra

In this work, time resolved PL (TRPL) and continuous wave PL (CWPL) measurements at low temperature of 67 K were carried out on the SnO_2 films. Fig. 8.16-18(a) show the PL spectra of the SnO_2 films on *c*-, *r*-sapphire and quartz glass for different excitation powers, respectively. All spectra are dominated by a broad deep-level emission band centered at near 2.6 eV in the visible region. This emission is much lower than the expected band gap of 3.6 eV for the SnO_2 films. Hence, the visible emission cannot be assigned to the direct recombination of a conduction-band electron (associated with the Sn 5*s* states) and a hole valence band (associated with the O 2*p* states [8]). It is rather related to the crystalline defects induced during the growth according to He *et al.*: the interaction of oxygen vacancies with interfacial tin vacancies leads to the formation of a considerable amount of trapped states with energies within the bandgap. These result in the observed dominant PL signal [9]. The spectral break-up in the broad peaks is caused by inhomogeneities in the streak camera′s photoemission rather than from the emission itself, as becomes clear when looking at the time-integrated detection. In addition to the broad deep-level emission, no other peak is observed in the PL spectra of these measured points.

Next, the dependence on excitation intensity is discussed. Fig. 8.16-18(b) show the TRPL data for different excitation powers. The time-resolved signals were integrated across a range of from 1.67 to 3.47 eV wide spectral region centered at the peak PL energy (2.6 eV). The decay times of the films on sapphires are very long, i.e., the decay constant is very slow, in the range of many tens of nanoseconds or longer. The time-zero is hardly observable at the lowest excitation fluency shown, yet becomes more obvious as the system is excited more strongly. These additional carriers give rise to a fast initial decay component which only becomes visible once the deeper trap-states are getting saturated. This the prototypical behavior expected for trapped excitations which radiate dominantly and cannot reach non-radiative recombination centers easily. The decay constant for the SnO_2 films on quartz glass shown in Fig. 8.18(b) is also relatively slow, but it is faster than for the films on sapphire. A probable reason is the polycrystalline nature of the films. In contrast to the material deposited on sapphire, the film on quartz glass substrate consists of many faceted grains. Despite the relatively large grain sizes, it is likely that the grain boundaries provide additional non-radiative recombination channels causing a faster decay of the deep-trap emission.

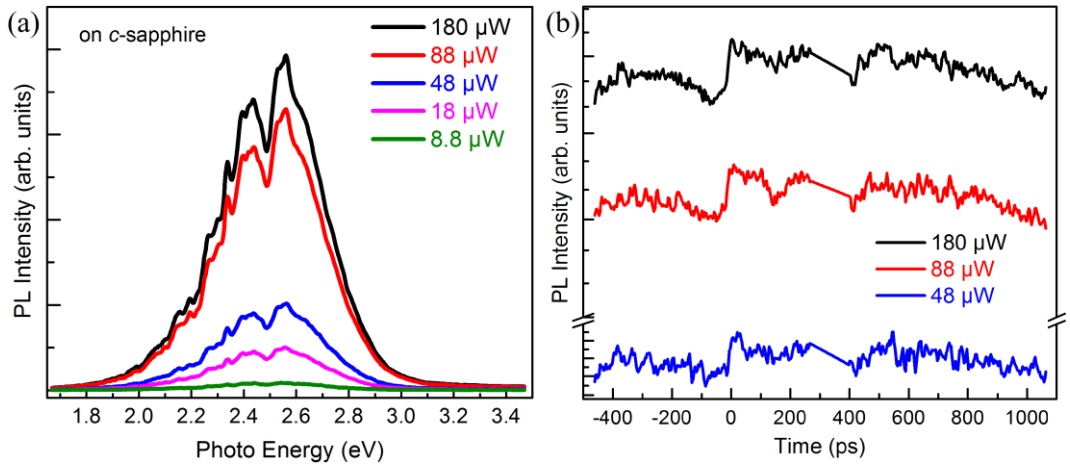

Fig. 8.16. PL spectra (a) and TRPL transients (b) for the SnO_2 film grown on *c*-sapphire with different excitation powers at T = 67K, respectively.

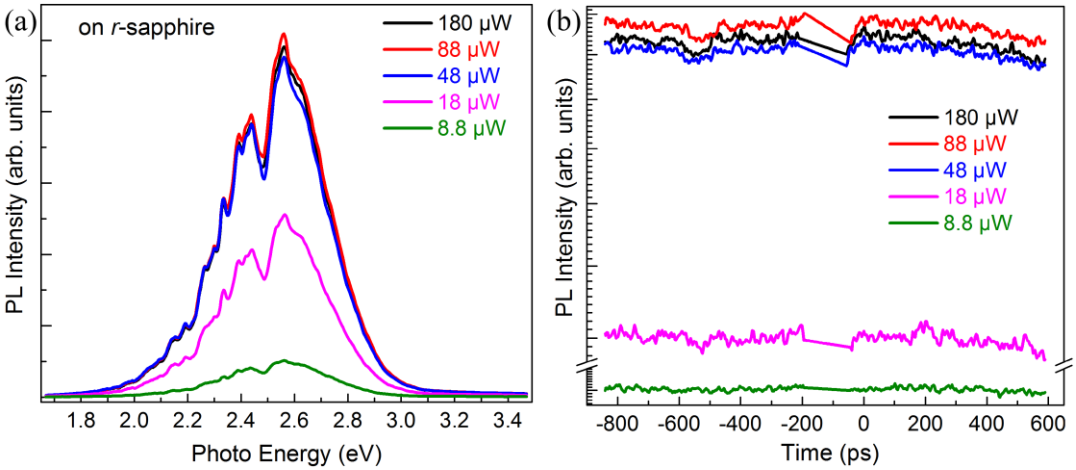

Fig. 8.17. PL spectra (a) and TRPL transients (b) for the SnO_2 film grown on *r*-sapphire with different excitation powers at T = 67K, respectively.

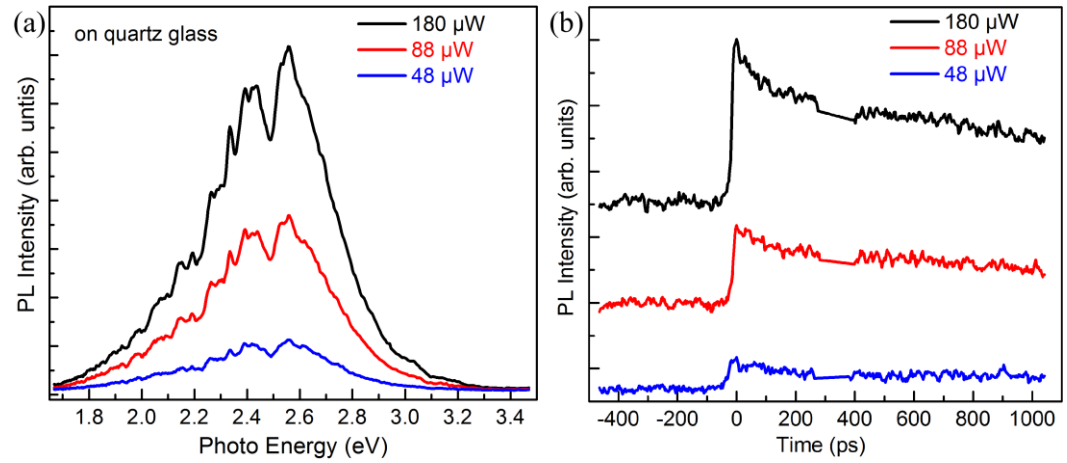

Fig. 8.18. PL spectra (a) and TRPL transients (b) for the SnO_2 film grown on quartz glass with different excitation powers at T = 67K, respectively.

The PL of the SnO_2 film on sapphire substrates was measured at various different positions on the sample. Fig. 8.19(a) shows the PL spectra measured at two different points of the SnO_2 film on *c*-sapphire. The broad deep-level emission is dominant at position 3 (red line) while an additional, sharp UV emission is observed at position 2 (black line). This relatively narrow-band (FWHM of 91 meV) line centered at 3.30eV completely dominates the spectrum, suppressing the deep-level contributions (the integrated time-interval for both was from -500 to 900 ps). A tentative attribution to impurities or defects in the substrates should be ruled out as this pronounced peak was not found there, neither on the back side of the sample (substrate) nor on a second piece of pure *c*-sapphire from the same batch. This emission should hence be related to the SnO_2 film and may tentatively be assigned to emission from bound excitons: a similar feature has been observed by Liu *et al.*, who reported a narrow peak at 3.2 eV for SnO_2 nanowires using PL. [10].

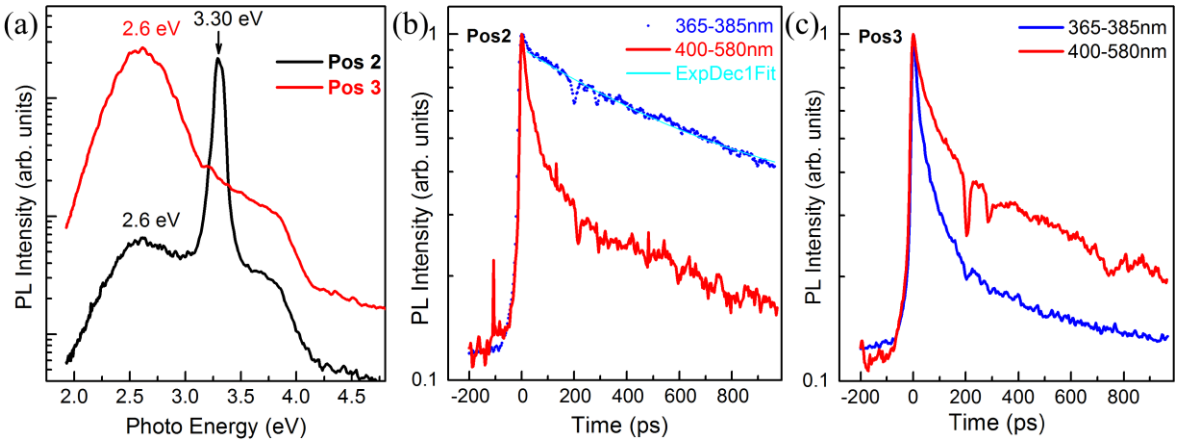

Fig. 8.19. (a) PL spectra acquired at the different positions of the SnO_2 film on *c*-sapphire. The normalized TRPL transients for the position 2 (b) and position 3 (c) of the film integrated over spectral regions of 365-385 nm (blue) and of 400-580 nm (red), respectively.

Fig. 8.19(b-c) show the TRPLs for the two different positions of the film on *c*-sapphire integrated across the spectral regions of 365-385 nm and 400-580 nm in blue and red color, respectively. The TRPL for the position 2 reveals completely different decay dynamics compared with all other data. It is of nearly perfect single-exponential nature, strongly suggesting that this emission channel is excitonic. A numerical fit yields a single-exponential decay constant of about 620 ps.

The dynamics of the radiative recombination are further analyzed by looking at the TRPL spectra for the SnO_2 film on *c*-sapphire at position 2. Fig. 8.20 shows TRPL spectra monitored at various times after the pulsed excitation. Each spectrum is integrated across a time-interval of 30 ps. Panel (a) reveals the intensity variation of the PL spectra. The

impurity emission at about 2.6 eV is observed during all times as it decays most slowly. The narrow-band peak shows more intricate dynamics. Hence, the normalized intensities are plotted in the Fig. 8.20(b), the curves are vertically offset for clarity. Around the excitation at 0 ps (integrated time-interval from -15 to 15 ps), the spectrum is dominated by the emission band at 3.329 eV. This peak shifts gradually towards lower photon energy with increasing time delay. If the time is increased about 6900 ps, the emission band is located at about 3.278 eV. The energy difference of the peak after pulsed excitation between 0 and 6900 ps is about 51 meV. The finding is also observed in $In_{0.20}Ga_{0.80}N$ /$In_{0.05}Ga_{0.95}N$ multiple quantum wells [11]. Narukawa *et al*. suggested that the density of states of localized centers is distributed to some extent, and that localized excitons are transferred further to the lower-lying energy levels.

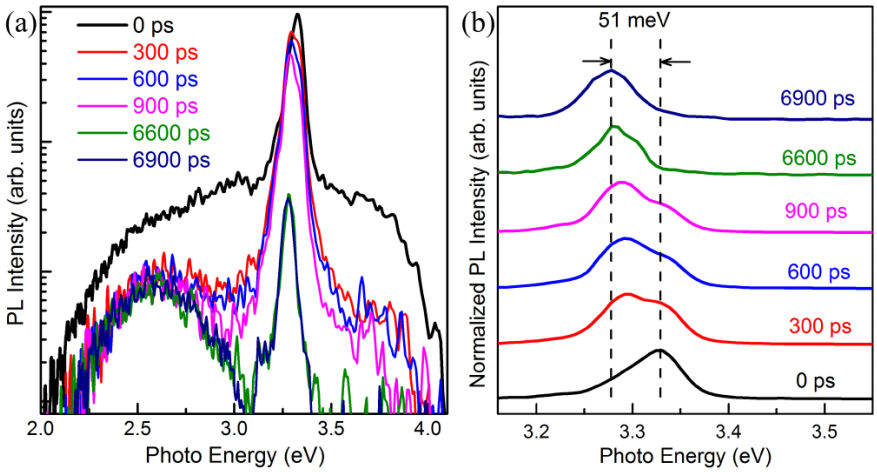

Fig. 8.20. (a) Time-integrated PL spectra monitored at various time integrated during the same time-interval (30 ps) after pulsed excitation. (b) Each spectrum is normalized in intensity.

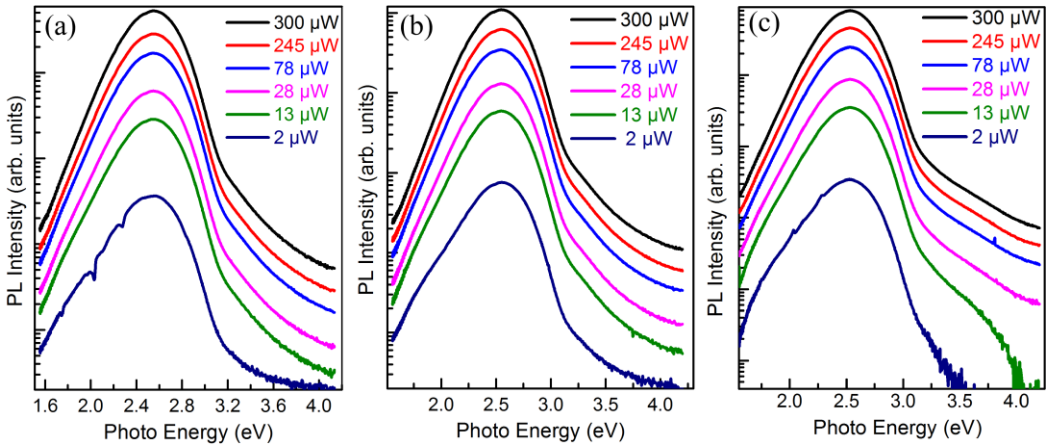

Fig. 8.21. CWPL spectra of the SnO_2 films grown on *c*- (a), *r*-sapphire (b), and quartz glass (c) with different excitation power at temperature of 67 K.

The CWPL spectra of the SnO_2 films grown on *c*- (panel a), *r*-sapphire (panel b) and quartz glass (panel c) with pronounced disorder are shown in Fig. 8.21 at the different excitation powers, respectively. For these experimental conditions, an asymmetric spectral shape of the PL is a clear hallmark of a disordered system (see Ref. [12], page 58). Here, the low energy slope basically represents the distribution of the band-tail states, whereas the much steeper high-energy side of the spectra is related to the carrier temperature and the homogeneous broadening of the optical transition. The peaks for three films on different substrates are located at almost the same energy of 2.6 eV, and do not vary in emission energy with increasing excitation power.

8.6 Optical transmittance

The SnO_2 films grown at high temperature on sapphire are colorless and transparent, while the film on quartz glass with the thickness of 8 µm has a whitish milky appearance. It is attributed to the polycrystalline nature of the film and the related light scattering at the surface. Fig. 8.22 shows the optical transmittance of the samples as a function of the incident light wavelength in the range of 200-2650 nm. The olive green, red, and emerald green curves correspond to the transmittance of the double-face polished pure 0.33 mm thick *r*-, *c*-sapphire, and 0.5 mm thick quartz glass substrates, respectively.

The black curve corresponds to the transmittance of SnO_2 sample on *r*-sapphire. The perfect interference oscillations of the transmittance spectrum in the range from the visible to the infrared demonstrate the flat surface and homogeneity of this film. According to the oscillations of the transmittance spectrum the film thickness is estimated to 4.75 µm and the standard deviation of this film thickness is only 25 nm. The results are in very good agreement with the thickness obtained by SEM (see Fig. 8.7). The average transmittance in the range of Vis-IR is about 80% for the sample and about 85% for the substrate. The absolute average transmittance (i.e. corrected for the substrate contribution) for the deposited SnO_2 film is about 94%.

The blue curve shows the transmittance of the SnO_2 sample on *c*-sapphire. Only weak interference oscillations are visible in this spectrum. According to the oscillations we can calculate the film on *c*-sapphire to be 3.5 µm thick, and the standard deviation of the film thickness is 170 nm, much larger than that of the film on *r*-sapphire. The absolute average transmittance for the SnO_2 film on *c*-sapphire in the range of IR is also more than 90%, but in the visible range it is slightly lower. The rather high transmittance of both thick films is attributed to the good ordering and few impurity defects inside the films. The slightly higher transmittance of the sample on *r*-sapphire is probably due to the better surface quality (see section 8.3)

The rust red curve shows the transmittance of the SnO_2 film on quartz glass. The transmittance of this sample is obviously very low, in stark contrast to that of the films on sapphire. The reason is that the film on quartz glass consists of large polycrystalline grains yielding a very rough faceted surface. The grain boundaries and the rough surface of the film give rise to very strong diffuse scattering leading to the very low transmittance. As the diffuse scattering dominates the transmission of SnO_2 film on quartz glass rather than the absorption, a similar analysis to extract the optical band gap cannot be applied.

The $\alpha^{2/3}$ of the film on *c*- and *r*-sapphire is plotted in Fig. 8.23 as a function of the incident light photon energy $h\nu$. Extrapolating along the linear portion of the $\alpha^{2/3}$ vs. $h\nu$ curve to zero absorption yields a value for the absorption edge of the two SnO_2 film on *c*-

and *r*-plane sapphire of 3.74 eV. This value is close to the band gap 3.6 eV of bulk SnO_2 (see Ref. [13] page 29).

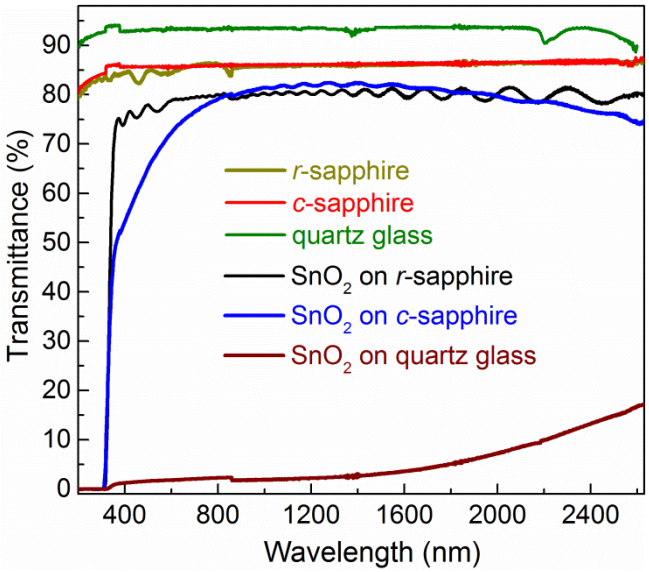

Fig. 8.22. Transmittance spectra for the pure substrates and SnO_2 samples on different substrates. The SnO_2 films on *r*-sapphire with a thickness of 4.7 µm on *c*-sapphire with a thickness of 3.5 µm are transparent; the SnO_2 film on quartz glass with a thickness of ~8 µm is a whitish milky appearance.

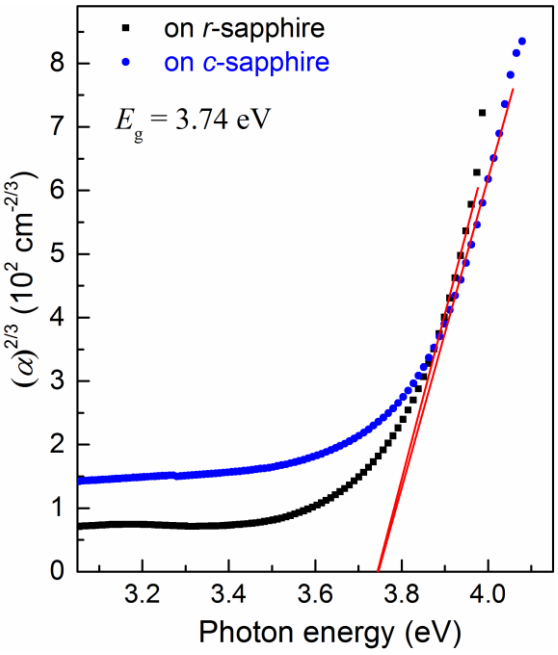

Fig. 8.23. plots of $\alpha^{2/3}$ as a function of photon energy ($h\nu$) for SnO_2 films on *c*- and *r*-sapphire deposited at a substrate temperature of 900 °C.

8.7 Conclusions

The capability of CVD as a suitable technique for growing high quality epitaxial SnO_2 films on *c*- and *r*-sapphire substrates was demonstrated in this chapter. The XRD results reveal that the ω-scan FWHM of (100) reflection and the coherent length along [100] direction of the SnO_2 film on *c*-sapphire are 0.039° and 318 nm, respectively, indicating the very perfect out-of-plane ordering of the SnO_2 film grown at a temperature of 900 °C on *c*-sapphire with a thickness of about 4 µm. However, HRXRD and angle dependent Raman spectra reveal that the in-plane ordering of the films grown on *r*-sapphire is better than that of the film grown on *c*-sapphire. The SEM and AFM results show that these films on sapphire consist of domains with sizes in the range of 20 - 40 µm, and the corresponding film on quartz glass is polycrystalline and consists of single crystallites with sizes between 2 and 7 µm in length. Furthermore, the cross-sectional SEM images reveal that an interface layer with a columnar structure and an extension of about 500 to 800 nm is present in case of *c*-sapphire substrates, which is absent in case of *r*-sapphire substrates. The top of films on sapphire exhibits a terraced structure, and the height of the terrace is in the nanometer range on *c*- and *r*-sapphire. The low temperature (67 K) PL and TRPL spectra exhibit an excitonic emission located at about 3.3 eV, whose energy slightly varies with the time after pulsed excitation. The absolute average transmittance of the films on sapphire substrates is above 90% in the visible and infrared range, which also demonstrates that the epitaxial SnO_2 films grown on sapphire possess very good quality.

References

[1] G.-H. Rue, D.H. Yoo, Y.H. Hwang, H.-K. Kimb, *Synchrotron x-ray scattering study of SnO_2 thin film grown on sapphire*, J. Mater. Res., 17 (2002), 2417-2422.

[2] P.S. Peercy, B. Morosin, *Pressure and Temperature Dependences of the Raman-Active Phonons in SnO_2*, Physical Review B, 7 (1973), 2779-2786.

[3] R.S. Katiyar, P. Dawson, M.M. Hargreave, G.R. Wilkinson, *Dynamics of the rutile structure III. Lattice dynamics, infrared and Raman spectra of SnO_2*, Journal of Physics C: Solid State Physics, 4 (1971), 2421.

[4] X.S. Peng, L.D. Zhang, G.W. Meng, Y.T. Tian, Y. Lin, B.Y. Geng, S.H. Sun, *Micro-Raman and infrared properties of SnO_2 nanobelts synthesized from Sn and SiO_2 powders* J. Appl. Phys., 93 (2003), 1760-1763.

[5] L. Abello, B. Bochu, A. Gaskov, S. Koudryavtseva, G. Lucazeau, M. Roumyantseva, *Structural Characterization of Nanocrystalline SnO_2 by X-Ray and Raman Spectroscopy*, Journal of Solid State Chemistry, 135 (1998), 78-85.

[6] A. Diéguez, A. Romano-Rodríguez, A. Vilà, J.R. Morante, *The complete Raman spectrum of nanometric SnO_2 particles*, J. Appl. Phys., 90 (2001), 1550-1557.
[7] T. Lan, C.W. Li, B. Fultz, *Phonon anharmonicity of rutile SnO_2 studied by Raman spectrometry and first principles calculations of the kinematics of phonon-phonon interactions*, Physical Review B, 86 (2012), 134302.
[8] F. Gu, S. Fen Wang, C. Feng Song, M. Kai Lü, Y. Xin Qi, G. Jun Zhou, D. Xu, D. Rong Yuan, *Synthesis and luminescence properties of SnO_2 nanoparticles*, Chem. Phys. Lett., 372 (2003), 451-454.
[9] J.H. He, T.H. Wu, C.L. Hsin, K.M. Li, L.J. Chen, Y.L. Chueh, L.J. Chou, Z.L. Wang, *Beaklike SnO_2 Nanorods with Strong Photoluminescent and Field-Emission Properties*, Small, 2 (2006), 116-120.
[10] R. Liu, Y. Chen, F. Wang, L. Cao, A. Pan, G. Yang, T. Wang, B. Zou, *Stimulated emission from trapped excitons in SnO_2 nanowires*, Physica E: Low-dimensional Systems and Nanostructures, 39 (2007), 223-229.
[11] Y. Narukawa, Y. Kawakami, S. Fujita, S. Fujita, S. Nakamura, *Recombination dynamics of localized excitons in $In_{0.20}Ga_{0.80}N$-$In_{0.05}Ga_{0.95}N$ multiple quantum wells*, Physical Review B, 55 (1997), R1938-R1941.
[12] A.A. Chernikov, *Time-Resolved Photoluminescence Spectroscopy of Semiconductors for Optical Applications beyond the Visible Spectral Range*, PhD thesis, the faculty of physics, Philipps-Universität, Marburg, (2011).
[13] H. Hosono, D.C. Paine, *Handbook of Transparent Conductors*, Springer, New York Heidelberg Dordrecht London, (2010).

9 Summary and outlook

This thesis work demonstrates that CVD has an excellent potential as a growth technique for high-quality SnO_2 epitaxial thin films. The analysis of the films provides extensive insight into the fundamental physical properties of this material system.

We have attempted to use SnI_2 (Sn^{2+}) (and even tried to use tin metal) as Sn precursor, aiming at achieving SnO as well as SnO_2 films by CVD. However, we have never observed growth of SnO, or the formation of Sn_2O_3, Sn_3O_4, or iodine inclusions in our SnO_2 films in our growth process as confirmed by XRD, XPS and Raman measurements. All films consisted of pure-phase SnO_2 with a rutile structure. In contrast, Becker *et al.* reported that single-phase films of α-SnO were deposited at relative low oxygen flow rate and low substrate temperature by ion beam sputtering [1]. In our case, reducing the oxygen flow rate and the substrate temperature can only reduce the growth rate in the SnO_2 film growth down to no film formation.

In this work we have tried to use quartz glass, *c*-, *r*-, and *a*-plane sapphire as substrates. To optimize the deposition process, we first investigated systematically the influence of the CVD parameters on the film properties, such as the substrate temperature, the precursor SnI_2 evaporation, and the oxygen flow rate, etc. When the substrate temperature was lower than 350 °C, no thin film formation could be achieved on any of the substrates used in the CVD process. The growth rate increased almost linearly with increasing substrate temperature above 350 °C up to 700 °C. However, if the substrate temperature was 900 °C, and the evaporation rate of the SnI_2 was 0.7 g/h, the growth rate of the SnO_2 films rapidly increased to about 2 µm/h and 4 µm/h on sapphire and quartz glass, respectively. Furthermore, the growth rate of SnO_2 films increased also almost linearly with increasing O_2 flow rate at a fixed substrate temperature.

On single crystal substrates we always obtained highly oriented epitaxial SnO_2 films, whereas polycrystalline SnO_2 thin films always were formed on quartz glass. The films were preferentially formed with SnO_2 (110) parallel to the quartz glass substrate surface for film thicknesses up to about 400 to 500 nm. This observation is expected as the (110)-plane possesses the lowest surface formation energy in SnO_2 [2]. However, the dominant reflections in the XRD spectra changed significantly for films thicker than 1 µm. The SnO_2 (211) reflection instead of (110) reflection becomes the preferred orientation of the SnO_2 films on quartz glass.

A series of epitaxial SnO_2 films were obtained on *c*-plane sapphire. The films on *c*-sapphire show an epitaxial relationship with the substrate of SnO_2 (100)$\|Al_2O_3$ (001) (out-of-plane) and SnO_2[010]$\|Al_2O_3$<110> (in-plane). Detailed analysis using XRD and SEM

reveal that the crystal quality and the morphology of SnO_2 films are dependent on the O_2 flow rate during film deposition, which is very likely caused by a variation of the V_O density in the films. This series of experiments indicates that the quality of SnO_2 films is enhanced with increasing O_2 gas flow rate up to 40 sccm, and then declines with further increase of the O_2 flow rate. As the O_2 flow rate is increased, the carrier concentration in films decreases from 3×10^{19} to 9×10^{17} cm^{-3}. This indicates a decrease of the V_O concentration with increasing O_2 flow rate during the film growth.

The epitaxial SnO_2 film on *c*-sapphire starts in the Volmer-Weber growth mode. The films initially grow by the nucleation of discrete islands with rectangular unit cells of c = 3.187 (relaxed) and b = 4.759 Å (strained) in-plane. There are three possible orientations of the unit cell of the SnO_2 islands with respect to the *c*-sapphire substrate. The orientations are rotated by 120° with respect to each other. At a characteristic layer thickness of about 50 nm the islands begin to merge, leading to a closed SnO_2 film growth on *c*-sapphire with a characteristic domain structure. This growth mechanism of SnO_2 films on *c*-sapphire by CVD is independent of the substrate temperature in the range of 450 - 650 °C.

The films grown on *r*-plane sapphire substrates also consist of pure-phase SnO_2. The epitaxial relationship of the films with the substrate is $SnO_2(101) \| Al_2O_3(01\bar{1}2)$ out-of-plane, $SnO_2[010] \| Al_2O_3[100]$ and $SnO_2[10\bar{1}] \| Al_2O_3[\bar{1}\bar{2}1]$ in-plane. But the orientation of SnO_2 (101) has a small tilt angle (about 1° to 2°) with the orientation of $Al_2O_3(01\bar{1}2)$ for substrate temperatures between 450 and 650°C. The tilt orientates crystallites towards two opposite directions with mirror symmetry. How to control the distribution the formation of fractions of grains of either symmetry and the relation between dislocation and crystallographic tilt, and how the mirror symmetry influences the optical and electrical properties of the films is not clear.

The films with thickness smaller than 1 µm are colorless and transparent. The absolute average transmittance of the films is more than 85% in the visible and infrared range. The optical absorption edge is in the range of 3.57 to 3.78 eV in this study.

High-quality heteroepitaxial SnO_2 films can be obtained at a high substrate temperature of 900 °C by CVD. The growth rate of these films on sapphire is about 2 µm/h. XRD measurements determined the FWHM of rocking curve of SnO_2 (200) reflection for the film with thickness of 3.5 µm on *c*-sapphire to be only 0.04°, indicating the high degree of out-of-plane ordering of this film. The three lattice parameters of the film on *r*-sapphire are calculated to be 4.738 Å, 4.738 Å and 3.184 Å, indicating that thick films are just like bulk SnO_2. The SEM measurements show that no grains or grain boundaries are observed on the films surface. The domains of these films are huge and possess diameters of more than 30 µm. Angle-dependent Raman spectra for SnO_2 (101) on *r*-sapphire is in good agreement with the calculated scattering intensities of the phonon modes A_{1g}, B_{2g} and E_g. The low temperature (67 K) PL and TRPL spectra exhibit an excitonic emission located at about

3.3 eV, whose energy slightly varies with the time after pulsed excitation. A broad deep-level emission is located at 2.6 eV, which is probably caused by the formation of trapped states due to oxygen vacancies. The absolute average transmittance of the films on sapphires is above 90% in the visible and infrared range. An optical absorption edge of 3.74 eV for these thick films on sapphire substrates is estimated.

The success of epitaxial growth of SnO_2 films on *c*- and *r*-sapphires indicates that heteroepitaxy may not only occur in material systems with similar structural symmetry, e.g. cubic on cubic, tetragonal on cubic, or vice versa, but is also possible for materials with different symmetry, e.g., tetragonal on hexagonal. Epitaxial growth of SnO_2 on sapphire has been demonstrated by various deposition techniques, such as CVD, MBE, sputter deposition and PLD etc. The best results have been obtained on *r*-sapphire substrates. This is in agreement with the findings of this thesis for CVD growth. Thus, the foundation is laid for obtaining high quality SnO_2 films which can be used in fundamental studies of the properties of this material system. Research directions based on the findings reported here may concern the open questions of controlled extrinsic doping of SnO_2 or of improvement of the SnO_2 films by employing sputtered SnO_2 buffer layers. Both are issues, which need to be addressed on the road towards SnO_2 devices.

References

[1] M. Becker, A. Polity, P.J. Klar, B.K. Meyer, *Synthesis of tin oxides SnO_{2-x} in the entire composition range (x = 0 to 1) by ion-beam sputter-deposition*, physica status solidi (RRL) – Rapid Research Letters, 9 (2015) 326-330.

[2] M. Batzill, U. Diebold, *The surface and materials science of tin oxide*, Progress in Surface Science, 79 (2005) 47-154.

Danksagung

An dieser Stelle möchte ich mich bei all jenen herzlich bedanken, die mich direkt und indirekt während der Anfertigung dieser Dissertation unterstützt haben und mir hilfreich zur Seite standen.

Als erstes danke ich **Prof. Dr. Bruno K. Meyer**. Seit er 1999 meinen Ehemann **Yunbin He** ins I. Physikalische Institut als einen Doktorand aufgenommen hat, hat er unserer Familie sehr viel geholfen. 2005-2006 hat er mich am Institut als seine Diplomandin aufgenommen. 2015 hat er mir wieder die Möglichkeit gegeben, meine Doktorarbeit in seiner Gruppe anfertigen zu können. Er begeisterte mich in Zeiten experimenteller Schwierigkeiten und half mir mit vielen Diskussionen und Erläuterungen. Er schaffte eine sehr angenehme Arbeitsatmosphäre im Institut. Als eine Ausländerin fühle ich mich sehr wohl im Gießen. Er war mein und auch Yunbin's Doktorvater. Leider haben wir mit seinem Tod am 02. 12. 2014 den liebgewonnenen Betreuer verloren. Ich möchte ihm diese Arbeit widmen.

Mein besonderer Dank gilt auch **Prof. Peter J. Klar** für die Übernahme der Betreuung meiner Arbeit. Er ermöglichte mir, weiter am Institut meine Doktorarbeit zu schreiben, bot mir einen Einblick in der Raman Technik und unterstützte mich bei der Erstellung dieser Arbeit, korrigierte immer sehr schnell meine Manuskripte, und diskutierte intensiv diese Arbeit mit mir.

Dr. Limei Chen danke ich herzlichen für die Raman-Messungen und familiäre Freundschaft. Sie war immer die erste Korrekturleserin meines Manuskripts, joggte mit mir, lud mich ein mit anderen gemeinsam bei ihr zu essen, usw. Ohne ihre Begleitung wäre meine Zeit in Gießen nicht so bunt gewesen.

Prof. Dr. Detlev M. Hofmann danke ich für das anhaltende Interesse an meinen Ergebnissen und die geduldige Auseinandersetzung mit vielen kleineren und größeren Fragestellungen.

PD Dr. Angelika Polity danke ich für das Korrekturlesen von allen Postern für die DPG und für internationale Tagungen, von Manuskripten und dieser Arbeit.

Prof. Dr. Martin Eickhoff danke ich für Korrektur des Manuskripts und die freundliche Übernahme des Zweitgutachtens.

PD Dr. Sangam Chatterjee an Philipps-Universität Marburg danke ich für die PL-Messungen und die geduldige Beantwortung meiner vielen Fragen.

Dr. Jürgen Bläsing an Otto-von-Guericke Universität Magdeburg danke ich für die große Anzahl an hochaufgelösten Röntgendiffraktometriemessungen, die freundlichen Antworten auf meine Fragen zu XRD, und die Korrektur eines Manuskripts.

Mein besonderer Dank gilt auch **Dipl.-Phys. Gunther Haas**, der mich in das Labor eingeführt hat. Während eines Jahres gemeinsamer Arbeit im Epitaxielabor hat er mir geholfen, die Mini-CVD-Reaktor zu reformieren. Er hat mir die verschiedenen Charakterisierungsmethoden gezeigt und erklärt, und stand mir mit Rat und Tat zur Seite. Leider hatte er einen tödlichen Unfall am 01. 05. 2013.

Dr. Jie Jiang danke ich für die vielen Diskussionen und die freundliche Laboratmosphäre.

Den Sekretärinnen **Anja Denhardt** und **Helge E. Höchsmann** danke ich für ihre Hilfsbereitschaft in administrativen Angelegenheiten, Zusendung von Proben usw.

Nicht zu vergessen gilt großer Dank **Hans Peter Jorde** für die Unterstützung bei Computer-Angelegenheiten und Software.

Ich bedanke mich bei den Mitarbeitern in sowohl der feinmechanischen als auch der Elektronikwerkstatt für die schnelle wertvolle Hilfe.

Allen Mitarbeitern und Mitarbeiterinnen des I. Physikalischen Instituts danke ich sehr für die angenehme Arbeitsatmosphäre und die ständige Hilfsbereitsschaft. Besonderen Dank auch an **Marc K. Dietrich** für viele Diskussionen über optische Messungen und die Begleitung an meinem ersten Tag an der Uni und in Gießen, **Martin Becker** für viele Diskussionen über SnO_2 Material und AFM-Messungen, **Benedikt Kramm** für die XPS-Messungen, **Melanie Pinnisch** für die PL-Messungen, die glückliche Zeit in einem Büro sowie ihre freundliche Hilfe bei meinem Umzug, **Thomas Sander** für die Anleitung zur Durchführung von Raman-Messung, die Hilfe bei der Berechnung der winkel-abhängigen Raman-Intensitäten und die Raman-Messungen, **Dr. Matthias Elm** für die Begleitung meiner ersten FESEM Benutzung, **Julian Benz** für die Strukturierung der Proben mittels Ionenstrahlätzens, **Max Kracht** für die 4-Kreis XRD-Messungen, **Philipp Hering** für die Anleitung zur Durchführung von Hall-Effekt-Messungen, **Frieder Müntze** am Institut für Angewandte Physik für die schnellen AFM-Messungen, und **Johannes Bieber**, **Florian Heck** für die gemeinsame freundliche Zeit im Epitaxielabor.

Für ein tolles Arbeitsklima und große Hilfsbereitschaft möchte ich mich beim gesamten I. Physikalischen Institut bedanken. Danke für die schöne Zeit in Gießen, und in Deutschland.

Besonders herzlichen Dank gilt meinen Eltern, **Kangfu Lu** und **Qingyun Liu** für die jahrelange Unterstützung während meines Studiums. Als ich ihnen beunruhigt von meinem Vorhaben in Deutschland zu promovieren erzählte, sagte mein Vater sofort: ,,folge deinen Träumen. Keine Sorge. Wir werden uns um **Jiekai** kümmern. ‘‘Mein besonderer Dank gilt natürlich auch dem wichtigsten Menschen in meinem Leben **Yunbin** für den lieben Rückhalt während meines Studiums, für die zweijährige Begleitung in Gießen und vielen wissenschaftlichen Diskussionen und Dispute.

Publications and conference contributions

Publications

1) **Y. M. Lu**, J. Bläsing, L. L. Zheng, Y.B. He, B. K. Meyer, M. Eickhoff and P. J. Klar, Growth mechanism of SnO_2 films on *c*-sapphire by chemical vapor deposition, ***J. Appl. Phys.*** 2015 (under review).

2) **Y. M. Lu**, J. Jiang, C. Xia, B. Kramm, A. Polity, Y. B. He, P. J. Klar and B. K. Meyer, The influence of oxygen flow rate on properties of SnO_2 thin films grown epitaxially on *c*-sapphire by CVD, ***Thin Solid Films***, 594 (2015) 270-276 (IF: 1.759).

3) **Y. M. Lu**, J. Jiang, M. Becker, B. Kramm, L. Chen, A. Polity, Y. B. He, P. J. Klar, and B. K. Meyer, Polycrystalline SnO_2 films grown by chemical vapor deposition on quartz glass, ***Vacuum***, 122 (2015) 347-352. (IF: 1.858)

4) Yunbin He, Hailing Cheng, Jiali Tai, Lei Li, Lei Zhang, Mingkai Li*, **Yinmei Lu**, Wei Zhang, and Bruno K. Meyer, Single-phase quaternary $Mg_xZn_{1-x}O_{1-y}S_y$ alloy thin films grown by pulsed laser deposition, ***J. Appl. Phys***. 117 (2015) 065301. (IF: 2.183)

5) Lei Zhang, Lei Li, Liangheng Wang, Mingkai Li, **Yinmei Lu**, Bruno K. Meyer, Yunbin He, Tuning the composition and optical band gap of pulsed laser deposited $ZnO_{1-x}S_x$ alloy films by controlling the substrate temperature, ***J. Alloy. Compd.***, 617 (2014) 413–417. (IF: 2.999).

6) Yunbin He, Lei Zhang, Liangheng Wang, Mingkai Li, Xunzhong Shang, Xiong Liu, **Yinmei Lu**, and Bruno K. Meyer, Structural and optical properties of single-phase $ZnO_{1-x}S_x$ alloy films epitaxially grown by pulsed laser deposition, ***J. Alloy. Compd.***, 587 (2014) 369–373. (IF: 2.999).

7) Jie Jiang, **Yinmei Lu**, Benedikt Kramm, Fabian Michel, Christian T. Reindl, Max Kracht, Peter J. Klar, Bruno K. Meyer, Martin Eickhoff,

Nitrogen incorporation in SnO_2 thin films grown by chemical vapor deposition, ***Phys. Status Solid B***, 2016 (to submit)

Talks and poster presentations

8) **Yinmei Lu,** Martin Becker, Jürgen Bläsing, Angelika Polity and Bruno K. Meyer, High-quality SnO_2 thin films grown by chemical vapor deposition, 5th International Symposium on Transparent Conductive Materials, Platanias-Chania, Crete, Greece, 17.10.2014, O-1110, p.191, (oral)

9) Jie Jiang, **Yinmei Lu,** David Hartung, Benedikt Kramm, Christian T. Reindl and Bruno K. Meyer, The effect of NH_3 in SnO_2 thin films grown by chemical vapor deposition, 5th International Symposium on Transparent Conductive Materials, Platanias-Chania, Crete, Greece, 14.10.2014, O-1195, p.63, 2014.

10) **Y. M. Lu**, J. Jiang, M. Becker, B. Kramm, M. Pinnisch, J. Bläsing, L. Chen, P. J. Klar, A. Polity and B. K. Meyer, High-quality SnO_2 thin films on c-sapphire by chemical vapor deposition, 13th European Vacuum Conference, Aveiro, Portugal, 08.09.2014, TF126, (Poster)

11) **Y. M. Lu**, L. Chen, M. Becker, J. Jiang, P. J. Klar, A. Polity and B. K. Meyer, High-quality SnO_2 thin films grown by chemical vapor deposition, Frühjahrstagung der Deutschen Physikalischen Gesellschaft, Dresden, Germany, 03.04.2014, HL 107.11, (Poster).

12) Jie Jiang, **Yinmei Lu**, Johannes Bieber, Elizabeth Anna Zolnowski, Bruno K. Meyer, Nitrogen doping in SnO_2 thin films grown by chemical vapor deposition, Frühjahrstagung der Deutschen Physikalischen Gesellschaft, Dresden, Germany, 03.04.2014, HL 107.12.

13) **Yinmei Lu**, Gunther Haas, Xia Chun, Melanie Pinnisch, Martin Becker, Johannes Bieber, B. K. Meyer, Epitaxial growth of SnO_2 films on *c*- and *r*-sapphire by CVD, Frühjahrstagung der Deutschen Physikalischen Gesellschaft, Regensburg, Germany, 03.2013 (Poster).

Selbstständigkeitserklärung

Hiermit versichere ich, die vorgelegte Dissertation selbstständig und ohne unerlaubte fremde Hilfe und nur mit den Hilfen angefertigt, die ich in der Dissertation angegeben habe. Alle Textstellen, die wörtlich oder sinngemäß aus veröffentlichten Schriften entnommen sind, und alle Angaben, die auf mündlichen Auskünften beruhen, sind als solche kenntlich gemacht. Bei den von mir durchgeführten und in der Dissertation erwähnten Untersuchungen habe ich die Grundsätze guter wissenschaftlicher Praxis, wie sie in der ,,Satzung der Justus-Liebig Universität Gießen zur Sicherung guter wissenschaftlicher Praxis‘‘ niedergelegt sind, eingehalten.

Yinmei Lu